2550

LABORATORY STUDY OF THE UV INDUCED POPULATION TRANSFER IN INTERSTELLAR OH

G. W. M. VAN MIERLO

LABORATORY STUDY OF THE UV INDUCED POPULATION TRANSFER IN INTERSTELLAR OH

PROMOTOR : PROF. DR. A. DYMANUS
CO-REFERENT : DR. J. J. TER MEULEN

LABORATORY STUDY OF THE UV INDUCED POPULATION TRANSFER IN INTERSTELLAR OH

PROEFSCHRIFT

TER VERKRIJGING VAN DE GRAAD VAN DOCTOR
IN DE WISKUNDE EN NATUURWETENSCHAPPEN
AAN DE KATHOLIEKE UNIVERSITEIT TE NIJMEGEN,
OP GEZAG VAN DE RECTOR MAGNIFICUS
PROF. DR. P. G. A. B. WIJDEVELD
VOLGENS BESLUIT VAN HET COLLEGE VAN DECANEN
IN HET OPENBAAR TE VERDEDIGEN
OP DONDERDAG 22 JANUARI 1981
DES NAMIDDAGS TE 4 UUR

DOOR

GERARDUS WILHELMUS MARIA VAN MIERLO

geboren te Arnhem

krips repro meppel

Allen die op enigerlei wijze bijgedragen hebben tot de verwezenlijking van dit proefschrift wil ik op deze plaats gaarne dank zeggen. In het bijzonder wil ik vermelden:

De leden van de groep Atoom- en Molecuulfysica van de Katholieke Universiteit te Nijmegen voor hun prettige samenwerking;

De Heren F.A. van Rijn en J.J. Holtkamp voor hun onontbeerlijke hulp bij de vele electronische problemen;

De Heren L. Hendriks en E.G.H. van Leeuwen voor hun niet aflatende steun bij technische moeilijkheden;

Dr. B.Th. Berendts en de Heer J.A.M. Faazen voor hun prettige samenwerking tijdens de natuurkunde praktika en hun welwillende hulp bij het lenen van vele onontbeerlijke componenten;

Dr. W. Hogervorst van de Vrije Universiteit te Amsterdam voor zijn hulp bij het ijken van de interferometer;

De dienstverlenende afdelingen in de personen van de Heren J. van Langen, P. Walraven, H. Verschoor en J. Holten voor hun vakkundige bijstand;

De afdelingen Illustratie en Fotografie o.l.v. de Heren J. Gerritsen en H. Spruyt voor het verzorgen van vele figuren;

De Directie en medewerkers van het Physisch Laboratorium TNO voor hun zeer gewaardeerde steun bij het schrijven en gereed maken van dit proefschrift, in het bijzonder de Heer G.J. Mooy voor het tekenen van enige figuren in de tijdnoodfase en de Heer J.M. Mazer voor de verzorging van de fotografische afdrukken;

Tenslotte wil ik mijn vrouw graag bedanken voor het vele typwerk dat zij verzet heeft en de steun die ik heb mogen ontvangen bij het tot stand brengen van dit proefschrift.

Het onderzoek, dat in dit proefschrift beschreven staat, is een gedeelte van het onderzoekprogramma van de "Stichting voor Fundamenteel Onderzoek der Materie" (FOM), welke financieel gesteund wordt door de "Nederlandse Organisatie voor Zuiver Wetenschappelijk Onderzoek" (ZWO).

voor mijn ouders,

voor Els en Christa

CONTENTS

Page

CHAPTER 1 INTRODUCTION

1.1 Anomalous microwave emissions from interstellar hydroxyl 9
1.2 The experimental method 13

CHAPTER 2 THE UV INDUCED POPULATION TRANSFER MECHANISM AND ITS EXPERIMENTAL INVESTIGATION

2.1 The molecular properties of the hydroxyl radical 18
2.2 UV pumping in interstellar space
 2.2.1 The population transfer mechanism 24
 2.2.2 The transfer equations 27
2.3 The required UV source 34

CHAPTER 3 THE UV SOURCE

3.1 Second harmonic generation
 3.1.1 Theory 40
 3.1.2 Intra-cavity SHG 50
3.2 The frequency doubled dye laser 52
3.3 Frequency stabilization 60
 3.3.1 Cavity mode stabilization 62
 3.3.2 Etalon stabilization 66
3.4 Results and discussion 68

CHAPTER 4 THE OH BEAM MASER AND UV EXCITATION

4.1 Outline of the maser set-up 72
4.2 The UV transportation system and excitation region 74
4.3 The state selection 78
4.4 The microwave detection system 85
4.5 The OH absorption cell 87

CHAPTER 5 THE EXPERIMENTAL RESULTS

5.1 The hyperfine structure of the $A^2\Sigma^+_{1/2}$ state 90
5.2 The UV induced population transfer 97

CHAPTER 6 ASTROPHYSICAL CONSEQUENCES AND CONCLUSIONS

6.1 The population transfer proces in interstellar OH 107

6.2 Conclusions 119

APPENDIX 1 122

APPENDIX 2 124

APPENDIX 3 127

REFERENCES 129

SAMENVATTING 134

Curriculum Vitae 137

CHAPTER 1

INTRODUCTION

1.1 ANOMALOUS MICROWAVE EMISSIONS FROM INTERSTELLAR HYDROXYL

The hydroxyl radical (OH) is one of the most intensively studied molecules. It plays a major role in laboratory chemistry, atmospheric pollution studies and radio astronomy; it is also one of the simplest diatomic molecules readily accessible for a wide range of spectroscopic techniques in the optical (DIE 62, ELM 72), infrared (DUC 72) and microwave (DOU 55, POY 68, MEE 75, MEU 72) regions of the spectrum. In 1963 Weinreb et al (WEI 63) reported the first observation of the absorption spectrum of OH at 18 cm in the radio source Cas A. This spectrum originates from the four hyperfine transitions $F=1,2 \rightarrow F'=1,2$ across the Λ-doublet of the rotational ground state ($X^2\Pi_{3/2}$, $J=3/2$). This discovery was followed two years later by the detection of emission spectra in W49 and NGC6334 by Weaver et al (WEA 65). In the subsequent period of time emission spectra, also from several excited rotational states, were reported in a large number of sources. In all but very few cases, the observations revealed many puzzling features, the most striking being the extremely high brightness temperatures of 10^{10}-10^{15} K observed in some sources. Turner (TUR 70) divided the OH formations into four classes of objects, distinguished by certain characteristic features. Class I OH sources show anomalously strong emissions in the main transition(s) $F=1 \rightarrow 1$ and/or $F=2 \rightarrow 2$ situated, respectively, at 1665 and 1667 MHz with the former being stronger in most sources (W3, W49, NGC6334); the observed linewidths are usually very small, corresponding to kinetic temperatures well below 50 K, and the emitted radiation is strongly linearly or circularly polarized. These sources seem to be associated with shock front boundaries between H_I and H_{II} regions (HAB 74), young formations (O or B type stars) or thermal radio sources. The class II(a) and II(b) sources show emission only at 1720 MHz and 1612 MHz, respectively, corresponding to the usually weak satellite transitions ($\Delta F=\pm 1$) between the upper and lower Λ-doublet levels, whereas Class III sources emit very weakly in all lines with apparently normal intensity ratios (local thermal equilibrium).

The very high brightness temperatures and small linewidths can only be explained if some kind of cosmic maser action is present: stimulated emission of microwave photons at frequency ν_o, triggered either by the spontaneous emission or by the 3 K background radiation, can produce the required intensities, provided the population n_u of the upper level of the considered transition is sufficiently higher than the occupation n_l of the lower level. The intensity change dI_ν at frequency ν with distance (s), stimulated by radiation with intensity I_ν, is then given by:

$$\frac{dI_\nu}{ds} = g(\nu)I_\nu(n_u - n_l) \tag{1-1}$$

with $g(\nu)$ a factor depending on the lineshape and strength of the transition $u \rightarrow l$. If, for simplicity, $n_u - n_l$ is assumed to be independent of s, integration of (1-1) gives the exponential behaviour:

$$I_\nu(s) = I_\nu(0)\exp[g(\nu)(n_u - n_l)s] \tag{1-2}$$

From this expression and the Gaussian (Doppler) frequency dependence of $g(\nu)$ the high brightness temperatures (high intensities) and narrow linewidths of the maser emission (when $n_u > n_l$) are explained, if sufficient length s of the OH formation is available. Since in thermal equilibrium $n_u < n_l$ the situation in which $n_u > n_l$ is called population inversion. If $n_u < n_l$ the microwave radiation is absorbed in the hydroxyl formation. Litvak et al (LIT 66) proposed a mechanism based on the electronic excitation of OH by by selective absorption of UV radiation near 308 nm and capable of producing the required population inversion in Class I OH sources. Rotational and vibrational excitation of OH by IR radiation, followed by decay of the excited state, can under certain conditions also produce the required inverted population in Class I or Class II sources (LIT 69, ELI 76). Also collisions with anisotropically streaming electrons (JOH 67), H, H_2 or He (BER 76) and collisional dissociation of H_2O by H atoms (GWI 73) are suggested to produce anomalous population distributions in OH. Practically no experimental investigations on these mechanisms have been reported. Collisions of OH with electrons has been studied by ter Meulen (MEU 76). He also discovered an inverted Λ-doublet population distribution originating in the production of OH from the reaction $H + NO_2 \rightarrow OH + NO$ (MEU 76a). Since that time several authors have reported "chemical" population inversions between the Λ-doublet states of OH (MAR 77, LEM 79, GER 80).

In this thesis the UV induced population transfer mechanism for Class I OH sources is investigated. This proces is shown schematically in Fig. 1.1. The OH radicals are excited to the first excited electronic state $A^2\Sigma^+_{1/2}$ by UV radiation near 308 nm via six rotational transitions from the $X^2\Pi_{3/2}$, J=3/2 ground state

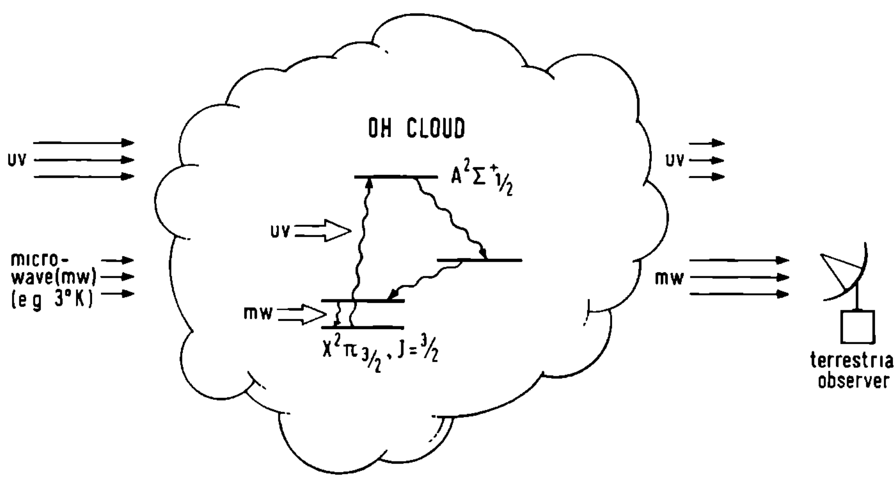

Fig. 1.1 A schematic view of the UV induced inversion of the ground state Λ-doublet populations and the resulting maser proces in the OH cloud.

(if hyperfine structure is included a total of 20 transitions is obtained). In the subsequent decay of the Σ state, the excited population is redistributed over the levels in the $X^2\Pi_{3/2}$, J=3/2 state. Because the line strengths of the various UV transitions are not equal, the net population transfer strongly depends on which transition is dominating the excitation at a particular position inside the hydroxyl cloud. As the UV penetrates into the cloud, the intensities at frequencies corresponding to different transitions are also absorbed differently, because of these unequal line strengths (and therefore unequal absorption coefficients). Consequently excitation via the strongest lines determines the population transfer at small optical depths, whereas the weaker transitions are responsible for the redistribution at larger depths into the cloud. This effect causes the amount of population inversion to vary considerably along the path of the UV radiation. Turner (TUR 70) showed, that (partial) overlap between adjacent hyperfine UV transitions severely influences the population transfer proces due to the interaction of the exciting transitions by absorption of UV radiation at the same frequency. This effect is confirmed in our calculations (Chap. 2 and 6), which also show that collisions between hydroxyl and other particles (mainly molecular hydrogen) strongly interfere with the radiative transfer proces by inducing transitions across the ground state Λ-doublet and opening transfer routes forbidden for radiative processes. This results in a large reduction of the amount of inverted population. To determine the resulting population distribution in the ground state the knowledge of the complete energy structure of both the ground and excited electronic states, including hyperfine structure, is required. This information is available for the $X^2\Pi_{3/2}$ state (DES 77). In the $A^2\Sigma^+_{1/2}$ state the rotational and rho-doubling structure is known from measurements reported by Diecke and Crosswhite (DIE 62) and Engleman (ENG 72). A theoretical prediction of the hyperfine splitting in the first excited rotational state in $A^2\Sigma^+_{1/2}$ is given by German _et al_ (GER 73) based on measurements on OD.

In the present investigation stimulated emission in a Λ-doublet transition of an excited rotational $X^2\Pi_{3/2}$ state is observed, when pumping molecules from the ground state to the $A^2\Sigma^+_{1/2}$ state by UV excitation. The population inversion produced is of the order of 1% (Chap. 5). Moreover, the hyperfine structure in the $A^2\Sigma^+_{1/2}$ state has been determined experimentally for the first time. The hyperfine splittings turned out to be a factor of 10 larger than in the $X^2\Pi_{3/2}$ state and consequently can have a strong influence on the population transfer via the $A^2\Sigma^+_{1/2}$ state. The measurements have been made possible by the development of a frequency doubled dye laser as UV source, delivering a high power in a very small bandwidth.

1.2 THE EXPERIMENTAL METHOD

The experimental investigation of radiative population transfer mechanisms is hindered by the fact, that the cosmic situation cannot be reproduced in all its aspects simultaneously in the laboratory. Mainly the factor time is responsible for this: the UV (electronic), near-infrared (vibrational) and far-infrared (rotational) cascade should be given time to complete. While the electronic decay is quite fast ($\tau \approx 10^{-6}$ s), the vibrational ($\tau \approx 10^{-2}$ s) and rotational ($\tau \approx 1-10$ s) cascades are relatively slow, which requires collision free path lengths of the order of at least 10 m to study the resulting population distribution in the ground state. Consequently a complete investigation of the UV induced population inversion mechanism in the laboratory is practically impossible. Therefore the present investigation is limited to the study of specific important aspects. A molecular beam set-up is used in order to resolve the Σ state hyperfine splittings and to avoid collisions disturbing the radiatively induced population transfer into the rotational levels in the direct decay from the $A^2\Sigma^+_{1/2}$ state. The molecular beam machine, a beam maser spectrometer (GOR 54), is essentially the same as described by ter Meulen

(MEU 76). The basic components of the UV source and the beam maser are shown in Fig. 1.2.

The hydroxyl radicals, produced in a reaction between H and NO_2, pass through the UV excitation region, an electrostatic state selector and two successive microwave cavities, where two different Λ-doublet transitions are induced (Chap. 4). The principle of operation of a beam maser is essentially the same as of the interstellar OH maser: stimulated transitions between levels with an inverted population distribution (Eq. 1-1). The main difference between the laboratory situation and interstellar space lies in the mechanism inverting the population distribution: in space the situation $n_u > n_l$ is achieved by some as yet unknown mechanism, in the laboratory by the use of an electrostatic state selector (a very unlikely mechanism for interstellar space). If the resonance frequency of the cavity equals the transition frequency a small increase of the microwave power reflected from the cavity occurs due to stimulation of transitions in the OH beam by the strong microwave field inside the cavity. This change in microwave intensity is detected by superheterodyne techniques to be described in Chap. 4.

In the state selector the OH beam passes through an inhomogeneous electric field $\vec{E}$, which, at a radial position $\vec{r}$, exerts a force $\vec{F}$ on the molecules:

$$\vec{F} = -\frac{dW}{dE}\frac{dE}{dr}\frac{\vec{r}}{r} \tag{1-3}$$

with W the molecular Stark energy. In the type of selector used in this investigation only the radial field gradient is large enough to be taken into account and $\frac{dE}{dr} > 0$. In all microwave transitions in OH the upper state has a positive Stark effect ($\frac{dW}{dE} > 0$), corresponding to a force directed towards the axis of the selector. The OH radicals in the upper state are therefore focused, whereas the molecules in the lower state ($\frac{dW}{dE} < 0$) are defocused by the selector. The net result is an occupation inversion of the molecules entering the microwave cavity (Chapt. 4).

With the present beam maser spectrometer signal to noise

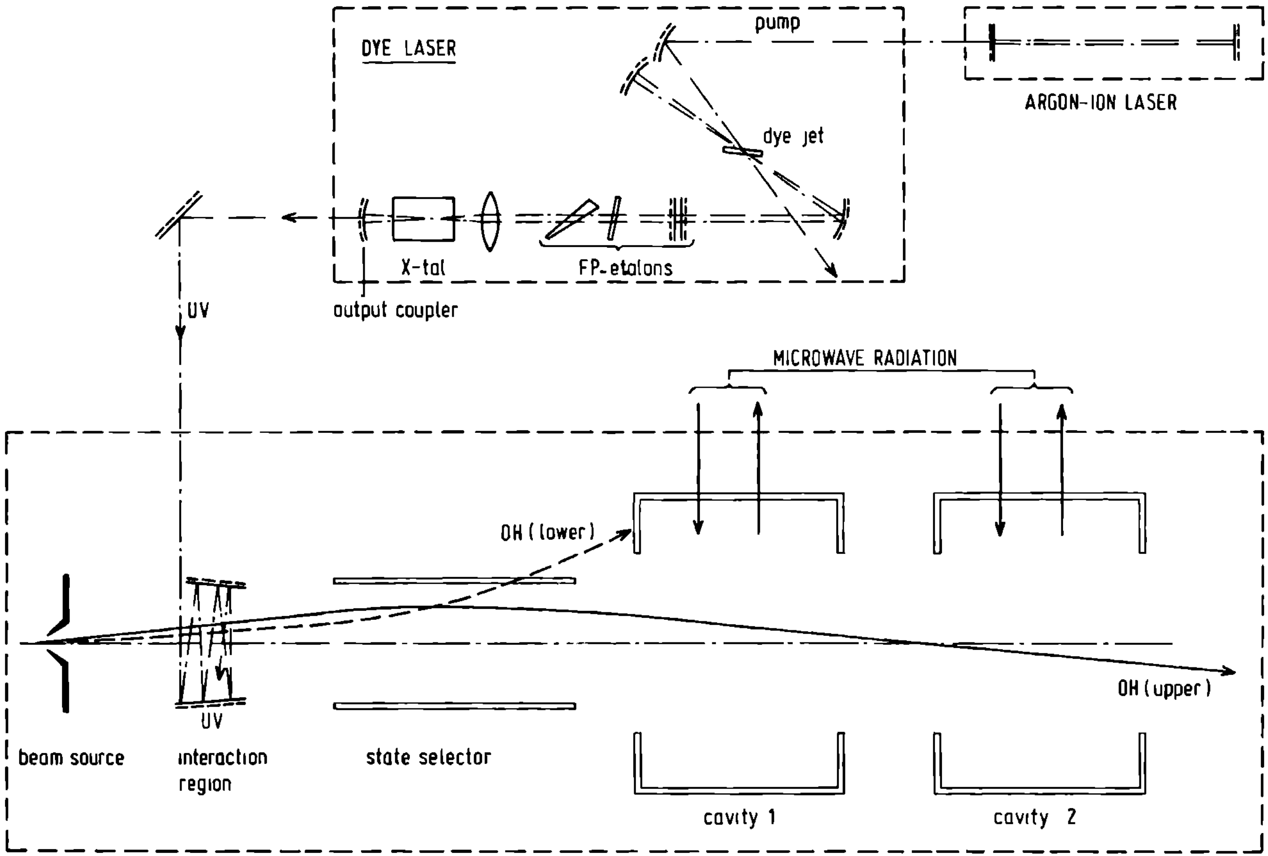

Fig. 1.2 Schematic view of the beam maser spectrometer and UV source. The curves shown in the beam maser are the trajectories of an upper and lower Λ-doublet state molecule.

ratios up to 100 at RC = 1 s are obtained after phase-sensitive detection, which is sufficient for the study of the UV induced population transfer proces in the beam maser. The hyperfine splittings of the $A^2\Sigma^+_{1/2}$ state are measured by monitoring the fluorescence intensity, produced in the decay of the Σ state, by means of an UV sensitive photo-multiplier tube, while sweeping the frequency of the UV source (Chap. 5).

The tunable UV radiation near 308 nm is produced by generation of the second harmonic of tunable dye laser radiation in the visible region (616 nm). For this purpose the light beam of the dye laser is focused into a nonlinear crystal made of Ammonium Dihydrogen Arsenate (ADA), which is temperature tuned, by means of a specially designed stable oven system, to obtain optimum conversion from the visible to UV. The dye laser is pumped by an argon-ion laser operating at 514.5 nm. By means of three specially coated Fabry-Perot type etalons, inserted into the dye laser cavity, the laser is forced to operate in only one single longitudinal mode. This single mode operation is required, because the hyperfine splittings to be resolved are of the same order of magnitude as the frequency distance between two adjacent modes. Scanning of the laser output frequency is accomplished by variation of the length of the laser cavity.

For second harmonic generation (SHG) either an extra-cavity or an intra-cavity frequency doubling set-up can be used. In the first case the nonlinear crystal is positioned outside the laser cavity. This is certainly the easiest method for SHG, because no interaction between the frequency doubling and lasing processes is present, permitting optimization of both processes separately. Experiments showed, that a single mode UV power of at most 2.5 μW could be obtained under stable operating conditions, which is far below the requirement for observable effects using microwave detection (Chap. 2). Because of the quadratic dependence of the generated UV power on the incident fundamental power, a substantial increase is expected, when the crystal is placed inside the dye laser cavity (intra-cavity operation), where the radiation field is much stronger. In this situation, however, the nonlinear medium imposes an additional loss to the fundamental radiation due to absorption, scattering and reflection, causing optimization of the entire set-up to be more complicated. The increase of single mode UV power, on the other hand, is quite dramatic: 0.2 mW stable UV is observed at 308 nm, which amply makes up for the extra effort.

In the course of the experiment stabilization of the UV frequency appeared to be necessary. Two active feedback loops, therefore, lock the frequency of the dye laser radiation to the transmission profile of a stable external reference cavity of the Fabry-Perot type and reduce the drift of the UV frequency by several orders of magnitude, leaving a residual drift < 100 MHz per hour, which is sufficient for our purpose. With this UV source the measurements of the hyperfine splittings of the $A^2\Sigma^+_{1/2}$ state of OH are performed at an average UV level of 60 μW permitting a stable frequency scan of 6 GHz in the UV. During the population transfer experiments scanning is not necessary and the UV source is operated at a maximum power level of 0.2 mW single mode. An extensive discussion of the principle of SHG and the construction of the frequency doubled dye laser is presented in Chap. 3.

Since 1972 Laser Induced Fluorescence (LIF) experiments on OH have been reported by several authors (BAA 72, BEC 72, BRO 74, HOG 74, WAN 74, GER 75, LEN 77, LIE 80). In all these experiments a pulsed frequency doubled dye laser was used to excite the OH either in a gas cell or in the atmosphere. In the present investigation, however, the first LIF measurements in the UV using a CW frequency doubled dye laser to excite the OH in a molecular beam set-up are presented.

CHAPTER 2

THE UV INDUCED POPULATION TRANSFER MECHANISM AND ITS EXPERIMENTAL INVESTIGATION

2.1 THE MOLECULAR PROPERTIES OF THE HYDROXYL RADICAL

The electronic properties of the hydroxyl molecule are determined by an open-shell configuration of its nine electrons, resulting in a non-zero orbital ($\vec{L}$) and spin ($\vec{S}$) electronic angular momentum. Because of the cylindrical symmetry of the molecular potential field about the internuclear axis, only the components $\Lambda(=0, \pm1, \ldots)$ and $\Sigma(=\pm\frac{1}{2})$ of $\vec{L}$ and $\vec{S}$, respectively, along this axis are quantized. Spin-orbit interaction couples Λ and Σ to the total electronic angular momentum $\Omega = \Lambda+\Sigma$ along the internuclear axis, which for the ground state ($\Lambda=\pm1$) of OH can take the values $|\Omega|=$ 1/2, 3/2. Of the two states $^2\Pi_{1/2}$ and $^2\Pi_{3/2}$ the latter has a lower energy. The end-over-end rotation $\vec{K}$ of the nuclei couples with Ω, resulting in an angular momentum $\vec{J}$ characterized by the quantum number $J=|\Omega|, |\Omega|+1, \ldots$. The degeneracy between the rotational states $+\Omega$ and $-\Omega$ is lifted by the interaction between $\vec{K}$ and $\vec{L}$, the phenomenon known as Λ-doubling. Interaction between the spin $\vec{I}$ ($=\frac{1}{2}$) of the hydrogen nucleus and the magnetic field generated by the electronic and rotational motion couple $\vec{I}$ and $\vec{J}$ to the total angular momentum $\vec{F}$, characterized by the quantum number $F=J\pm1/2$. An extensive theory of the wavefunction and energy level structure of the electronic ground state of OH is given by Dousmanis _et al_ (DOU 55), Meerts (MEE 75a) and Destombes _et al_ (DES 77, DES 77a). The resulting energy level scheme of the $X^2\Pi_\Omega$ state is shown in Fig. 2.1.

In the first excited electronic state $A^2\Sigma^+_{1/2}$ the electronic angular momentum Λ vanishes. Consequently the coupling scheme for this state is close to Hund's case (b): $\vec{K}$ and the electronic spin $\vec{S}$ couple to an angular momentum $\vec{J}$, the interaction known as the ρ-doubling phenomenon which splits each K level into a doublet with $J=K\pm1/2$. A further splitting of each J level is produced by

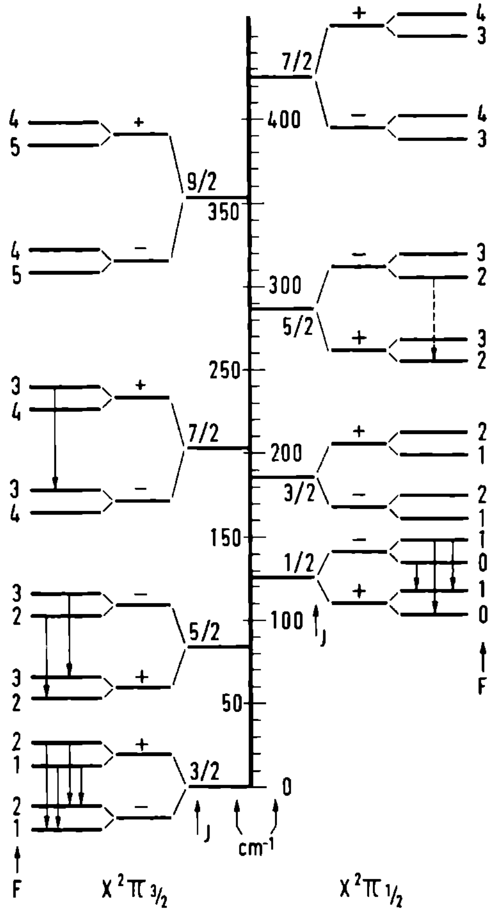

Fig. 2.1 The energy level scheme of the electronic ground state of OH. The arrows indicate the observed interstellar microwave emissions.

the hyperfine interaction. The wavefunctions of the rho-doublet hyperfine levels in Hund's case (b) representation are designated by $|^2\Sigma^+ K\ J = K \pm 1/2\ IFM_F>$.

The hyperfine splittings in both $X^2\Pi_\Omega$ and $A^2\Sigma^+_{1/2}$ states are of great importance to the UV induced population transfer mechanism proposed by Litvak (LIT 66): (partial) overlap due to Doppler broadening between adjacent hyperfine transitions may substantially influence the population transfer and the resulting relative occupation distribution between the ground state hyperfine levels. The hyperfine splittings in the rotational states up to $J = 7/2$ in $X^2\Pi_{1/2}$ and up to $J = 9/2$ in $X^2\Pi_{3/2}$, which are of interest to the transfer problem, are given in Table 2.1. From optical work by several authors (DIE 62, ENG 72) good data on the rotational and rho-doubling structure of the $A^2\Sigma^+_{1/2}$ state are available. Because the complete energy structure of the $^2\Pi$ ground state is very well known, only the hyperfine interaction in the $A^2\Sigma^+_{1/2}$ electronic state of OH will be discussed in some detail.

Hyperfine splittings in $X^2\Pi_\Omega,\pm$ states

J	$X^2\Pi_{1/2},+$	$X^2\Pi_{1/2},-$	$X^2\Pi_{3/2},+$	$X^2\Pi_{3/2},-$
1/2	90.414(5)	14.906(5)	-	-
3/2	11.838(7)	70.216(7)	53.17083(30)	55.12802(30)
5/2	71.536(7)	17.819(7)	18.346(7)	14.001(7)
7/2	23.609(7)	74.002(7)	7.4353(15)	0.6554(15)
9/2			12.3183(23)	21.3241(32)

Table 2.1 The hyperfine splittings in various rotational states of $X^2\Pi_{1/2}$ and $X^2\Pi_{3/2}$ according to Destombes et al (DES 77). Parity of states is identical to that used by ter Meulen (MEU 76). All splittings are given in MHz.

The Hamiltonian, containing the rotational, rho-doubling and hyperfine interactions, can be written as:

$$\underline{H} - B_\Sigma \underline{K}.\underline{K} + \gamma\underline{K}.\underline{S} + b\underline{I}.\underline{S} + c\underline{I}_Z.\underline{S}_Z \qquad (2\text{-}1)$$

The operators are defined in the molecular frame of reference, where the Z-axis is directed along the internuclear axis; B_Σ and γ represents the rotational and rho-doubling constant , respectively, while b and c are the hyperfine coupling constants as given by Frosch and Foley (FRO 52):

$$b = g_I\mu_o\mu_N\left\langle\frac{4}{3}\ \frac{\delta(r)}{r^2} - \frac{3\cos^2\chi-1}{r^3}\right\rangle_{av} \tag{2-2}$$

$$c = 3g_I\mu_o\mu_N\left\langle\frac{3\cos^2\chi-1}{r^3}\right\rangle_{av} \tag{2-3}$$

where the average has to be taken over the electronic space coordinates r and χ. In the expression for the Hamiltonian given above the interaction between the $A^2\Sigma^+_{1/2}$ and other electronic states, such as $X^2\Pi$ and $^2\Delta$, has been neglected as well as distortion effects, because these contributions to the energy are far below our experimental accuracy of ∿1 MHz. To evaluate the matrix elements of Eq. (2-1) it is most convenient to develop the Hund's case (b) wavefunctions in terms of Hund's case (a) equivalents. Following the phase convention of Freed (FRE 66) the correspondence is written as follows (MEE 71):

$$|^2\Sigma^+_{1/2}K\ J = K \pm 1/2\ IFM_F\rangle_b = |^2\Sigma^+_{1/2}JIFM_F\mp\rangle_a \tag{2-4}$$

where the right hand expression represents the symmetrized Hund's case (a) function. The reduction from $|^2\Sigma^+_{1/2}JIFM_F\mp\rangle_a$ to $|^2\Sigma^+_{1/2}JM_JIM_I\mp\rangle_a$ representation in evaluating the Hamiltonian matrix elements is done by application of spherical tensor operator techniques (JUD 63). The latter wavefunction can be decomposed into $|^2\Sigma^+_{1/2}JM_J\mp\rangle_a|IM_I\rangle$ with

$$|^2\Sigma^+_{1/2}JM_J\mp\rangle_a = \frac{1}{\sqrt{2}}[\,|\Lambda{=}0^+\rangle|S\Sigma\rangle|J\Omega M_J\rangle \mp |\Lambda{=}0^+\rangle|S{-}\Sigma\rangle|J{-}\Omega M_J\rangle] \tag{2-5}$$

and $S{=}\Sigma{=}\Omega{=}1/2$; $|\Lambda{=}0^+\rangle$ represents the electronic wavefunction of the Σ^+ state, while $|S\Sigma\rangle$ is the spin wavefunction of the unpaired electron. The rotational part $|J\Omega M_J\rangle$ can be expressed in terms of the rotational matrix elements:

$$|J\Omega M_J\rangle = \sqrt{\left(\frac{2J+1}{8\pi^2}\right)}\ D^{(J)}_{\Omega,M_J}(\alpha,\beta,\gamma) \tag{2-6}$$

The symmetry of the wavefunctions (2-4) under a reflection in a plane containing the internuclear axis (henceforth called symmetry operation P) is given by $(-1)^{K-1}$ for the Hund's case (b) function (MEE 71), corresponding to $(-1)^p(-1)^{J-1/2}$ for the case (a) equivalent having parity $p = \mp$. Using these wavefunctions, the matrix elements of (2-1) in Hund's case (b) representation can be shown to be nonzero if $\Delta F = 0$; $\Delta J = 0, \pm 1$; $\Delta K = 0, \pm 2$. The last rule is evident from the consideration that the Hamiltonian (2-1) is invariant under P while the Hund's case (b) wavefunctions have symmetry $(-1)^{K-1}$. The expressions for the matrix elements are (in agreement with Radford (RAD 64)):

$$\langle {}^2\Sigma^+_{1/2} K\ J=K-1/2\ I\ F=K-1\ |\underline{H}|\ {}^2\Sigma^+_{1/2}\ K-2\ J=K-3/2\ I\ F=K-1\rangle = -\frac{\sqrt{(K(K-1))}}{2K(2K-1)}\, c \qquad (2\text{-}7)$$

$$\langle {}^2\Sigma^+_{1/2} K\ J=K-1/2\ I\ F=K-1\ |\underline{H}|\ {}^2\Sigma^+_{1/2}\ J=K-1/2\ I\ F=K-1\rangle = B_\Sigma K(K+1) - \tfrac{1}{2}\gamma(K+1) - \frac{1}{4(2K-1)}\left[c-b(2K-1)\right] \qquad (2\text{-}8)$$

$$\langle {}^2\Sigma^+_{1/2} K\ J=K-1/2\ I\ F=K\ |\underline{H}|\ {}^2\Sigma^+_{1/2} K\ J=K-1/2\ I\ F=K\rangle = B_\Sigma K(K+1) - \tfrac{1}{2}\gamma(K+1) + \frac{1}{4(2K+1)}\left[c-b(2K-1)\right] \qquad (2\text{-}9)$$

$$\langle {}^2\Sigma^+_{1/2} K\ J=K-1/2\ I\ F=K\ |\underline{H}|\ {}^2\Sigma^+_{1/2} K\ J=K+1/2\ I\ F=K\rangle = \langle {}^2\Sigma^+_{1/2} K\ J=K+1/2\ I\ F=K\ |\underline{H}|\ {}^2\Sigma^+_{1/2} K\ J=K-1/2\ I\ F=K\rangle - \frac{\sqrt{K(K+1)}}{2(2K+1)}\,(2b+c) \qquad (2\text{-}10)$$

$$\langle {}^2\Sigma^+_{1/2} K\ J=K+1/2\ I\ F=K\ |\underline{H}|\ {}^2\Sigma^+_{1/2} K\ J=K+1/2\ I\ F=K\rangle = B_\Sigma K(K+1) + \tfrac{1}{2}\gamma K - \frac{1}{4(2K+1)}\left[c+b(2K+3)\right] \qquad (2\text{-}11)$$

$$\langle {}^2\Sigma^+_{1/2} K\ J=K+1/2\ I\ F=K+1\ |\underline{H}|\ {}^2\Sigma^+_{1/2} K\ J=K+1/2\ I\ F=K+1\rangle = B_\Sigma K(K+1) + \tfrac{1}{2}\gamma K + \frac{1}{4(2K+3)}\left[c+b(2K+3)\right] \qquad (2\text{-}12)$$

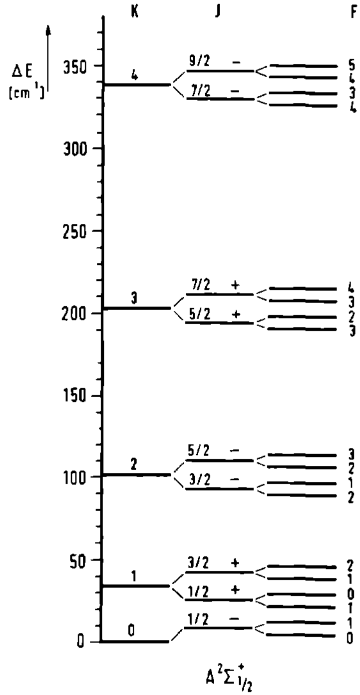

Fig. 2.2 The energy level structure of the $A^2\Sigma^+_{1/2}$ electronic state of OH.

The matrix element (2-7) gives a contribution to the energy of the $F = K-1$ or $F = K+1$ levels of a particular rotational state by a $\Delta K = \pm 2$ interaction and will therefore have only a small influence on the level energy. The other off-diagonal matrix element (2-10), however, describes the interaction between two hyperfine levels of the same rho-doublet and can therefore have a substantial effect on the energies of the levels. Recent values for B_Σ and γ are reported by Destombes et al (DES 77a): $B_\Sigma = 508.59(2)$ GHz and $\gamma = 6.81(2)$ GHz obtained from an extensive fit to existing data. German et al (GFR 73) report a somewhat higher value: $\gamma = 7.05$ GHz. Measured values of the hyperfine coupling constants in the $A^2\Sigma^+_{1/2}$ state are not reported in literature. From measurements on OD German et al estimated $\Delta\nu_{HF} = 227$ MHz and 509 MHz for the $J = 1/2$ and 3/2 levels, respectively, in the $K = 1$ state.

A schematic view of the energy level structure in the $A^2\Sigma^+_{1/2}$

state is shown in Fig. 2.2: the ordering of the hyperfine levels, shown here, is confirmed by a theoretical fit of the measured hyperfine splittings discussed in Chap. 5. Electric dipole transitions are allowed between the Σ and Π levels, according to the selection rules:

$$\Delta F = 0, \pm 1 \ , \ F = 0 \not\rightarrow 0 \ , \ \Delta J = 0, \pm 1 \ , \ \text{parity} \ + \leftrightarrow - \qquad (2\text{-}13)$$

Expressions for the dipole moment matrix elements for the $|A^2\Sigma^+_{1/2}, J'F'\rangle \rightarrow |X^2\Pi_\Omega, JF\rangle$ transitions are given by ter Meulen (MEU 76) together with an extensive list of spontaneous transition probabilities for these transitions. A survey of the values of the Einstein coefficients for spontaneous decay relevant to the astrophysical population transfer proces, with the exception of data on the UV transitions, is given by Destombes _et al_ (DES 77).

2.2 UV PUMPING IN INTERSTELLAR SPACE

2.2.1 THE POPULATION TRANSFER MECHANISM

A pumping mechanism based on the electronic excitation of OH by UV radiation near 308 nm was proposed by Litvak _et al_ (LIT 66) to explain the anomalous features of Class I OH sources. In this mechanism the UV radiation excites the OH from the ground $^2\Pi_{3/2}$, $v = 0$, $J = 3/2$ rotational level to the excited $A^2\Sigma^+_{1/2}$, $v = 0$ state via six (if hyperfine splitting is neglected) rotational transitions obeying the selection rules $\Delta J = 0, \pm 1$ and parity $+ \leftrightarrow -$. As a result of the subsequent decay back to the ground state via electronic, vibrational and rotational transitions, the upper and lower Λ-doublet levels are both populated, the amount depending on the number of intermediate levels involved in the cascade. The six excitation transitions can be divided into three groups: three strong transitions, two of them leaving from the upper Λ-doublet level and resulting in a net anti-inverting action; one weak anti-inverting transition and a group of two inverting lines of intermediate strength, both leaving from the lower Λ-doublet level. Selective absorption in the interstellar OH cloud determines the net effect: at small optical depths UV radiation at wavelengths corresponding to transitions of the first group is absorbed most strongly, resulting in a net anti-inverting effect. At intermediate optical depths, where the flux at wavelengths corresponding to the strong transitions is reduced to a negligible level, the last category dominates the population transfer proces giving an inversion of the population of the Λ-doublet levels. At larger optical depths only the UV radiation at the frequency corresponding to the weakly absorbing transition is left which again results in anti-inversion.

Litvak et al assumed the UV Doppler widths of the transitions to be larger than the hyperfine splittings in order to neglect their effect. In this case only an inversion of the Λ-doublet levels is obtained without any preference for a particular hyperfine state. As a consequence no anomalous intensity difference between the main line transitions ($\Delta F = 0$) can be expected when microwave transitions across the Λ-doublet are neglected. This is in contradiction with the observed preference for the upper $F = 1$ state as follows from the observed dominance of the 1665 MHz transition. If, however, the influence of these microwave transitions is included, a reduction of the produced population inversion occurs, which will be different for the 1665 and 1667 MHz line due to a slightly different line strength. Also the microwave intensity at the two transitions will be different (see Sect. 6.1) resulting in a greater quenching at the stronger transition, which in most cases is the $F = 2 \rightarrow 2$ line at 1667 MHz.

Turner (TUR 70) has shown that the inclusion of hyperfine structure, resulting in a total of 20 excitation transitions from $^2\Pi_{3/2}$, $J = 3/2$, may strongly influence the population transfer proces, when partial overlap occurs between adjacent hyperfine transition profiles due to Doppler broadening. The total transition scheme then obeys the selection rules $\Delta F = 0, \pm 1$ $\Delta J = 0, \pm 1$ and parity $+ \leftrightarrow -$. A part of this total scheme including decay from the $A^2\Sigma^+_{1/2}$ hyperfine sublevels is shown in Fig. 2.3. In the subsequent cascade down the $\Pi_{1/2}$ and $\Pi_{3/2}$ rotational ladders relaxation takes place to the initial states. At a temperature of 0.1 K the UV Doppler width (full width at half maximum height) already exceeds the ground state hyperfine splitting. Using the values of German <u>et al</u> (GER 73) for the hyperfine splittings in the $A^2\Sigma^+_{1/2}$, K = 1 state (227 and 509 MHz for the J = 1/2 and 3/2 levels, respectively) this overlap would occur here at 1.7 K and 8.6 K. The kinetic temperature of the OH formations is observed

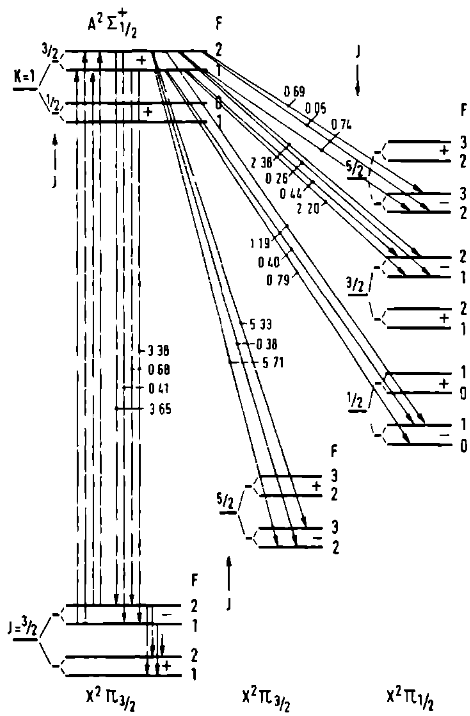

Fig. 2.3 Sample part of the total transition scheme for UV induced population transfer in OH: the $A^2\Sigma^+_{1/2}$, K = 1 $\leftarrow X^2{}_{3/2}$, J = 3/2 transition. The rotational cascade of the $X^2\Pi_\Omega$ levels is not shown. The numbers in the transitions are the spontaneous transition probabilities in units of $10^5\ s^{-1}$.

to be in the range from 10 K to 200 K (TUR 70), which makes the occurence of (partial) overlap in the $A^2\Sigma^+_{1/2}$ state quite probable. Furthermore, Turner's results indicate that under certain conditions of temperature and optical depth the observed dominance of the 1665 MHz transition can very well be explained by this effect. Exact values for the hyperfine splittings in the $A^2\Sigma^+_{1/2}$ state, however, were not available to Turner, whereas the balance between the gains of the $F = 1 \rightarrow 1$ and $F = 2 \rightarrow 2$ transitions turns out to depend quite strongly on the amount of overlap.

2.2.2 THE TRANSFER EQUATIONS

The equilibrium population density $N_i(s)$ of molecular energy level i at position s, in the presence of UV radiation and inelastic collisions between hydroxyl and surrounding molecules (primarily molecular hydrogen), is given by the well known rate equation for population transfer in a steady state:

$$\sum_{j>i} A_{ji}N_j(s) + \sum_{j\neq i} N_j(s)W_{ji}(s) + \sum_{j\neq i} C_{ji}N_j(s)$$
$$-N_i(s)\left[\sum_{j<i} A_{ij} + \sum_{j\neq i} W_{ij}(s) + \sum_{j\neq i} C_{ij}\right] = 0 \qquad (2\text{-}14)$$

Herein i and j run over all levels participating in the transfer proces: in $X^2\Pi_{3/2}$ up to $J = 9/2$, in $X^2\Pi_{1/2}$ up to $J = 7/2$, in $A^2\Sigma^+_{1/2}$ up to $K = 3$, $J = 5/2$ (microwave transitions across the Λ-doublets of the $\Pi_{1/2}$ and $\Pi_{3/2}$ states are left out of consideration in the one-dimensional model of the hydroxyl cloud used in this thesis); A_{ji} is the Einstein coefficient for spontaneous emission from level j to level i and C_{ji} the collisional transition rate from j to i. The radiative transition rate $W_{ji}(s)$ is given by:

$$W_{ji}(s) = B_{ji}\int_0^\infty g(\nu,\nu_{ji})\rho_\nu(s)d\nu \qquad (2\text{-}15)$$

where B_{ji} represents the Einstein coefficient for stimulated emission (or absorption if $j < i$); $g(\nu, \nu_{ji})$ is the Doppler broadened line shape function of the transition $j \rightarrow i$ centered at frequency $\nu_{ji} = (E_j - E_i)/h$ (expressions for the Einstein coefficients and $g(\nu, \nu_{ij})$ are given in Appendix 1); $\rho_\nu(s)$ represents the radiation density at position s and is related to the flux density $F_\nu(s)$ and the radiation intensity $I_\nu(s)$ by the relation (KRA 66):

$$\rho_\nu(s) = \frac{F_\nu(s)}{c} = \frac{1}{c} \int I_\nu(s) d\Omega \tag{2-16}$$

where the integral is to be taken over the solid angle of the incident radiation. For transitions between hyperfine levels in the absence of external static fields the relation between the radiative deexcitation rate $W_{ij}(s)$ and the excitation rate $W_{ji}(s)$ of Eq. (2-15) is:

$$g_i W_{ij}(s) = g_j W_{ji}(s) \tag{2-17}$$

Herein g_k is the degeneracy of level k.

The normalization equation, necessary to make the system of equations (2-14) independent is given by the conservation of total population density N_{OH}:

$$\sum_i N_i(s) = N_{OH} \quad ; \tag{2-18}$$

N_{OH} is assumed to be constant throughout the hydroxyl cloud.

The collisions introduced into the system (2-14) are defined such that, in the absence of any radiative proces, the final population densities will be thermally distributed. In this case the collisional excitation rate C_{ji} is related to the deexcitation rate C_{ij}, where i designates the upper state, by:

$$g_i C_{ij} = g_j C_{ji} e^{h\nu_{ij}/kT} \tag{2-19}$$

Assuming all downward collisional transition rates between magnetic sublevels to be equal to C, the collisional deexcitation rate C_{ij} becomes:

$$C_{ij} = g_j C \tag{2-20}$$

Using Eq. (2-19,20) the rate C is shown to be related to the total transition rate $C_{1t} = N_{H_2} \langle \sigma v \rangle$ out of level 1 (the lowest energy level), induced by inelastic collisions between OH and H_2, by the expression:

$$C = \frac{N_{H_2} \langle \sigma v \rangle}{\sum\limits_{i>1} g_i e^{-h\nu_{i1}/kT}} \tag{2-21}$$

Herein N_{H_2} represents the density of molecular hydrogen; v is the (thermal) relative velocity of the hydroxyl radicals and σ the total inelastic collision cross section for transitions out of level 1 and induced by OH-H_2 collisions. The average in Eq. (2-20) has to be taken over the velocity distribution of the hydroxyl radicals, which is assumed to be Maxwellian. As no information is available about the total collision cross section σ, we shall assume σ to be velocity independent and use $N_{H_2}\sigma$ as a parameter in the calculations.

The differential equation describing the change of UV intensity I_ν (measured in W/m^2Hz Sr) under unsaturated conditions along the direction of propagation is deduced from conservation of energy:

$$\frac{dI_\nu(s)}{ds} = - \alpha_\nu(s) I_\nu(s) + \varepsilon_\nu(s) \tag{2-22}$$

where $\alpha_\nu(s)$ and $\varepsilon_\nu(s)$ represents, respectively, the total absorption coefficient and source function at frequency ν; in general both contain contributions from various transitions if overlap occurs due to Doppler broadening. In terms of the population densities N_i of the levels involved, these contributions are given by (Appendix 1):

$$\alpha_\nu(s) = \sum_{j<i} \alpha_{ji}(\nu,s) = \sum_{j<i} \frac{h\nu}{c} B_{ji} g(\nu,\nu_{ji}) \left[N_j(s) - \frac{g_j}{g_i} N_i(s)\right] \tag{2-23}$$

$$\epsilon_\nu(s) = \sum_{j<i} \epsilon_{ij}(\nu,s) = \sum_{j<i} \frac{h\nu}{4\pi} A_{ij} g(\nu,\nu_{ij}) N_i(s) \tag{2-24}$$

Herein the upper level is designated by i. In this derivation the spontaneous emission is considered to be isotropic. As can be seen from an inspection of a two level transition scheme (Appendix 1), the ratio $\epsilon/\alpha I$ will be in the order of $\Delta\Omega/4\pi$, where $\Delta\Omega$ is the solid angle of the incident radiation. Taking as UV source an O-type star ($R_* \simeq 10\ R_0$, $T \sim 70{,}000$ K) at a distance of 2ly, which is a reasonable assumption (LIT 66), this ratio becomes $\sim 10^{-13}$ indicating that the emission term in Eq. (2-22) can be neglected. In this case the intensity is given by:

$$I_\nu(s) = I_\nu(0)\exp[-\tau_\nu(s)] = I_\nu(0)\exp[-\int_0^s \alpha_\nu(s)ds] \tag{2-25}$$

where $\tau_\nu(s)$ represents the total optical depth at frequency ν and consists of contributions from several transitions via the total absorption coefficient given in Eq. (2-23). The excitation rate is then given by:

$$W_{ji}(s) = B_{ji} \frac{F_\nu(0)}{c} \int_0^\infty g(\nu,\nu_{ji})\exp[-\tau_\nu(s)]d\nu \tag{2-26}$$

Herein $F_\nu(0)$ represents the flux density incident on the hydroxyl formation and is taken equal for all UV transitions. Using Eq. (2-23,25,26) and assuming a Gaussian line shape the excitation rate $W_{ij}(s)$ at transition $i \rightarrow j$ and position s can be calculated once the population densities at s are known. Overlap between different UV transition profiles is included via the line-shape factors $g(\nu,\nu_{kl})$ (with $\nu_{kl} \neq \nu_{ij}$), which are contained in the expression for the total optical depth $\tau_\nu(s)$.

With the help of the relations given above the population transfer due to UV transitions and collisions is calculated. The distance inside the OH formation relative to the front is measured in terms of the optical depth τ at line center of the $A^2\Sigma^+_{1/2}$, K = 1, J = 3/2, F = 2,+ ← $X^2\Pi_{3/2}$, J = 3/2, F = 2,- transition at 307.934 nm and is determined under thermal equilibrium conditions and neglect of overlap with other transitions. The effect of population transfer on the microwave intensity is determined via a calculation of the relative gain factor G_{ij} at the considered microwave transition (the negative absorption coefficient at line center) given by:

$$G_{ij}(\tau) = - \frac{h\nu_{ij}}{c} B_{ij} \frac{2}{\Delta\nu_{ij}} \sqrt{(\frac{\ln 2}{\tau})} \frac{1}{N_{OH}} [N_i(\tau) - \frac{g_i}{g_j} N_j(\tau)] \quad (2\text{-}27)$$

where N_{OH} is the total OH density and is assumed to be constant throughout the cloud and i and j represents the upper and lower level, respectively, of the considered microwave transition.
The population inversion ΔN_{ij} is given by:

$$\Delta N_{ij} = 2 \frac{N_i(\tau)/g_i - N_j(\tau)/g_j}{N_i(\tau)/g_i + N_j(\tau)/g_j} \quad (2\text{-}28)$$

The iterative procedure used to calculate G and ΔN runs as follows:

from the values obtained at smaller optical depths the population densities are linearly extrapolated to depth τ for each level. These values are then used to calculate the radiative transition rates W at τ, which, when inserted into (2-14), give corrections to the extrapolated densities. If necessary, this procedure is repeated until the corrections to be applied at depth τ are smaller than some predetermined value (typically 10^{-2}%). If so, the entire procedure is applied to the next optical depth. As starting values for N_i at the front of the OH cloud the thermal population densities are used. In the one-dimensional model of the OH cloud, used in this thesis, population transfer due to microwave transitions across the Λ-doublets is not incorporated and back-scattered UV radiation is not taken into account,because the spontaneous emission is assumed to be negligible relative to the stimulated UV processes.

The approach followed by Turner (TUR 70) deviates from ours in a number of points:

1. A rectangular line profile is used by Turner, rather than the Gaussian shape adopted in our calculations.
2. The hyperfine splitting in the Σ state is probably determined from the first order perturbation theory using the hyperfine Hamiltonian $H_{hfs} = b\underline{I}.\underline{S}$ with $b = 1420\xi$ MHz and ξ the unknown ratio of the hyperfine splitting in the $A^2\Sigma^+_{1/2}$, $K = 0$ state to the hyperfine splitting of the H atom in its ground state (in Turner's calculations $\xi \simeq 1/2$ is assumed). If, in addition, the Doppler width in Turner's calculation is taken one half the value used in our calculations, the various hyperfine splittings in the $A^2\Sigma^+_{1/2}$ state start to overlap ($\Delta\nu_D > \Delta\nu_{HF}$) at $T/\xi^2 = 267$ for the $K = 0$ state and at $T/\xi^2 = 119$ and 96.3 for the upper rho-doublet levels of the $K = 1,2$ rotational states, respectively. For the lower rho-doublet levels of the $K = 1,2,3$ states the results are $T/\xi^2 =$ 29.7, 42.8 and 49.1, respectively. In his paper Turner gives for T/ξ^2 the values 29.7, 42.7, 54.1, 90.4, 119 and 267 for successive overlap, but does not explain how these values were derived.

If a rectangular line shape with the correct width at $T = 4.5$ K is inserted into the present model, the results for the relative gain factors shown in Fig. 2.4 (without the effect of collisions) are obtained. At this temperature no overlap occurs between the various transitions to different hyperfine levels in the $A^2\Sigma^+_{1/2}$ state. The hyperfine splitting is determined according to Turner's method; the spontaneous transition probabilities are calculated from the expressions for the dipole moment matrix elements given by ter Meulen (MEU 76), assuming a value of $f_{00} = 1.03\times10^{-3}$ for the oscillator strength of the $\Sigma, v' = 0 \rightarrow \Pi, v = 0$ band (DIM 79). For a schematic view of the 20 hyperfine transitions to the $A^2\Sigma^+_{1/2}$ state the reader is referred to Fig. 6.4. The results, obtained by Turner in this situation, are shown also in Fig. 2.4 assuming an OH density of 10^5 m^{-3} (Turner gives the absolute gain factors of the four ground state microwave transitions) and reveal clear

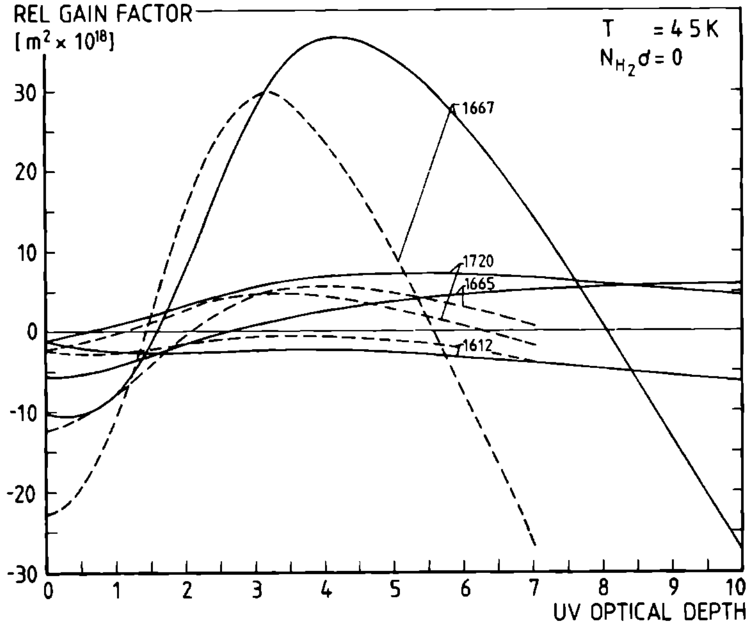

Fig. 2.4 The relative gain factors of the four ground state microwave transitions versus optical depth at $T = 4.5$ K in the absence of collisions and according to the model of Turner (TUR 70) with a rectangular absorption line profile. The solid curves are the results of the present investigation; the dashed curves represent Turner's calculations assuming $N_{OH} = 10^5\ m^{-3}$.

discrepancies with our results, the most striking being the apparent difference in optical depth scale and the dicrepancy in the values at $\tau = 0$. Moreover, our result for the relative gain factor at 1665 MHz appears to be somewhat less favorable than that of Turner. Similar differences, especially the optical depth scale and the relative magnitude of the result at 1665 MHz, are also observed at higher temperatures, where overlap between UV transitions to different hyperfine levels in the $A^2\Sigma^+_{1/2}$ state is not negligible. No definite causes for these discrepancies could be found, however, because of various uncertainties in Turner's model:

- The results obtained by Turner at $\tau = 0$ are constant throughout the various regions of T/ξ^2. Because the gain factors at $\tau = 0$ are temperature dependent through the linewidth, this constancy suggests that his results are probably obtained at a fixed temperature, which, however, would be in contradiction with his statement: $\xi \simeq \frac{1}{2}$.
- In earlier work (TUR 67) the values of the Einstein A coefficients for various transitions are not correct. It is, however, not clear whether these errors are also present in later work (TUR 70).
- From the information supplied with his results no definite identification of the transitions determining the optical depth scale is possible, whereas also a difference in linewidth seems to be present in Turner's model.
- The model for population transfer by collisions with hydrogen and electrons, results of which are included in the paper, is not specified.

If the observer's line of sight is perpendicular to the UV pumping direction, the observed microwave radiation in each of the four transitions will mainly come from the region with maximum gain factor. In this situation, the dominance of the 1665 MHz emission in the observations cannot be explained. In the parallel pumping geometry the gain at 1665 MHz only exceeds the value at 1667 MHz for $\tau > 10$. The 1720 MHz emission, however, should be of comparable magnitude, which is never observed in reality. Results of extensive calculations using a Gaussian line shape and the exact hyperfine structure will be presented in Chap. 6.

2.3 THE REQUIRED UV SOURCE

From the estimated values of the hyperfine splittings of the $A^2\Sigma^+_{1/2}$, $K = 1$, $J = 1/2$, and $J = 3/2$ states, being 227 MHz and 509 MHz, respectively (GER 73), it is clear that the bandwidth of the UV radiation should be lower than 100 MHz if the splittings are to be resolved. Moreover, the source should be tunable over the region 305-309 nm where the most interesting transitions to the $A^2\Sigma^+_{1/2}$ state are situated (MEU 74). If a single mode laser source is used to generate the UV, the radiation bandwidth is generally determined by the frequency jitter of the laser mode during times in the order of 10^{-4}-10^{-6} s, the time of flight of the OH radicals through the interaction region. As shown by Hemminger *et al* (HEM 77) the effective linewidth of a single mode dye laser is then in the order of 50 kHz. The bandwidth requirement given above is met if the center frequency drift can be kept below 100 MHz during the measuring time of approximately 1 h, which requires active stabilization of the laser frequency.

The required intensity of the UV radiation source is determined from the change in population density of the ground state hyperfine levels, which has to be generated to produce a detectable effect on the intensity of the microwave transitions. For this purpose a three-level proces is investigated: population is transferred from state $|1\rangle$ in $X^2\Pi_{3/2}$ to state $|2\rangle$ in $A^2\Sigma^+_{1/2}$ by UV excitation and is followed by a decay of $|2\rangle$, which also transfers via spontaneous emission population to a state $|3\rangle$ in $X^2\Pi_{3/2}$. These transfer effects are then measured by monitoring the population of states $|1\rangle$ and $|3\rangle$. A quantum mechanical description of such a three-level proces, analogous to the Rabi theory for a two-level system, is very complicated because of the presence of spontaneous decay. The spontaneous emission contributes to the population transfer both by offering different pathways for the decay and by determining the width of the excited state, and thereby the excitation efficiency. The equivalence between the Einstein and Rabi approaches to the problem of interaction between a single mode radiation field and a two-level atomic system will be demonstrated for small excitation rates. This justifies the use of the semi-classical Einstein theory, which also takes into account population transfer by spontaneous processes, to the three-level system in the case of small excitation efficiencies.

In the Rabi approach all levels involved are assumed to have infinite lifetime when no radiative excitation is applied. The probability $|c_2(t)|^2$ for finding the atomic system in the upper state, due to excitation by a radiation field $E\cos(\omega t)$ and assuming $|c_1(0)|^2 = 1$, is given by the well-known expression:

$$|c_2(t)|^2 = \frac{\Omega^2}{(\omega-\omega_1)^2 + \Omega^2} \sin^2\{\tfrac{1}{2}t[(\omega-\omega_1)^2 + \Omega^2]^{\frac{1}{2}}\} \qquad (2\text{-}29)$$

Herein ω_1 represents the atomic transition frequency and Ω the strength of the interaction:

$$\Omega^2 = \overline{|\vec{\mu}_{12}.\vec{E}|^2}/\hbar^2 = 4B_{12}I/c \qquad (2\text{-}30)$$

where $\vec{\mu}_{12}$ is the matrix element of the dipole moment operator between the initial and final states and I represents the intensity of the radiation field related to E by $I = \tfrac{1}{2}\varepsilon_0 cE^2$. The horizontal bar in Eq. (2-30) denotes averaging over the orientation of $\vec{\mu}_{12}$ (assumed to have an isotropic distribution of direction) with respect to $\vec{E}$. In practise, however, the upper level will have a spectral width $\Delta\omega_0$. This is incorporated by integration of Eq. (2-29) over the line shape $g(\omega_1,\omega_0)$ of the upper level, which is essentially Lorentzian with center frequency ω_0 and width $\Delta\omega_0$:

$$\overline{|c_2(t)|^2} = \Omega^2 \int_0^\infty \frac{\sin^2\{\tfrac{1}{2}t[(\omega-\omega_1)^2 + \Omega^2]^{\frac{1}{2}}\}}{(\omega-\omega_1)^2 + \Omega^2} g(\omega_1,\omega_0)d\omega_1 \qquad (2\text{-}31)$$

with

$$g(\omega_1,\omega_0) = \frac{\Delta\omega_0/2\pi}{(\omega_1-\omega_0)^2 + (\tfrac{1}{2}\Delta\omega_0)^2} \qquad (2\text{-}31a)$$

If the width $\Delta\omega_0$ of the upper level is much larger than the line-width given by the finite time of flight t through the UV interaction region, the variation of $g(\omega_1,\omega_0)$ is slow compared to the remainder of the integrand and may therefore be fixed at $(\tfrac{1}{2}\Delta\omega_0)^{-2}$ in case of resonant excitation ($\omega = \omega_0$). Numerical evaluation of the integral in Eq. (2-31) for various values of $\beta = \tfrac{1}{2}\Omega t$ under the condition $\Delta\omega_0 t \gg 1$ then shows that $\overline{|c_2(t)|^2}$ is very well approximated by:

$$\overline{|c_2(t)|^2} = \frac{2\Omega}{\Delta\omega_0}\,\frac{\sin^2\beta}{\beta} \xrightarrow[\beta<<1]{} \frac{\Omega^2 t}{\Delta\omega_0} \tag{2-32}$$

where the limit is valid for low excitation rates (not for small t because of the requirement $\Delta\omega_0 t>>1$). In the Einstein theory this result should be compared to the case, where the upper level has spectral width $\Delta\omega_0$ and population transfer to the lower level by spontaneous emission is negligible. For low excitation efficiencies $W_{12}t$ the fraction $\overline{|c_2(t)|^2}$ of population in the upper level at time t is given:

$$\overline{|c_2(t)|^2} = W_{12}t = \frac{4B_{12}It}{c\Delta\omega_0} \tag{2-33}$$

where Eq. (2-15,16) are used in the last step and the bandwidth of the single mode radiation field is assumed to be much smaller than the width $\Delta\omega_0$ of the Lorentzian profile of the molecular absorption line. From this and Eq. (2-30) it is clear that in a two-level system, neglecting population transfer due to spontaneous processes, both the Einstein and Rabi approaches produce identical results in the case of low excitation rates. We will therefore assume the Einstein theory to be adequate also for the three-level proces, provided the excitation rates in the UV beam remain low.

The required intensity of the UV radiation is determined by calculating the change in flow of molecules in a certain state through the microwave cavity as a result of the UV excitation. This change is then compared with the minimum value required for observable effects on the microwave intensity. Within times of interest in the beam maser ($t < 10^{-3}$ s) only the electronic decay in OH is sufficiently fast to be taken into account. At the entry of the microwave cavity the population present in state |2> at the exit of the radiation zone has totally decayed due to the relatively large distance of approximately 40 cm between the cavity and the radiation zone. The decay of state |2> not only transfers population to $|3>$ but also to various other states (designated by $i = 4,5,\ldots$) in the way described in Appendix 3. These alternative decay routes from state $|2>$ have to be taken into account to determine the required UV intensity. According to the Einstein theory for such a multi-level system, discussed in Appendix 3, the UV induced relative changes R_1, given by Fq.(A3-9), and R_i in population density of states $|1>$ and $|i>$ ($i \geq 3$) respectively, at the entrance of the microwave cavity are related by Eq. (A3-11), which in the case of a Maxwellian population distribution without UV excitation reads:

$$\frac{R_i}{R_1} = - \frac{g_1 A_{2i}}{g_i (A - A_{21})} \exp(-h\nu_{1i}/kT) \qquad (2\text{-}34)$$

Herein g_1 and g_i are the degeneracies of states $|1>$ and $|i>$. However, due to the divergence θ_m of the molecular beam, assumed to have uniform velocity v, the UV excitation rate W_{12} changes considerably across the OH beam profile due to a Doppler shift of the absorption line center frequency. Assuming a Lorentzian absorption profile of full width $\Delta\nu$, the excitation rate $W_{12}(\theta)$ of molecules emerging from the source at an angle θ relative to the OH beam axis, is given by:

$$W_{12}(\theta) = \frac{2B_{12}I}{\pi c \Delta\nu} \Big/ \left[1 + \left(\frac{\nu_L - \nu(\theta)}{\frac{1}{2}\Delta\nu} \right)^2\right] \qquad (2\text{-}35)$$

with $\nu(\theta) = \nu_0(1 - \frac{v}{c}\sin(\theta))$ the Doppler shifted frequency of the absorption line and ν_L the frequency of the narrow band UV source ($\Delta\nu_L << \Delta\nu$). To obtain the relative change in total flow Φ_i of molecules in state $|i>$, passing through the microwave cavity, the contributions of individual parts of the molecular beam have to be averaged, yielding:

$$\frac{\Delta\Phi_i}{\Phi_i} = \frac{4H}{\pi D} \frac{1}{2\tan\theta_m} \int_{-\tan\theta_m}^{\tan\theta_m} R_i(W_{12}(\theta))\, d(\tan\theta) \quad i \neq 2 \qquad (2\text{-}36)$$

Here D and H (<<D) represent the thickness of the molecular and

UV beams, respectively, at the interaction region; the factor $\frac{4H}{\pi D}$ represents the fraction of molecules in the OH beam, that is irradiated by the square UV beam.

To determine the required UV intensity we consider the three-level system: $X^2\Pi_{3/2}$,J=3/2,F=2,− → $A^2\Sigma^+_{1/2}$,J=3/2,F=2,+ → $X^2\Pi_{3/2}$,J=5/2, F=3,− where $A=14.33\times10^5\ s^{-1}$, $A_{21}=3.65\times10^5\ s^{-1}$, $A_{23}=5.33\times10^5\ s^{-1}$ and $B_{12}=6.41\times10^{17}\ m^3J^{-1}s^{-2}$. If we assume the minimum detectable relative flow changes by the microwave spectrometer to be about 1×10^{-3} for both $\Pi_{3/2}$ levels (which is obtainable by long time integration techniques), a parallel UV beam of 1×1 mm^2 cross section, $\nu_o=9.7\times10^{14}$ Hz, v = 717 m/s, D = 5 mm and $\theta_m=1.5°$ then the minimum required UV powers are about 0.3 mW and 1 mW for detection of effects on the $^2\Pi_{3/2}$,J = 3/2,F = 2 → 2 and J = 5/2, F = 3 → 3 microwave transitions, respectively,produced in a single traversal of the molecules through the UV beam. At 0.3 mW UV, however, the excitation efficiency $W_{12}(0)T=1.2$ in the center of the OH beam, indicating that saturation effects will occur. In this region the theory presented above is no longer applicable and the population transfer will decrease. A more effective use of the available UV power is application of a reflection system such that different sections of the OH beam are excited in each passage through the UV beam. This is accomplished by a slight tilt of the mirrors of the reflection system (Chap. 4). At a UV power of 0.1 mW a minimum of 10 reflections is then necessary to produce a detectable effect on the J = 5/2 microwave transition. The application of highly reflective dielectric coatings on the mirrors make a number of more than 50 reflections possible. From these figures we conclude to a required UV power of at least 0.1 mW single mode (depending on the quality of the reflection system) if population transfer effects to other rotational states are to be investigated.

CHAPTER 3

THE UV SOURCE

3.1 SECOND HARMONIC GENERATION

3.1.1 THEORY

The UV radiation necessary in the hyperfine and population transfer experiments is produced by second harmonic generation (SHG) of visible dye laser radiation in a nonlinear crystal placed inside the laser cavity. This method can provide both the desired tunability and high spectral power density if the laser is operating in one single longitudinal mode of the cavity.

The SHG is performed in a uniaxial nonlinear crystal belonging to the symmetry class $\bar{4}2m$ and having negative birefringence. In these media the refractive index $n_{ord}(\omega,\theta)$ for the ordinary ray at angular frequency ω, polarized perpendicularly to the plane defined by the optic axis (OA) and the wave vector $\vec{k}$, is independent of direction and equal to $n_o(\omega)$ (Fig. 3.1). The refractive index for the extra-ordinary ray $n_{ext}(\omega,\theta)$, polarized in the plane through $\vec{k}$ and OA, in the direction θ relative to the optic axis is given by the relation (YAR 75):

$$n_{ext}^{-2}(\omega,\theta) = n_o^{-2}(\omega)\cos^2\theta + n_e^{-2}(\omega)\sin^2\theta \qquad (3-1)$$

where $n_e(\omega)$ represents the index of the extra-ordinary ray in a direction normal to the optic axis of the medium; in negative uniaxial crystals $n_e(\omega) < n_o(\omega)$. Contrary to the ordinary ray the directions of phase propagation $\vec{k}$ and energy flow $\vec{S}$ of the extra-ordinary ray are not parallel (BOR 59). The angle ρ between these directions, referred to as the double refraction angle, is given by:

$$\tan\rho = -\frac{n_o^2(\omega) - n_e^2(\omega)}{n_e^2(\omega) + n_o^2(\omega)\tan^2\theta}\tan\theta \qquad (3-2)$$

Optimum conversion efficiency in a collinear SHG proces is

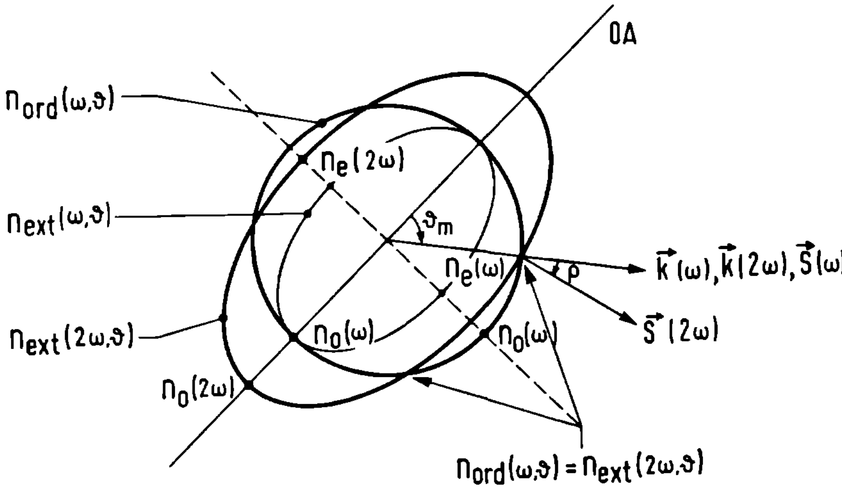

Fig. 3.1 The index surfaces in negative uniaxial nonlinear crystals at the fundamental and second harmonic frequencies. The phase-matching angle θ_m relative to the optic axis (OA) and the double refraction angle ρ between the wave vector $\vec{k}$ and the Poynting vector $\vec{S}$ at the second harmonic frequency are indicated.

expected when, in the direction θ, the momentum mismatch $\Delta k = 2k(\omega) - k(2\omega)$ between the incident (fundamental) wave, having momentum $k(\omega)$, and the generated second harmonic wave, at momentum $k(2\omega)$, vanishes. This occurs only, if the corresponding refractive indices for phase propagation in the direction θ are equal. Due to the fact that $dn/d\lambda < 0$ for all transparent media, this requirement is only met, if the fundamental and second harmonic waves have orthogonal polarizations, the fundamental being the ordinary wave in negative uniaxial crystals as illustrated in Fig. 3.1. The type of phase matching in which an ordinary fundamental wave interacts with itself to produce an extra-ordinary second harmonic output is called type I phase matching. The angle θ_m at which Δk vanishes follows from Eq. (3-1):

$$\sin^2\theta_m = \left[\frac{n_e(2\omega)}{n_o(\omega)} \right]^2 \frac{n_o^2(2\omega) - n_o^2(\omega)}{n_o^2(2\omega) - n_e^2(2\omega)} \qquad (3\text{-}3)$$

Destructive interference of the produced UV due to the double refraction severely limits the efficiency of the SHG proces by restricting the contributing part of the crystal to a fraction of its length. Optimum efficiency of the SHG proces occurs when phase matching is achieved in a direction perpendicular to the optic axis (θ_m=90°, ρ=0). This situation, employed in our experiment, is called noncritical or 90° phase matching, because the orientation of the crystal relative to the fundamental beam is not critical, since the index surfaces of both beams are just tangential. Temperature tuning of the crystal has to be employed to obtain phase matching (Δk=0) in this situation. Curves of the fundamental wavelength λ_{nc} versus noncritical phase-matching temperature are shown in Fig. 3.2 for various uniaxial crystals (QTL 74). The slopes of these curves are given by the relation:

$$\frac{d\lambda_{nc}}{dT} = - \frac{\frac{d}{dT}\left[n_o(\lambda_{nc}) - n_e(\tfrac{1}{2}\lambda_{nc})\right]}{\left(\frac{dn_o}{d\lambda}\right)_{\lambda_{nc}} - \tfrac{1}{2}\left(\frac{dn_e}{d\lambda}\right)_{\lambda_{nc}}} \tag{3-4}$$

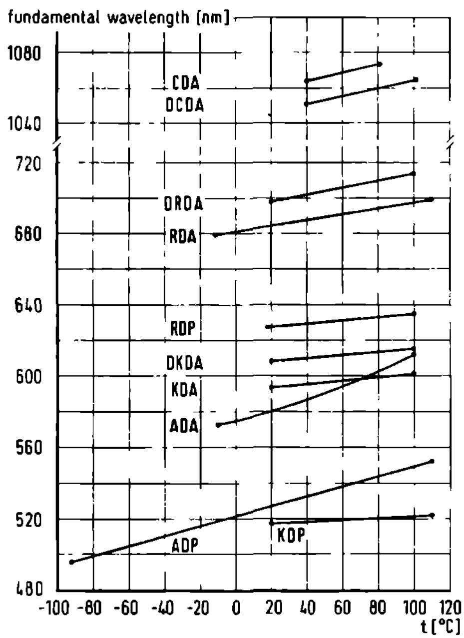

Fig. 3.2 The fundamental wavelength at noncritical phase matching versus operating temperature for various crystals of symmetry class $\bar{4}2m$.

The nominator of the righthand side is henceforth called the temperature coefficient of birefringence. For most crystals of $\bar{4}2m$ symmetry refractive index information is available in the visible range. In the UV region, however, hardly any good data are known, with the exception of KDP and ADP, for which dispersion relations are given by Zernicke (ZER 64) in the region 0.2-1.5 μ. Table 3.1 summarizes properties of some nonlinear uniaxial crystals of class $\bar{4}2m$ showing negative birefringence. Because of the lack of UV data, needed to evaluate the phase-matching and double refraction parameters, only references to index data are listed.

Due to a nonlinear susceptibility in the medium the polarization, induced by the electric field of the fundamental light wave, contains a contribution $\vec{P}_{SH}$ at 2ω given by (MID 65):

$$P_{SH}(2\omega) = \epsilon_o \sum_{j,k} d_{ijk}(2\omega,\omega,\omega)E_j(\omega)E_k(\omega) \qquad (3\text{-}5)$$

where d_{ijk} represents a component of the tensor $\underline{\underline{d}}$ of rank 3 describing the nonlinear susceptibility of the medium and $E_j(\omega)$ is the j-th component of the fundamental electric field in the crystallographic system of axes. In uniaxial crystals the optic axis coincides with the Z-axis of this system. The shape of the tensor $\underline{\underline{d}}$ is determined by symmetry conditions. In case of uniaxial crystals of class $\bar{4}2m$ the $\underline{\underline{d}}$ tensor can be contracted into a 3×6 matrix representation, in which only the elements d_{36} and $d_{25}=d_{14}$ are non-zero (MID 65). Values of d_{36}, relative to KDP (KH_2PO_4), for various crystals of this class, are given in Table 3.1. To convert to absolute quantities $d_{36}(KDP)=4.7(3)\times10^{-13}$ m/V [1)] should be used (SIN 71). Only the component of $\vec{P}_{SH}$ parallel to the electric field of the second harmonic wave contributes to a growing wave (MIE 76). This permits the definition of an effective nonlinear susceptibility d_{eff} by the relation:

1. To convert from CGS to SI units, the former are to be multiplied by $\frac{4\pi}{c}\times10^4$. This applies only when $\underline{\underline{d}}$, in the SI system, is defined by Eq. (3-5), which differs from the definition of Yariv (YAR 75).

$$P^{c}_{SH} = \varepsilon_o d_{eff} E^2(\omega) \tag{3-6}$$

where only scalar magnitudes of vectors are used; P^{c}_{SH} represents the contributing part of the induced second order polarization and, for a type I SHG proces in negative uniaxial crystals, d_{eff} is given by the expression:

$$d_{eff} = -\, d_{36} \sin(\theta+\rho) \sin 2\phi \tag{3-7}$$

Herein ρ represents the double refraction angle at the second harmonic frequency; the angles (θ, ϕ) are the polar angles of the wave vector $\vec{k}(\omega)$ of the fundamental beam inside the medium in the crystallographic system of axes as shown in Fig. 3.3. Equation (3-7) differs from the expression given by Midwinter and Warner (MID 65) in the occurrence of the double refraction angle ρ, which in

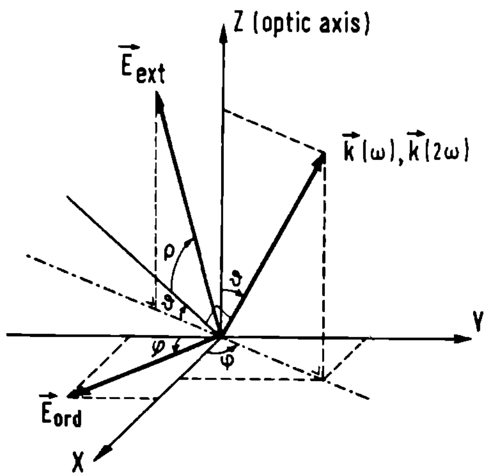

Fig. 3.3 The ordinary and extra-ordinary rays in the crystallographic system of axes (X,Y,Z). Note that $\vec{E}_{ext}$, situated in the plane through $\vec{k}$ and the optic axis, is not normal to $\vec{k}$, in contrast to non-birefringent media.

crystal		transparency range 3) [μm]	d_{36} 4)	$\frac{d}{dT}[n_e(2\omega)-n_o(\omega)]$ 5) $[10^{-5}\ K^{-1}]$		thermal conductivity $[Wm^{-1}K^{-1}]$		refractive index reference	absorption coef. (visible) $[m^{-1}]$ 5)	
KDP	KH_2PO_4	0.2-1.5	1	0.86(5)	PHI 66	1.9	SUE 67	ZER 64, QTL 71a		
D-KDP	KD_2PO_4	0.2-1.5	0.91(3)	0.63(3)	PHI 66			SIN 71, SUV 67	0.6	ADH 74
ADP	$(NH_4)H_2PO_4$	0.2-1.5	1.21(5)	3.9 (1)	PHI 66	0.71//OA 1.3 ⊥ OA	AIP 63	ZER 64, QTL 71a	2.4	BOY 65
D-ADP	$(NH_4)D_2PO_4$		1.10					SUV 67		
KDA	KH_2AsO_4		1.12(5)			1.9	SUE 67	ADH 68, QTL 71	6)	ADH 68
D-KDA	KD_2AsO_4							ADH 68	0.8 (1)	1)
ADA	$(NH_4)H_2AsO_4$		1.1 1)	6.7 (1.5) 1)		2.0 7)	FER 77	QTL 71	0.55(5)	1)
RDP	RbH_2PO_4	0.22-1.4	1.04(20)	1.1 (1)	KAT 75			SIN 71, QTL 71a	1.3 (3)	NIK 77
RDA	RbH_2AsO_4	0.26-1.46	0.64	0.93	ADH 74			ADH 69, QTL 71	6)	ADH 69
D-RDA	RbD_2AsO_4							ADH 69	6)	ADH 69
CDA	CsH_2AsO_4	0.26-1.43	0.53 2)	0.80(2)	KAT 74			KAT 74, ADH 69a, QTL 71		
D-CDA	CsD_2AsO_4	0.27-1.66	0.50 2)	0.78(2)	KAT 74			KAT 74, ADH 69a	0.9	ADH 74

Notes: 1) value measured by the author.
2) according to ADH 74.
3) according to NIK 77.
4) relative to KDP and according to ZER 73.
5) typical values in the visible.
6) dispersion given in reference.
7) probably the value of KDP is used.

Table 3.1 Characteristics of frequency doubling crystals of symmetry class $\bar{4}2m$ transparent in the UV.

practise, however, produces only a slight difference due to the small value of ρ (typically in the order of 1°). To obtain a maximum d_{eff} in a noncritical phase-matching arrangement ($\theta=90°$) at normal incidence, Eq. (3-7) shows, that the laboratory crystal is to be cut such that the entrance face is parallel to the optic axis (then $\theta=\theta_m=90°$ and $\rho=0$), whereas its normal is directed at an angle of 45° with both the crystallographic X and Y axes ($\phi=45°$), as is evident from the required direction of $\vec{k}(\omega)$ in Fig. 3.3. The crystals used in the present investigation are cut according to this prescription.

The type I phase-matching proces has been studied theoretically by several authors (KLE 62, KLE 66, BOY 65, BJO 66, ARM 62). Boyd et al (BOY 68) presented a powerful theory, including effects of double refraction, absorption, focusing and phase mismatch for the case of a fundamental beam of TEM_{oo} transverse mode structure, which has a Gaussian distribution of electric field strength over the beam profile (KOG 71). Assuming no depletion of the fundamental beam energy by the SHG proces and a negligible thermal influence of crystal absorptions, Boyd et al derive the following expression for the second harmonic power efficiency γ:

$$\gamma = \frac{P(2\omega)}{P(\omega)^2} = \frac{2}{\pi\varepsilon_o} \frac{\omega^2 d_{eff} kL \exp(-\alpha L)}{c^3 n_{ext}(2\omega,\theta_m) n_o^2(\omega)} h(\sigma,B,\xi) \qquad (3-8)$$

where $P(\omega)$ and $P(2\omega)$ represents power at the fundamental and second harmonic frequencies, respectively; k is the magnitude of the wave vector inside the crystal at the fundamental frequency, L is the crystal length and α gives the combined power absorption by the crystal of the fundamental and second harmonic beams and is given by $\alpha = \alpha(\omega) + \frac{1}{2}\alpha(2\omega)$; all quantities are given in SI units. The influence of focusing, double refraction and phase matching is incorporated in the function h via the parameters σ, B and ξ given by the relations:

$$\sigma = \tfrac{1}{2}b\Delta k$$
$$B = \tfrac{1}{2}\rho\sqrt{(kL)} \qquad (3\text{-}9)$$
$$\xi = L/b$$

where b represents the confocal parameter of the focused fundamental beam having a Gaussian geometry (see Appendix 2). Optimization of $h(\sigma,B,\xi)$ with respect to phase matching σ delivers the function $h_m(B,\xi) = h(\sigma_{opt},B,\xi)$ with σ_{opt}=0.57 (BOY 68). Plots of $h_m(B,\xi)$ are given by Boyd et al. Their results show that optimum conversion efficiency is obtained at ξ=2.84 in a noncritical phase-matching setup (B=0), yielding for h_m the value 1.068. Substitution of typical values for the various parameters (L=3 cm, α=0, $n_{ext}(2\omega,\theta_m)=n_o(\omega)\approx 1.6$, $\omega=3.1\times 10^{15}$, $d_{eff}(ADA)=5.2\times 10^{-13}$ m/V, h_m=1.068) into expression (3-8) yields in this optimum situation $\gamma=9\times 10^{-4}$ W^{-1}. This value agrees roughly with our measured value of 5.5×10^{-4} W^{-1} under slightly less ideal circumstances ($h_m\approx 0.75$, when using a f=5 cm lens for focusing).

The focal length f of a lens used to focus the beam into the crystal is inversely proportional to $\xi^{1/2}$ as is evident from (3-9) and the relation (A2-7) given in Appendix 2. The plots of h_m provided by Boyd et al show, that a reduction of γ by 50% is obtained from a change in ξ by approximately a factor of four with respect to the optimum value of 2.84, which corresponds to a variation in f by a factor of two. The accuracy of the value of f is therefore not critical. Neither is the position of the focus: at the crystal surfaces the reduction is 47% relative to the maximum value of γ, which occurs in the center of the crystal.

Under conditions of optimum focusing (ξ=2.84), negligible double refraction (a noncritical phase matching set-up) and nearly optimum phase matching ($\sigma\approx\sigma_{opt}$) the relative change ε in the conversion efficiency, defined by $\varepsilon(\sigma) = -1 + \gamma(\sigma)/\gamma(\sigma_{opt})$, is approximated by the relation:

$$|\varepsilon(\sigma)| = 1.91(\sigma-\sigma_{opt})^2 \qquad (3\text{-}10)$$

if only terms up to second order in Taylors expansion of $h(\sigma,B,\xi)$

are retained. The results of Boyd _et al_ show (3-10) to be valid even at $\varepsilon \approx 0.5$. Using the definition of σ, given in Eq. (3-9), the permissible deviation, as a function of ε, from the optimum crystal temperature T_{opt} is determined:

$$|T-T_{opt}| = 0.33 \frac{\lambda_o}{L} \sqrt{\varepsilon} \left| \left(\frac{dn_o}{dT} \right)_{\lambda_o} - \left(\frac{dn_e}{dT} \right)_{\frac{1}{2}\lambda_o} \right|^{-1} \qquad (3\text{-}11)$$

where λ_o represents the wavelength in vacuo of the phase-matched fundamental radiation. In case of a 3 cm long ADA crystal, phase matched at 616 nm, a thermal bandwidth of 0.03 C is obtained for a 50% reduction of efficiency. To obtain this stability a double oven system, surrounding the crystal is required.

The permissible frequency deviation from the optimum value ν_o, at a given temperature, is derived similarly:

$$\left|\frac{\Delta\nu}{\nu_o}\right| = 0.33 \frac{\sqrt{\varepsilon}}{L} \left| \left(\frac{dn_o}{d\lambda} \right)_{\lambda_o} - \tfrac{1}{2}\left(\frac{dn_e}{d\lambda} \right)_{\frac{1}{2}\lambda_o} \right|^{-1} \qquad (3\text{-}12)$$

In case of a 3 cm long ADA crystal, phase matched at 616 nm, we measured a value of $\Delta\nu=25(5)$ GHz for $\varepsilon=0.5$, from which, using Eq. (3-4,3-12) and Fig. 3.2, the temperature coefficient of birefringence is calculated yielding the value $6.7(1.5)\times10^{-5}\ K^{-1}$, which is shown in Table 3.1. This result does not agree with the value of $4\times10^{-5}\ K^{-1}$ used by Ferguson and Dunn (FER 77), who probably have applied the known coefficient of ADP because of lack of data for ADA. The measured value of 25 GHz for the frequency tolerance $\Delta\nu$ is not restrictive in the experiment, because no frequency scans larger than 10 GHz are made, which removes the necessity to vary the crystal temperature during scanning.

Effects of crystal absorption, resulting in a local heating and consequently in a thermally induced phase mismatch in the medium, are discussed by Okada and Ieiri (OKA 71a,b). Their results apply only to the situation of weak focusing ($\xi \ll 1$) as is concluded from a comparison between the phase-matching properties of the SHG proces at $\rho=0$ given by Boyd _et al_ (BOY 68) and the expression used by Okada and Ieiri. It is shown in the next section that these thermal effects determine the optimum length of the nonlinear crystal in an intra-cavity frequency doubling set-up. Table 3.1 also shows typical values of the absorption coefficients in the visible region.

Higher order transverse mode structures of the fundamental beam result in a reduced conversion efficiency, when averaged over the beam cross section: for a TEM_{01} mode the reduction is 21 %, whereas a TEM_{02} mode is on the average 49 % less effective (ASH 63). In the dye laser used in our set-up a pure TEM_{00} mode structure is hard to achieve, probably because of inhomogeneities and thermal effects in the dye medium.

In our experiment SHG in a 3 cm long ADA crystal in a non-critical phase-matching set-up at nearly optimum focusing is used to generate the required UV radiation between 307 and 309 nm. The required temperature is then in the range of 100-115 °C, depending on the UV transition to be excited. Experiments performed on D-KDA, which can be 90° phase matched at 60 °C and 616 nm, proved it to be less efficient than ADA and is therefore not used in our situation. Fröhlich et al (FRO 76) report a conversion efficiency for a 3 cm long ADA crystal of 5×10^{-4} W^{-1} in our wavelength range, which agrees with our observations. In extra-cavity experiments the maximum observed UV power was approximately 2.5 μW at 308 nm using a stable single mode fundamental input power of 70 mW. Because the laser output power can hardly be increased beyond this value under stable operating conditions, the UV power requirement, given in Chap. 2, can not be met with this technique. Fröhlich et al (FRO 76), however, obtain several milliwatts of single mode UV radiation by inserting the ADA crystal into the dye laser cavity and taking advantage of substantially higher fundamental power levels inside the cavity. If the insertion loss of a nonlinear crystal into the laser cavity can be kept small with respect to the round-trip loss of the laser cavity without the frequency doubling unit, the amount of UV produced in an intra-cavity SHG set-up is expected to increase significantly with respect to extra-cavity experiments.

3.1.2 INTRA-CAVITY SHG

The fundamental radiation field inside the laser cavity consists of two counter propagating beams, both generating a second harmonic wave inside the doubling crystal. Because the nonlinear polarization is generated by the total electric field at the fundamental frequency, a third contribution to the produced second harmonic field exists due to the interaction of the two counter propagating waves. A straightforward calculation of the induced polarization, using Eq. (3-6) and taking into account the fixed phase relation between the two fundamental beams, shows this contribution to consist of two components: a time independent and a position independent part, both unable to produce an energy flow. The UV radiation produced intra-cavity is, therefore, the sum of two separate contributions arising from the two counter propagating fundamental waves in the way described in the previous section. Confining the attention to the one-way proces, the amount of second harmonic generated can be determined provided the one-way fundamental power is known. The latter in turn depends on the amount of UV produced, because the SHG proces acts as a nonlinear loss mechanism, which has to be added to the round-trip losses of the laser cavity. A general expression for the UV production in an intra-cavity SHG set-up, taking into account the various loss processes, has been given by Fröhlich _et al_ (FRO 76), which in practical situation reduces to:

$$P(2\omega) = \frac{\alpha^2\gamma}{\ell^2} (P_p - P_{th})^2 \qquad (3\text{-}13)$$

Herein $P(2\omega)$ is the one-way generated UV power, P_p represents the pump power for the dye medium, whereas P_{th} is the threshold pump power for laser action. The quantity ℓ represents the round-trip losses of the laser cavity excluding the SHG loss, and α contains various dye and cavity parameters; α can be determined from measurements of P_{th} and the fundamental laser power in the way described by Fröhlich _et al_. Inspection of Eq. (3-13) learns, that the round-trip loss ℓ of the dye laser cavity should be kept to an absolute minimum to obtain high second harmonic powers: $P(2\omega)$ depends stronger on ℓ than via ℓ^{-2} due to the linear dependence of P_{th} on the round-trip loss. Inserting typical values for a Rhodamine B dye laser with an intra-cavity nonlinear crystal (α=0.2, γ=5x10^{-4} W^{-1}, ℓ=0.2, P_{th}=1.5 W, P_p=4 W) yields 3 mW for the one-way generated UV power, which is roughly a factor of three higher than observed.

Effects of crystal absorption at the fundamental frequency, resulting in increased losses and a thermal phase mismatch in the crystal, determine the optimum crystal length. Ferguson and Dunn (FER 77) studied the influence of these effects on the amount of second harmonic produced in an ADA crystal placed inside the cavity of a Rhodamine 6G dye laser and provide curves to determine the optimal length for various values of crystal absorption and round-trip loss. The measured absorption coefficient of the various ADA crystals used in our set-up varied between 0.005 cm^{-1} and 0.006 cm^{-1}, which then gives an optimum length of 3 cm at 4 W pump power and 20 % round-trip loss, if the parameters applicable to a Rhodamine B dye medium do not differ much from their Rhodamine 6G equivalents. The dependence of the second harmonic power on crystal length, taking into account both absorption and phase-mismatch effects, is weak at the present values of the fundamental power. We repeated the calculations of these absorptive effects using a temperature coefficient of birefringence equal to 6.7x10^{-5} K^{-1}, instead of the value 4x10^{-5} K^{-1} used by Ferguson and Dunn, and obtained approximately the same result: a very flat optimum at a crystal length of 2 cm. With help of the result of Okada and Ieiri (OKA 71a) we have calculated the reduction of the SHG conversion efficiency due to the crystal absorption and obtained a value of about 20 % for the total two-way fundamental intra-cavity power of 2 W, applicable to the situation in our laser system. Deviations from the values given above may occur in the actual situation, where optimum focusing is employed in the SHG proces, because the result of Okada and Ieiri is apparently derived under the assumption of weak focusing. These and other problems, such as thermal defocusing effects on the fundamental beam, make a good estimate of the amount of second harmonic, produced in an intra-cavity SHG set-up, more complicated.

Assuming a realistic conversion efficiency of $5\times10^{-4}\ W^{-1}$ (FRO 76) the round-trip loss induced by the energy conversion is at most in the order of 1% for fundamental power levels of several Watts, if thermal effects are neglected. Compared to the 20% round-trip loss of the cavity set-up this contribution is negligible and and depletion of the fundamental intra-cavity power due to the second harmonic production can be neglected.

3.2 THE FREQUENCY DOUBLED DYE LASER

The UV source consists of a CW dye laser of the standing wave type, with a nonlinear crystal placed inside the cavity to produce the second harmonic. The dye laser is pumped by a high power argon-ion laser (Spectra Physics, model 171-03) at 514.5 nm. The optimum pump power to the dye medium, which consists of a 2×10^{-3} molar solution of Rhodamine B in ethylene glycol, was found to be approximately 4 W. At higher power levels the cavity losses are increased due to thermal lensing effects in the dye medium (WEL 75, TES 76), resulting in a reduction of the dye laser intensity. Attempts to reduce these effects by the use of an aequeous solution of Rhodamine B, as suggested by several authors (LEU 76, FRO 76), including a viscosity raising additive (Mowiol 88, manufactured by Hoechst), were not succesfull, because the higher dye flow speeds required could not be achieved with the present dye circulator.

The dye laser set-up itself is a modified version of the jet stream dye laser system, model 580 A, manufactured by Spectra Physics. The modification consists of an enlargement of the laser cavity in order to provide space for the ADA crystal with surrounding oven system. For this purpose, a new base was constructed, which is much more massive than the original one resulting in a reduced sensitivity to vibrations. In addition, both the argon-ion and dye lasers are placed on a table top, having an internal honeycomb structure to absorb vibrations (NRC, model K-410 A).

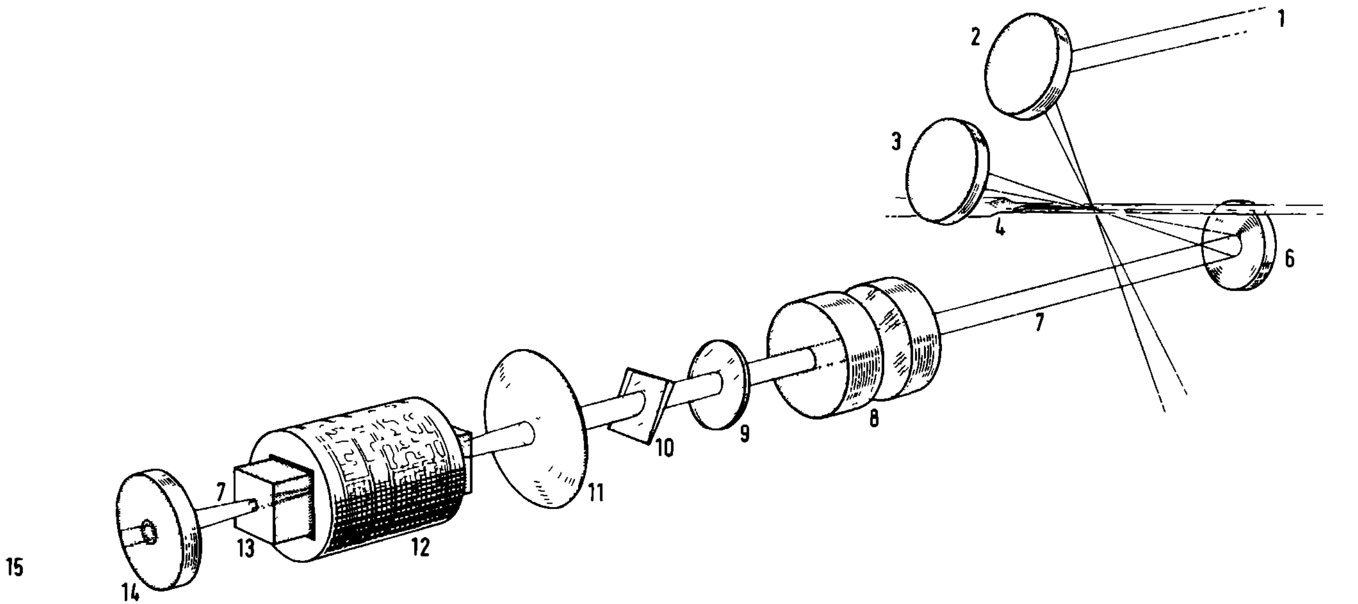

1. pump beam	5. dye jet	9. fine tuning etalon	13. crystal
2. input mirror	6. collimating mirror	10. tuning wedge	14. output mirror
3. end mirror	7. dye laser beam	11. lens	15. UV beam
4. dye nozzle	8. narrow band etalon	12. crystal oven	

Fig. 3.4 A schematic view of the intra-cavity frequency doubled dye laser system.

Drift of the frequency of the dye laser radiation, due to thermal expansion of the laser cavity, is minimized by the application of quartz rods as spacers between the mounting plates of the various mirrors. In principle, also the lens, used to focus the dye laser beam into the nonlinear crystal, should be mounted in this way. However, no problems were encountered when the lens holder was rigidly mounted to the base. A schematic view of the laser system is shown in Fig. 3.4. Several components of this system are discussed below shortly.

The input head (consisting of the dye nozzle, the end mirror and the collimating and input mirrors) is that of the original dye laser system. No modifications are introduced in this section. All mirrors have a radius of curvature equal to 50 mm. The input mirror focuses the pump beam onto the dye jet, which is positioned at Brewster angle relative to the intra-cavity beam of the dye laser to minimize reflection losses at the surfaces of the jet. The cavity itself has a folded structure, the folding angle being chosen such that the astigmatism, introduced by the off-axis incidence of the dye laser beam on the collimating mirror, is compensated by the dye jet (KOG 72).

The tuning wedge, fine-tuning etalon and narrow band etalon are plane-parallel etalons of the Fabry-Perot type and are used for wavelength and longitudinal mode selection. The tuning wedge, placed at Brewster angle, is a low finesse, extremely thin, wedge shaped etalon having a free spectral range (FSR) of approximately 85 THz according to the specifications. The fine-tuning etalon, consisting of a 30% reflective coated glass plate, has a FSR of 900 GHz and a finesse $F \approx 2$, whereas the values for the piezo-electrically tunable narrow band etalon are measured to be FSR~90 GHz and F~12. The latter etalon is actively temperature stabilized to reduce thermal drift of its transmission curve. When superimposed correctly, the transmission characteristics of the three etalons allow only a single longitudinal cavity mode to have enough gain for laser oscillation. This situation is called single mode operation. The distance between adjacent cavity modes is measured to be 314.0(1.3) MHz in the visible, which corresponds to an effective cavity length of 0.477(2) m, when all required components are inserted into the laser cavity, including the frequency doubling unit.

Mainly for constructional reasons, the linear geometry of the frequency doubling set-up was preferred over the folded design as applied in the input section of the dye laser: the latter geometry would require a Brewster angle crystal in an almost 90° folded leg of the cavity. Using the imaging rules, given by Kogelnik et al (KOG 72), the optical combination of lens, crystal and output mirror is equivalent to a fictitious plane mirror located approximately 10 cm in front of the lens. Placing this mirror at the position of the original output mirror to retain optically the original cavity geometry would increase the cavity length by 10 cm, resulting possibly in frequency stabilization problems in single mode operation due to a reduced mode spacing. These problems are reduced by keeping the cavity length as small as possible.

The frequency doubling unit consists of the ADA crystal (Quantum Technology Ltd, Canada; dimensions 10×10×30 mm) and a fused silica lens (Melles Griot, Holland; diameter 25 mm), which focuses the intra-cavity dye laser beam (width 0.5 mm) perpendicularly into the crystal. All surfaces are polished and provided with V-type anti-reflection coatings (Gsänger Optische Instrumente, W.Germany) having a reflectivity $R<0.25\%$. The crystal is placed in a thermally stabilized double oven system. The UV output is extracted from the laser cavity through a specially coated fused silica mirror (Valtec, USA), the transmission of which is shown in Fig. 3.5. The mirror (diameter 7.75 mm, radius of curvature 5 cm) is glued onto a thin aluminum ring, which is rigidly pressed against a piezo-electrical element (Elomag, type MD44, expansion coefficient 4.4 nm/V) by means of an "O"-ring supported by the holder housing for frequency stabilization and scanning. The pressure used is quite high in order to shift the first mechanical resonance of the system to 19 kHz. The combination is placed in an adjustible mount for precise alignment of the mirror. The focus inside the crystal is situated in the center of curva-

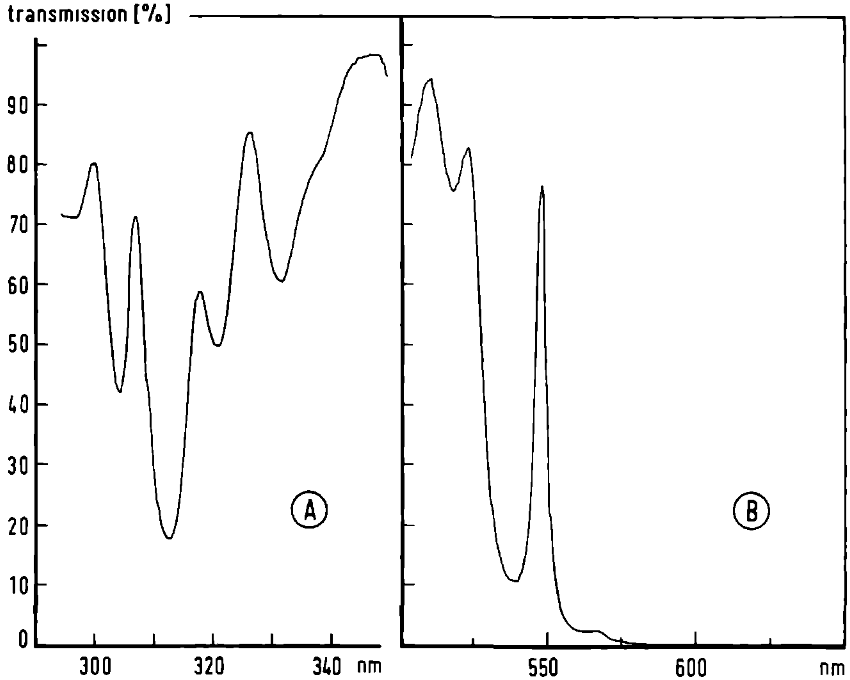

Fig. 3.5 The power transmission of the output mirror in the visible region (B) around the fundamental wavelength as well as in the UV region (A) for the second harmonic radiation.

ture of the output mirror.

The losses introduced by the tuning elements are difficult to measure due to the small values and the strong dependence on tilt angle. With the help of the relation given by Frohlich et al (FRO 76), which shows the threshold pumping power to be linearly dependent on the cavity round-trip losses, the total round-trip loss excluding the crystal was measured to be approximately 18% at 616 nm, whereas insertion of the ADA crystal increases the loss by somewhat more than 2%. The loss introduced by tilting of the narrow band etalon is estimated using the theory developed by Leeb (LEE 75), yielding a value of 20% for a tilt angle of 0.5° used in the present set-up. In view of the difficulties in measuring the losses, this value appears to be in reasonable agreement with the observation that the majority of losses are caused by the narrow band etalon.

To obtain mode-hop free operation of the laser the electronically tunable narrow band etalon is locked to the cavity mode by techniques to be described in the next section. Due to the large spectral width of the associated transmission curves the tuning wedge and fine-tuning etalon need not be locked for stable operation.

The geometry of the frequency doubling unit for optimum SHG is determined from the propagation law for Gaussian beams, as discussed in Appendix 2. The focal length f of the lens, required to obtain optimum focusing ($L/b = 2.84$, where L is the crystal length), is then calculated from Eq. (A2-7). Using appropriate values for the various parameters ($2w = 0.5$ mm, $n_o = 1.575$ at 616 nm, $L = 3$ cm) we obtain $f = 3.29$ cm. The position of the lens is determined by calculating the distance a between its second principle plane and the crystal surface. Because, according to the ray matrix given by Yariv (YAR 75), the radius of curvature R of the wave front of the incident dye laser beam at this plane equals f, when seen from the focus, a is obtained by substitution of $R = f$ and $s = a$ in Eq. (A2-8) delivering $a = 2.30$ cm for a focus centered in the crystal. The spacing d between the output mirror and crystal surface is determined by the requirement, that the laser beam retraces itself upon reflection at the mirror surface, which occurs if $R = R_o$ (the radius of curvature of the output mirror). From Eq. (A2-8) with $s = d$ we then obtain $d = 4.02$ cm for $R_o = 5$ cm. However, as the space between the lens and the crystal is rather small in this case, a lens with $f = 5$ cm was chosen. The values of a, b and d become then: $a = 3.93$ cm, $b = 2.41$ cm and $d = 3.93$ cm. With this value of b the focusing parameter ξ, defined in Sect. 3.1, becomes 1.25, which means a reduction by 18% of the conversion efficiency according to the results of Boyd et al (BOY 68). The lens is mounted in a fine adjustable support for optimization. The longitudinal position is found not to be very critical: a displacement of approximately ± 1 mm can be tolerated

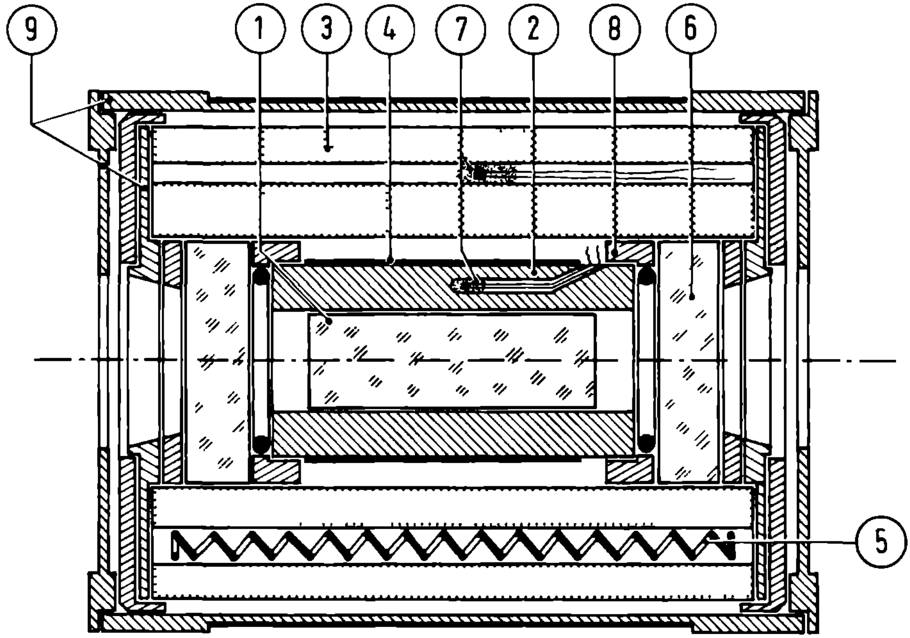

1. crystal
2. inner oven block
3. outer oven block
4. inner oven heater
5. outer oven heater
6. window
7. NTC+heat sink compound
8. teflon spacers
9. metal caps

Fig. 3.6 The double oven system for active stabilization of the crystal temperature. In some experiments the windows are removed.

before any effect is seen on the UV power.

The ADA crystal is placed inside a well stabilized oven system, shown in Fig. 3.6, capable of maintaining a thermal stability better than 0.01 °C at an operating temperature of 110 °C. The stability is needed to keep the power fluctuations due to crystal temperature below 1%. The ADA crystal is sandwiched between two semi-cylinders made of aluminum, constituing the inner oven. To improve thermal contact between oven and crystal one sheet of Al foil and some heat sink compound are inserted in between. The oven temperature is controlled via a feedback loop, consisting of a NTC resistor ($R \sim 10$ kΩ at 25 °C, type YSI 44006) attached to the oven block, regulating electronics and a thermofoil heater (MINCO, model HK-913) glued onto the oven. Because ADA crystals are highly hygroscopic, contamination of the crystal surfaces by water vapour is prohibited by keeping the oven temperature at a level of approximately 50 °C, when the system is not in use. This oven is mounted inside a cylindrically shaped outer oven by means of teflon endcaps (serving as spacers) in order to provide minimal thermal contact between the two oven systems. The outer oven is a commercial type (Model TC, Quantum Technology LTD, Canada), with the original endcaps replaced by caps of own design. The temperature control mechanism is essentially the same as used for the inner oven. The windows shown in Fig. 3.6 were present only during the measurements of the hyperfine splittings, whereas they were removed in the population transfer experiments to reduce the cavity losses. The entire system is mounted via a pyrex tube in an adjustible mount in order to optimize the crystal position

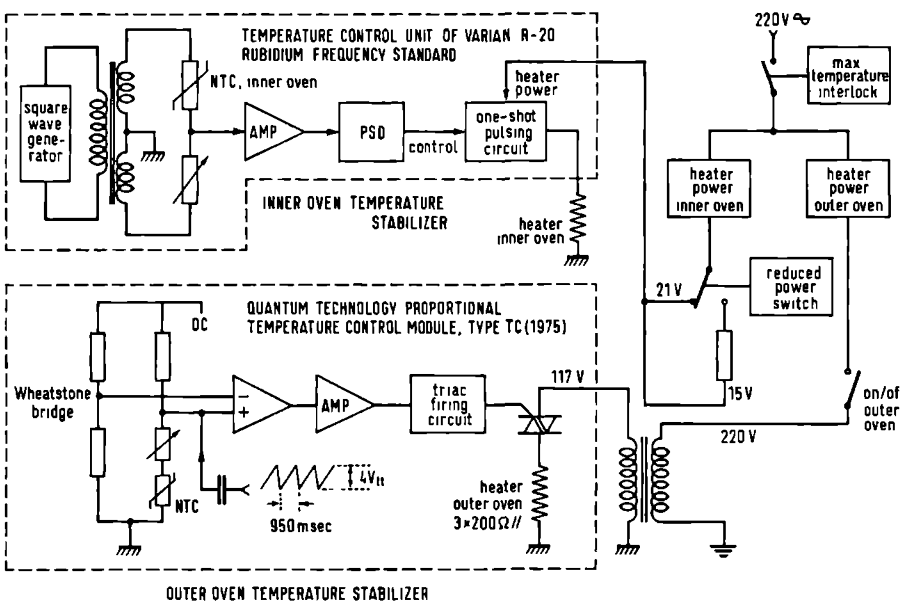

Fig. 3.7 The electronic block diagram for active stabilization of the crystal temperature. Also shown are the various protecting interlocks.

relative to the laser beam. The maximum safe operating temperature of the crystal is approximately 110 °C, as stated by the manufacturer. The regulating electronics of both oven systems are of the proportional type: when the crystal temperature, sensed by the NTC resistor, is below an adjustible limit, the heater is continuously powered; otherwise, the heater power is pulsed with a pulse width proportional to the temperature deviation from the preset value. A block diagram of the electronic circuitry is shown in Fig. 3.7, with the various interlocks designed to protect the crystal from damage. The reduced power facility is used to heat the crystal from the standby temperature to the operating temperature, because the heating rate should not exceed 5 °C/min. in order to prevent the occurrence of a thermal shock; the various other interlocks are used to prevent the temperature from rising too high, the cut-off point was set at 110 °C.

The lifetime of the ADA crystal turned out to be limited mainly by the occurrence of coating defects. Although the temperature used (110 °C) is just at the limit of the range for safe operation, the onset of coating defects, increasing the cavity losses for the fundamental laser radiation, proved to be the restrictive factor rather than deterioration of the crystal as such. The cause for the occurrence of these coating defects has not yet been identified and might be due to the presence of dust particles on the coating, which are burned by absorption of the laser radiation, a chemical reaction between the crystal and coating materials possible at elevated temperatures produced by laser beam absorption or a local heating of the coating, which causes the material to expand or evaporate.

3.3 FREQUENCY STABILIZATION

The expected absorption linewidth of the OH molecules in the beam maser apparatus is in the order of 50 MHz. Accurate measurements are only possible if the frequency stability of the UV source is much better than this figure. Because the drift of the free running dye laser, measured over a period longer than

1 s, is larger than this value, active frequency stabilization has to be applied. The stabilization scheme used in our set-up consists of two loops:

- locking of the frequency of the laser mode to an external reference cavity, which was chosen to be a confocal Fabry-Perot etalon;
- locking of the transmission peak of the narrow band etalon to the lasing cavity mode to prevent mode hopping.

The frequency stability obtained by these techniques is determined by the residual thermal drift of the reference cavity and the electronic circuitry. Further refinement proved not to be necessary

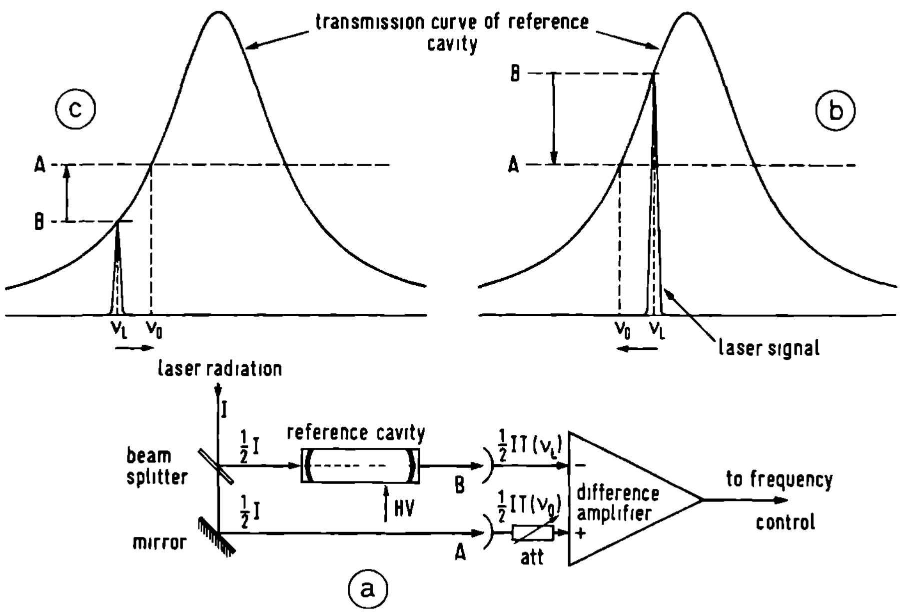

Fig. 3.8 The principle of frequency stabilization. The electronic circuit (a) is schematically indicated. The directions of the difference voltage (↑↓) and of the resulting frequency corrections (⇄) are shown for the cases $\nu_L > \nu_o$ (b) and $\nu_L < \nu_o$ (c), assuming a positive difference signal to correspond to a positive frequency correction.

during the experiments. If desired, improved stability is possible by locking the laser frequency, pre-stabilized by the present technique, to an atomic or molecular transition using a low frequency modulation of the reference cavity to produce an error signal for phase-sensitive detection.

3.3.1 CAVITY MODE STABILIZATION

The frequency of the cavity mode is locked to an adjustible position on the side of the transmission curve of a reference cavity using an intensity difference technique as shown in Fig. 3.8. The fundamental laser beam of intensity I, indicated in Fig. 3.8a and derived from the radiation reflected off the tuning wedge, is split into two beams of equal intensity; one of them traverses the reference cavity (Tropel, model 240-B) and is monitored by a build-in photo-diode delivering an output signal proportional to $\frac{1}{2}IT(\nu_L)$, with $T(\nu_L)$ the transmission of the reference cavity at the laser frequency ν_L. The other beam impinges directly on a photo-diode (EG&G, model HAV 1000A) with an adjustable gain producing an output signal corresponding to $\frac{1}{2}IT(\nu_o)$ with ν_o the desired locking frequency. Usually ν_o is chosen such that $T(\nu_o) \simeq \frac{1}{2}T_{max}$ with T_{max} the maximum transmission of the reference cavity. The output voltage of the difference amplifier is then given by the relation:

$$V_{out} \div \tfrac{1}{2}[T(\nu_o) - T(\nu_L)]I \qquad (3\text{-}14)$$

which is valid if the laser linewidth, at a time scale in the millisecond range, is much smaller than the instrumental bandwidth of the reference cavity, which applies in our situation. When $\nu_L > \nu_o$, as in the situation shown in Fig. 3.8b, the output signal of the difference amplifier is negative, if ν_o is situated on the low frequency side of the transmission curve. When $\nu_L < \nu_o$ the situation shown in Fig. 3.8c is obtained and the output voltage is reversed. The output signal, by which it is thus possible to discriminate between a positive and a negative frequency offset from ν_o, is then used to correct the laser frequency by driving the HV amplifier controlling the cavity length. In this scheme the feedback loop can be made quite fast, the response being limited by the correcting elements in the laser cavity.

Scanning of the dye laser frequency is accomplished by sweeping the reference cavity by means of its piezo-electric tuning mechanism. The laser frequency will automatically follow due to the feedback action. The scan range is limited, at the moment, by the maximum voltage tuning of the HV amplifier to 3.3 GHz in the visible, corresponding to a change of the length of the laser cavity by 3.1 μm. However, by utilizing the full expansion capability of the MD44 piezo (8.8 μm), a scan range of 9.2 GHz should be obtainable. This is not attempted in our set-up, because a fast programmable ($\tau<10^{-3}$ s) HV amplifier, capable of a 2 kV voltage swing and being rather noise free, was not available.

The spectrum analyzer serving as the reference cavity has a FSR = 7.5 GHz and an instrumental bandwidth of 37.5 MHz, which is increased to 100 MHz by a slight misalignment of the analyzer body at the expense of signal transmission. This was necessary in order to reduce the probability that the system drops out of stabilization, when small sudden disturbances cause the laser frequency to jump over the top of the transmission curve. The analyzer (body made of invar) is placed inside a vacuum tank and is actively temperature stabilized in order to eliminate thermal drift. The residual temperature fluctuation is less than 0.01 °C at 35 °C. The drift of the reference frequency ν_o is determined by the residual thermal drift and by the pressure change in the interior of the analyzer housing. With the help of the expression for the refractive index of air as a function of temperature T and pressure P (LAN 62), the following relation is deduced for the change in ν_o at $\lambda = 616$ nm and $T = 300$ K:

$$\frac{\Delta\nu_o}{\nu_o} = \left(9\mathrm{x}10^{-12}\ P - \frac{1}{L}\frac{dL}{dT}\right)\Delta T - 2.6\mathrm{x}10^{-9}\ \Delta P \qquad (3\text{-}15)$$

Herein P is measured in Pa and L represents the separation of the analyzer mirrors, which in our case is 1 cm. The coefficient of expansion (the last term within the brackets) depends strongly on the construction of the mirror mounts. Because no data of this quantity are available, we assume the coefficient of invar, equal to $1.44 \times 10^{-6}\ K^{-1}$, to be applicable. Using the temperature fluctuation of 0.01 °C given above, it is then concluded, that the observed drift of $\leq$100 MHz/hour in the UV is mainly due to a pressure change of approximately 33 Pa/hour in the analyzer, if the set is operated far below atmospheric pressure as in our case.

A schematic diagram of the electronic stabilization circuitry is shown in Fig. 3.9. The difference amplifier is a very critical element in the feedback circuit and requires the use of a very low drift operational amplifier like LM 725. If the frequency ν_L of the radiation from the free running dye laser deviates from the desired frequency ν_o, as in the situation depicted in Fig. 3.8b-c, restoration of ν_L to ν_o requires a permanent nonzero correction voltage. This, however, is only possible if integrating action is incorporated in the feedback loop, because the output voltage of the difference amplifier vanishes at $\nu_L=\nu_o$. These deviations from the desired frequency occur, for instance, when the transmission curve of the reference cavity is shifted, as occurs in scanning, or when the optical length of the laser cavity drifts. Therefore a PI regulator is used in the feedback loop to provide an Integrated ($\tau \approx 22$ ms) and a Parallel signal, which is an amplified version of the difference signal and is incorporated, because the integrator response vanishes at high frequencies permitting no correction for perturbations in this frequency regime in case only the integrator is present. A 6 dB per octave roll-off is incorporated with a 3 dB down frequency of 2 kHz in order to avoid triggering of the 19 kHz resonance of the output coupler. The parallel gain is adjusted for maximum stability. Using this system succesfull frequency stabilization is obtained, provided the narrow band etalon is locked to the cavity mode as described next.

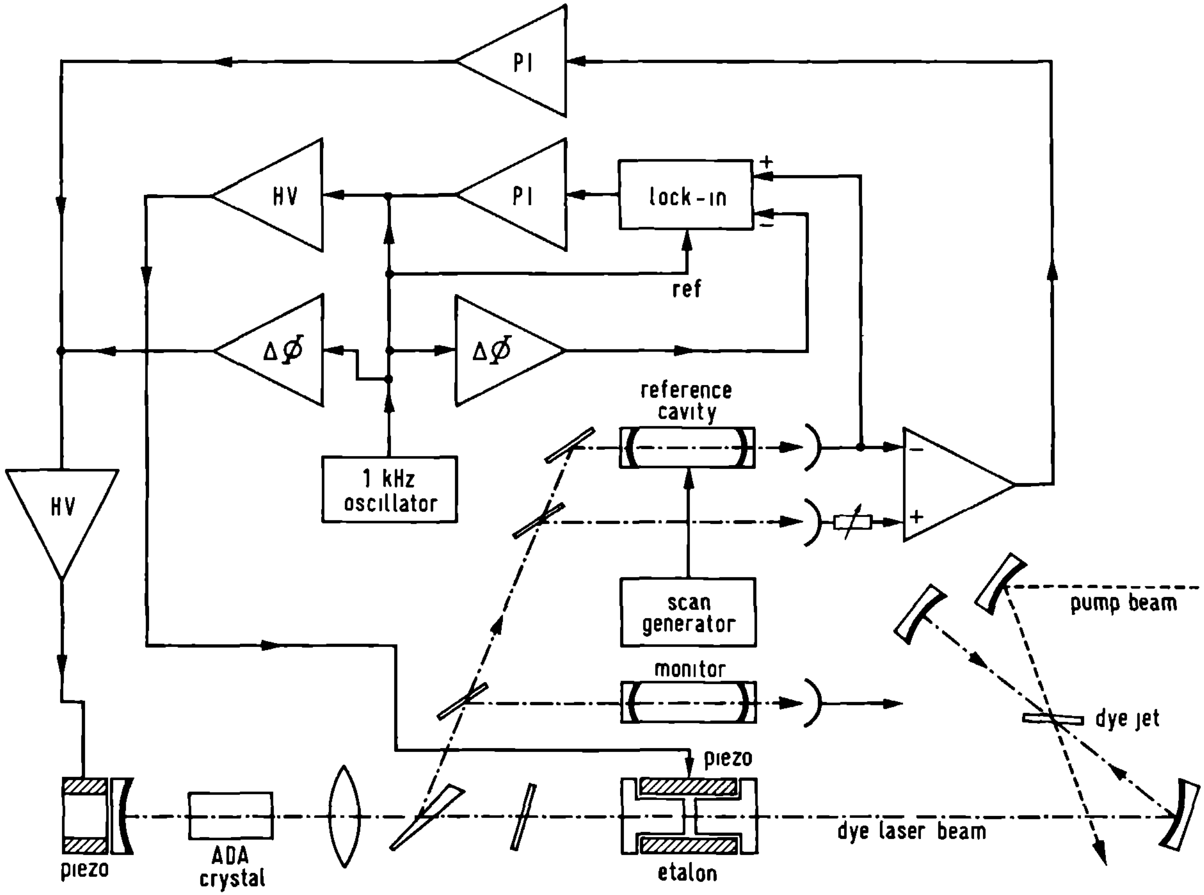

Fig. 3.9 The frequency stabilization block diagram. The narrow band etalon stabilization is also shown. The elements indicated by ΔΦ are phase-shifting amplifiers.

3.3.2 ETALON STABILIZATION

Stabilization of the center frequency of the transmission function of the etalon is accomplished by a phase-sensitive technique. Modulation of this center frequency at a rate of 1 kHz causes an intensity modulation of the laser radiation, the amplitude of which is minimum, if the frequency of the lasing cavity mode coincides with the mean position of the center frequency of the etalon transmission curve. If this is not the case, the phase of the intensity modulation, measured by a phase-sensitive detector, determines whether the frequency of the cavity mode is located above or below the etalon center frequency. The output of the PSD drives, via a PI regulator of the same type as used in cavity stabilization, the HV amplifier to control the etalon mirror spacing by a piezo-electric tuning element. A modulation depth of 10% is used, which corresponds to a 100 MHz peak-to-peak frequency swing of the transmission maximum. Demodulation of the error signal is performed by a differential lock-in amplifier (PAR, model 128A) using a time constant of 10^{-2} s. The feedback circuit should be very noise and drift free because of the very large input sensitivity of the etalon HV amplifier (52 GHz/V in contrast to 0.9 GHz/V for the cavity amplifier), which means that all noise and drift effects should be well below 1 mV in order not to disturb the stabilization proces. Due to the feedback action, however, the circuit will counteract rendering practical situations slightly less critical. Experiment indicates, that only large sudden disturbances of the laser intensity, having durations in the order of 10^{-4}-10^{-3} s, drive the system out of lock, e.g. bunches of air bubbles in the dye stream. The very fast ones, however, are cut off by the low pass output filter of the lock-in amplifier. In certain situations it proved to be necessary to increase the time constant to 0.1 s. Etalon resonances were observed near 6 kHz, but did not cause problems thanks to the rather large time constant of the PSD.

Since the amplitude of the modulated signal depends on the slope of the etalon transmission curve as well as on the mean laser intensity, a small rising adjacent cavity mode can very well produce a contribution to the intensity modulation, which dominates the contribution from the primary mode. As a result the etalon will be pulled away from the primary mode resulting in unstable operation. This is prevented by deriving the error signal from the output of the reference cavity, where only the primary mode is monitored. A problem is presented by an unwanted frequency modulation of the laser radiation generated by the modulation of the transmission curve of the narrow band etalon. This effect is due to a change of phase of the signal transmitted by the etalon, when the lasing cavity mode is not exactly centered in the etalon transmission curve, causing an additional interfering amplitude modulation at the output of the reference cavity and a shift of the locked position of the etalon transmission maximum. The magnitude of the induced frequency modulation was measured to be 2-3 MHz and produced at the output of the reference cavity an amplitude modulation comparable to the intensity modulation discussed above. This effect can only be reduced by a counter modulation of the cavity length and thereby of the laser frequency. To accomplish this a 1 kHz signal of appropriate phase is injected into the cavity HV amplifier by an active phase shifter. A second phase-shifted signal is injected into the inverting input of the differential lock-in amplifier to shift the etalon transmission curve slightly relative to the cavity mode, which turns out to improve stability. A tentative explanation for this phenomenon will be discussed in the next section.

When the feedback loop is closed and the PI regulator switched on, the 1 kHz amplitude modulation, observed at the reference cavity output, vanishes totally. The phase-shifted signal to the PSD is now adjusted until the modulation is just visible again.

When both the cavity and narrow band etalon are stabilized by the method described above, locking periods in the order of 1 hour for stabilization at a fixed frequency are obtained showing the good operation of this method, whereas stabilized scanning of the fundamental frequency, by sweeping the reference cavity, is obtained over a range of 3.3 GHz.

3.4 RESULTS AND DISCUSSION

The operating characteristics of the intra-cavity frequency doubled dye laser can be summarized as follows:

- operating wavelength: approx. 305-309 nm, mainly limited by the transmission of the output coupler, the maximum operating temperature of the crystal and to a lesser extent by the various anti-reflection coatings.
- dye medium : 2×10^{-3} molar solution of Rhodamine B in ethylene glycol.
- single mode UV power: non-scannable: 0.3 mW at 308 nm.
  scannable: 60 μW at 308 nm, determined by the narrow band etalon tilt angle.
  nonlinear crystal: ADA, dimensions 10x10x30 mm.
  pumping power: 4 W at 514.5 nm.
- UV power stability : non-scanning: ± 10% on time scale >1 s, mainly due to fundamental power fluctuations; <± 10% on time scale <1 s.
  scanning: ± 50%, probably due to an interference effect (see below).
- mode spacing in UV : 628.0(2.6) MHz.
- UV frequency stability : $\leq$ 100 MHz/hour, determined by the drift of the reference cavity.
  FM jitter: 2-3 MHz on time scale <1 s at 616 nm.
- stabilized scan range : 6.6 GHz at 308 nm, limited by the HV amplifier output voltage swing.
- output beam geometry: divergent.

The 6.6 GHz scan is only possible at the specified lower power level of 60 μW due to the required larger tilt angle of the narrow band etalon. This may be caused by the need for a stronger mode competition (the tendency for the gain of the strongest mode to grow at the expense of the gain of nearby modes) to prevent the detrimental influence of two phenomena observed:

a. pronounced asymmetry in the maximum mode-hop free scan distance of the narrow band etalon, when sweeping it up and down over the lasing cavity mode.

b. a strong tendency for mode-hopping after scanning of the laser frequency over small distances, typically between 200 and 400 MHz, despite locking of the etalon to the cavity mode. Concurrently, the laser intensity shows a periodic variation, with mode-hops occurring most frequently at the minimum intensity situations.

The existence of an additional interference pattern in the laser cavity is a possible explanation for these phenomena. Such patterns are generated by reflecting surfaces in the laser cavity, e.g. the surfaces of the narrow band etalon, the lens or the crystal. Reflection at one of the mirror surfaces of the etalon, positioned approximately in the center of the dye laser cavity, is expected to be the main cause of trouble, because removal of the lens and crystal oven assembly does not lift the observed effects. Figure 3.10 shows a schematic picture of the effect of interference on the laser operation. In single mode operation the transmission function of the narrow band etalon allows only the central cavity mode I at frequency ν_o to lase, if the loss due to the interference pattern III is neglected. If not this pattern, resulting for example from the interference between waves reflected at one of the etalon mirrors and the laser end mirror, introduces an additional loss difference δ between the central cavity mode and the next higher mode situated at $\nu_o + \Delta\nu$. In this example we consider the situation, where the FSR of pattern III is somewhat larger than $2\Delta\nu$. If at $\nu_o + \Delta\nu$ the transmission reduction Δ, relative to the value at ν_o and due to the etalon curve, is larger than δ, the total loss at $\nu_o + \Delta\nu$ exceeds the loss at ν_o and lasing still occurs at the central cavity mode. When only the etalon

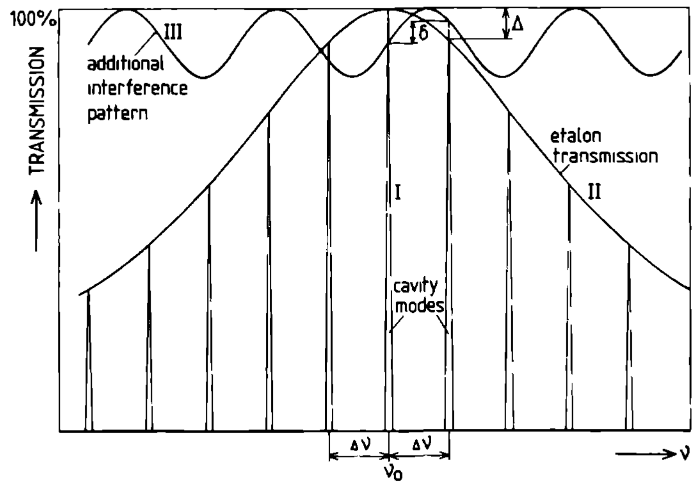

Fig. 3.10 A schematic view of the interference structure in the dye laser cavity as a function of frequency. The additional interference pattern III may be produced by the interaction of waves reflected from the laser end mirror and from one of the mirrors of the narrow band etalon.

transmission curve is moved to higher frequencies, the value of Δ decreases, whereas δ remains constant. A hop to the neighbouring mode at $\nu_0 + \Delta\nu$ then occurs at the moment when $\Delta = \delta$, which in the situation shown happens already, when the etalon center frequency is slightly offset from ν_0. When the etalon transmission curve is moved to lower frequencies, however, the loss increase at $\nu_0 - \Delta\nu$ due to the additional interference III has to be cancelled by the increased transmission of the etalon and therefore a mode hop to $\nu_0 - \Delta\nu$ takes place at a much larger frequency offset from ν_0. This asymmetry in the maximum mode-hopping free scan distance of the etalon is absent, when the central cavity mode I lies in a maximum or minimum of the pattern III. In case the FSR of this pattern is smaller than $2\Delta\nu$ an analogous argument is used to demonstrate the existence of the asymmetry. If the FSR of the additional interference pattern equals $2\Delta\nu$ the asymmetry vanishes, because the losses introduced by this pattern at $\nu_o + \Delta\nu$ and $\nu_o - \Delta\nu$ are equal. Furthermore, when the cavity mode I is scanned synchronously with the center of the etalon transmission function, the value of Δ remains constant and a periodic variation of the total loss (and therefore of the laser intensity) occurs due to the variation of δ during the scan (the interference pattern III is assumed to be fixed). Moreover, if the amplitude of pattern III is comparable or larger than the maximum value of $\Delta/2$, which occurs when the etalon is centered at ν_o, a strong tendency for mode hopping exists when the adjacent cavity mode at $\nu_o + \Delta\nu$ or $\nu_o - \Delta\nu$ is located near a maximum of this pattern. The additional interference theory is thus able to explain the phenomena observed. All these effects are lifted, if the amplitude of this interference pattern is made considerably smaller than the maximum value of Δ. This is achieved by a tilt of the etalon relative to the laser beam, because the amplitude of the pattern III depends strongly on the alignment of the resonator formed by the additional reflecting surface and the laser end mirror. Experimental verification shows this conclusion to be justified, at the expense, however, of the laser intensity, because the walk-off losses induced by the etalon increase with tilt.

CHAPTER 4

THE OH BEAM MASER AND UV EXCITATION

4.1 OUTLINE OF THE MASER SET-UP

Apart from some alterations in the OH source and the modifications necessary to perform the UV excitation experiments, the beam maser is identical to the set-up described by ter Meulen (MEU 76). Figure 4.1 shows schematically the situation during the measurements of the hyperfine splittings of the $A^2\Sigma^+_{1/2}$ state of OH. The OH radicals are produced by the reaction $H + NO_2 \rightarrow OH + NO$ in a gas flow tube of the same type as used by Meerts (MEE 75). The atomic hydrogen is obtained from a microwave discharge in H_2O and the hydroxyl beam is formed by a teflon coated skimmer (ø 3mm). After passing through a buffer chamber, the molecules enter the UV excitation chamber, which is pumped by a 1000 l/s oil diffusion pump equipped with a liquid nitrogen baffle to reduce the deposit of thin oil films on the UV optics. The last chamber contains the electrostatic state selector and the two microwave cavities. The total flow of OH radicals from the beam source may be somewhat higher than the value calculated by ter Meulen (10^{16} s^{-1}), because a sharp edged skimmer is used to minimize collisional destruction of hydroxyl in front of the beam source opening. A mechanical beam chopper provides the possibility to use phase-sensitive detection at 120 Hz. An adjustable diaphragm (diameter 3-10 mm) is mounted at the entrance of the excitation chamber to control the divergence of the molecular beam inside the interaction region.

The state selection required to obtain strong emission signals in the microwave cavities is described in Sect. 4.3. The detection of the UV induced population transfer effects takes place on two microwave transitions simultaneously. The splitting of the levels involved due to the earth's magnetic field is decreased to a negligible amount by magnetic shielding of the microwave cavities. Fine tuning of the resonance frequency is accomplished thermally by a water jacket around the cavity.

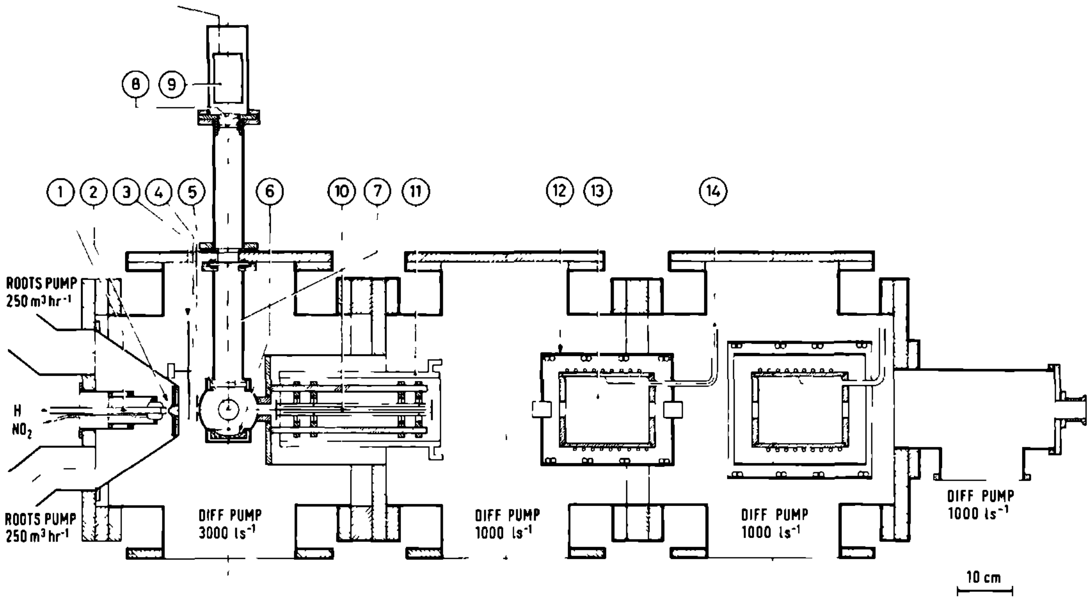

1. OH production tube
2. skimmer
3. beam chopper
4. diaphragm ø 3-10 mm
5. UV beam through window
6. spherical mirror
7. window
8. lens + UG-5 filter
9. photo multiplier tube
10. state selector
11. liquid nitrogen trap
12. mu - metal box
13. microwave cavity + water tube
14. coaxial line

Fig. 4.1 The OH beam maser. The radiation chamber is shown in the geometry used during the measurements of the hyperfine splittings. The direction of the UV beam is perpendicular to the plane of the figure.

During the hyperfine measurements the microwave detection is merely used to monitor the OH beam intensity, while the fluorescence caused by the UV excitation is measured by a photo-multiplier tube (EMI, type 9789QA). In the population transfer experiments the UV excitation is controlled by monitoring the photo-multiplier signal whereas the UV induced population transfer effects on two rotational levels of the electronic ground state are measured by microwave detection.

4.2 THE UV TRANSPORTATION SYSTEM AND EXCITATION REGION

In order to avoid disturbing effects due to vibrations of the vacuum pumps of the beam maser the UV source is placed in a separate room. The UV radiation is transferred to the beam maser (distance $\sim$15 m) via a set of five highly reflecting UV mirrors ($R > 96\%$). The overall loss of the UV intensity caused by this beam transportation system, including a beam collimator consisting of two quartz lenses, is in the order of 50%. The discrepancy with the expected value of $\sim$25% may be due to excessive diffraction, scattering or reflection losses at the separate mirrors, possibly enhanced by collected dust.

The excitation region used in the measurements of the hyperfine splittings in the $A^2\Sigma^+_{1/2}$ electronic state of OH is shown in Fig. 4.1. The UV beam, oriented perpendicularly to the plane of Fig. 4.1, enters the beam maser via a fused silica window, crosses the molecular beam perpendicularly and is reflected by the front surface of a UV sensitive photo-diode (EG&G, type HUV-4000 B, having an integrated preamplifier) into a Wood's horn to minimize scattering of UV radiation into the photo-multiplier. The photo-diode monitors the UV intensity in the beam maser. The width of the molecular beam at the interaction region can be varied from 8 to 20 mm with adjustable diaphragm. The center of this region is situated about 3 mm above the focal point of a UV reflecting spherical mirror ($f = 5$ cm, $R \sim 92\%$). As shown by ter Meulen (MEU 77) this results in a total UV capture efficiency of the fluorescence radiation of approximately 0.8%, whereas only a region of $3 \times 3 \times 3$ mm^3 effectively contributes to the photo-multiplier signal. The capture efficiency is increased to $\sim 4\%$ by the application of a fused silica lens, having $f = 5$ cm and an effective diameter of about 40 mm, placed directly in front of the photo-multiplier window. The fluorescence radiation is extracted from the excitation chamber via a quartz window. A tube, mounted between this window and the photo-multiplier, screens the photo-cathode from ambient background radiation. All surfaces are blackened to prevent scattering of UV into the multiplier. Scattered visible background radiation is further blocked by an UG-5 filter (transmission $\sim 80\%$ at 308 nm) placed in front of this lens. The gain of the photo-multiplier tube is approximately 2×10^7 under normal operating conditions (anode voltage 1000 V) and the quantum efficiency of the cathode material is 0.17 at 308 nm. From these values a total detection efficiency at the photo-multiplier output of 2×10^{-14} A per unit emitted photon flux is derived. This output current is measured and amplified by an electrometer (Keithley, model 610C) or fed into a lock-in amplifier (PAR, model 120), set usually at $RC = 1$ s, to improve the signal to noise ratio.

During the experiments on UV induced population transfer effects between rotational states of OH a different set-up for the interaction region is used. The produced effects are enhanced by a multiple passage of the laser beam through the molecular beam, which is accomplished by the application of a reflection system consisting of two plane mirrors (diameter 2 inches) furnished with highly reflective dielectric UV coatings ($R > 96\%$) and placed 25 mm apart. A schematic view of the UV excitation region used in these experiments is shown in Fig. 4.2. The divergence of the molecular beam, detected in the $J = 3/2, F = 2 \rightarrow 2$ and $J = 5/2, F = 3 \rightarrow 3$ microwave cavities without state selection, is 0.9° and 1.2° respectively, corresponding to Doppler linewidths of 37 MHz and 49 MHz. As the intrinsic linewidth due to the finite lifetime

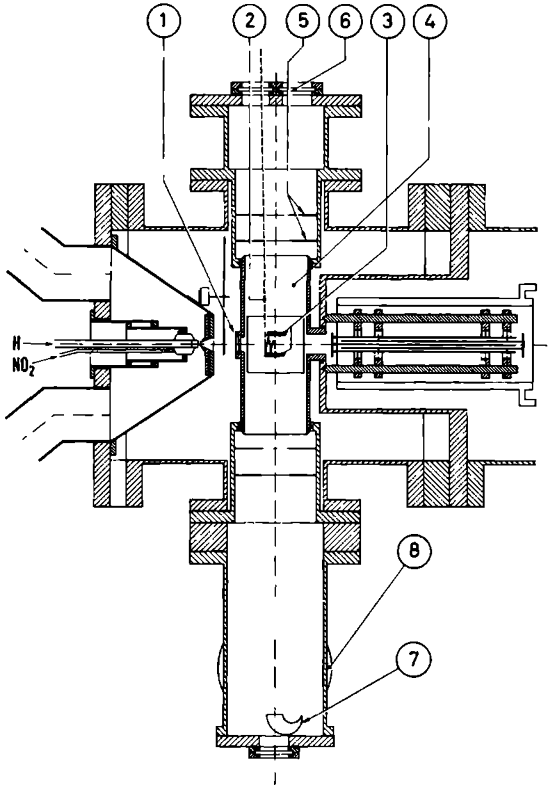

1. diaphragm ∅ 3–10 mm
2. UV beam
3. mirrors
4. radiation chamber
5. diaphragms
6. window
7. Wood's horn
8. diff. pump 1000 l/s + liq. N_2 cooled baffle

Fig. 4.2 The geometry of the radiation chamber during the UV induced population transfer experiments. The remainder of the beam maser is identical to the set-up shown in Fig. 4.1. The path of the UV beam is also indicated.

of the Σ level and the finite time of flight through the interaction region are both in the order of 1 MHz or smaller, the fraction of molecules in the beam excited by the UV radiation is very small (at this time scale the laser linewidth is negligibly small), if a plane-parallel reflection set-up is used. The disadvantage is overcome by changing the angle between the OH and laser beams slightly in each reflection, which is accomplished by a small tilt δ of both mirrors ($4\delta \approx 0.09°$). This technique is especially useful if saturation effects can occur due to the multiple excitation of the molecules in a parallel mirror geometry. The UV beam enters the excitation region at an angle of $\sim 1.0°$ relative to the normal to the molecular beam axis, which produces about 40 reflections before the UV leaves the reflection system (Fig. 4.3). The total length L of the interaction region is then about 4 mm. Due to the small effective absorption linewidth of ~ 1 MHz only the fraction of the OH beam is excited, which is perpendicular to the UV to within 0.02°. If a parallel UV beam is used only disjunct angular portions of the OH beam are then excited. To overcome this problem a 0.4° divergent UV beam focused to a 0.1 mm diameter spot at about the fifth passage through the molecular beam is used. The UV transmitted by the rear mirror is caught by a large Wood's horn to prevent UV scattering into the photo-multiplier. The UV beams transmitted by the front mirror leave the excitation chamber through a quartz window for control of alignment. At a distance of 52 mm above the interaction region a fused silica lens (f = 5 cm)

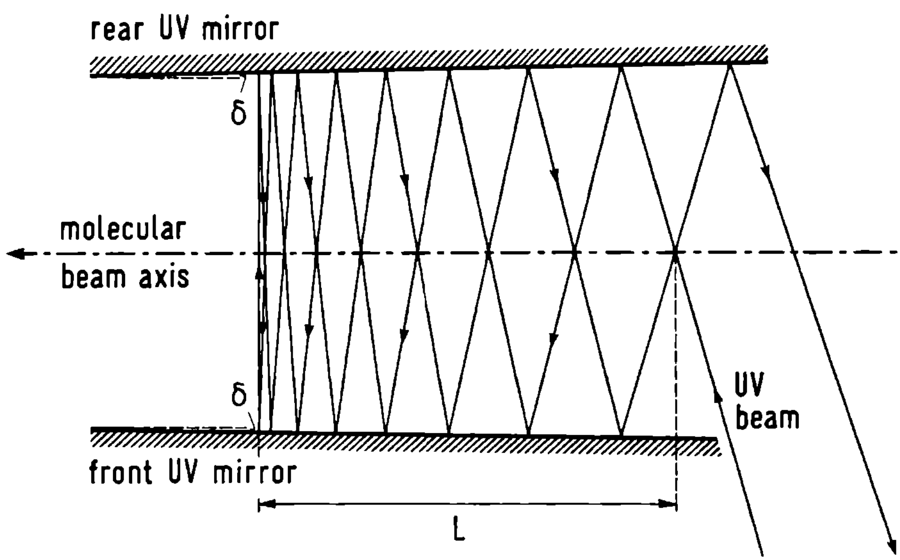

Fig. 4.3 The tilted UV reflection system (not to scale).

is inserted in such a way that, in conjunction with the $f = 5$ cm lens in front of the multiplier, a fluorescence capture efficiency of $\sim$5% is achieved. The background noise due to scattering of UV at the mirror surfaces is reduced to 10^{-7} relative to the incoming UV power by diaphragms between the molecular beam and lens.

4.3 THE STATE SELECTION

State selection of OH is achieved by the application of an inhomogeneous electric field along the path of the molecular beam. The selection of a particular molecular state is then due to the force acting on the molecule when traversing a zone of inhomogeneous electric field according to the relation:

$$\vec{F} = -\frac{\partial W}{\partial E}\vec{\nabla}E \qquad (4\text{-}1)$$

where E represents the scalar magnitude of the electric field strength and W is the Stark energy of the molecular state. For a $|JM_J\rangle$ state W is given by (MEU 76):

$$W = W_o \pm \tfrac{1}{2}[(h\nu_o)^2 + \{\frac{M_J\langle\Omega\rangle\mu}{J(J+1)}E\}^2]^{\frac{1}{2}} \qquad (4\text{-}2)$$

Herein W_o is the average energy of the $|J\rangle$ state, + and − refer to the upper and lower levels, respectively, of a Λ-doublet; ν_o is the frequency of the Λ-doublet splitting (1.666 GHz and 6.033 GHz for the $^2\Pi_{3/2}$, $J = 3/2$ and $J = 5/2$ states, respectively); $\mu = 1.668$ D represents the electric dipole moment of OH (MEE 73). General expressions for $\langle\Omega\rangle$, which is a function of the contributions C_1 and C_2 of the symmetrized Hund's case (a) wavefunctions of the $\Pi_{1/2}$ and $\Pi_{3/2}$ states, respectively, to the wavefunction of the $|^2\Pi^{\pm}_{3/2}JM_J\rangle$ state, are given by ter Meulen (MEU 76); in case of the $^2\Pi_{3/2}$, $J = 3/2$ and $J = 5/2$ states they yield $\langle\Omega(3/2)\rangle = 2.9398$ and $\langle\Omega(5/2)\rangle = 2.8599$.

In our experiments an octupole state selector is used consisting of eight circular rods, diameter 2.5 mm and length 26 cm, arranged in a regular octagon. The odd numbered rods are grounded, the even numbered rods are connected to a high voltage supply (Brandenburg, model 905) delivering voltages up to 50 kV. The inside diameter $2r_o$ of the selector is 10 mm. With this geometry only positive field gradients are obtained, resulting in a collimation of molecules in the upper Λ-doublet state. The molecules in the lower state are bent away from the beam axis and will mostly miss the entrance openings of the microwave cavities. The exact expression for E is rather complicated (VON 58); however, up to a radial distance $r \approx 0.9\, r_o$ it is very well approximated by the cylindrically symmetric expression (neglecting fringing fields):

$$E(r) = 1.69 \frac{r^3}{r_o^4} V \tag{4-3}$$

In this approximation the influence of the selector can be studied by computing the trajectories of molecules in various quantum states (MIE 73). The selector efficiency S for the upper (+) and lower (-) levels of a rotational substate $|JM_J\rangle$ is defined by the relation:

$$S(\pm,J,M_J) = \frac{\Phi(\pm,J,M_J) - \Phi_{\Omega_c}(\pm,J,M_J)}{\Phi_{\Omega_s}(\pm,J,M_J)} \tag{4-4}$$

Herein $\Phi(\pm,J,M_J)$ represents the total flow of molecules in the indicated substate focused by the selector into the entrance opening of the microwave cavity, integrated over the solid angle Ω_s substended by the selector at the source and averaged over the velocity distribution of the molecules, which is assumed to be Maxwellian; Φ_{Ω_s} represents the total flow within Ω_s, whereas Φ_{Ω_c} is the total flow within the solid angle Ω_c subtended at the source by the entrance opening of the microwave cavity. The trajectories of OH radicals in both Λ-doublet states are calculated numerically from Eq. (4-1,2,3) for 60 values of the molecular velocity and 50 values of the entrance angle to the selector for each M_J substate. The efficiency is then determined by counting the molecules which enter the microwave cavities and averaging over the velocity distribution at a kinetic temperature of 300 K. Values for the selector efficiency using the geometry shown in Fig. 4.4 are given in Table 4.1, where the solid angle Ω_c of both microwave cavities is replaced by the angle Ω_c' of the exit opening of the state selector, which is smaller than Ω_c.

If we assume a field free region between the state selector and the microwave cavities, the population of the various M_F substates at the entrance of the microwave cavity will again be mixed and become evenly distributed over all M_F substates. In this case an effective selector efficiency for the total F state, analogous to Eq. (4-4) with M_J replaced by F, can be defined by:

$$S_{eff}(\pm,J,F) = \frac{1}{2F+1} \sum_{M_F} S(\pm,J,F,M_F) \qquad (4\text{-}5)$$

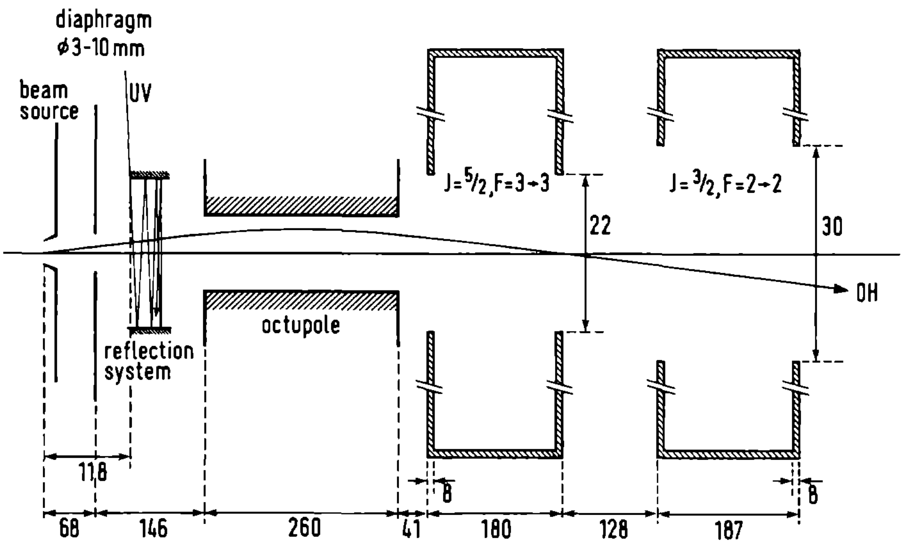

Fig. 4.4 The geometry during the UV induced population transfer experiments. All dimensions are in mm. Also shown are the reflected UV beam and the trajectory of an OH radical in an upper Λ-doublet state.

upper/lower Λ-doublet state	J	M_J	$S(\pm,J,\|M_J\|)$ at specified voltage (kV) 3.2	7	10	15	20	25
+	3/2	3/2	0.27	0.44	0.48	0.51	0.53	0.52
	3/2	1/2	0.07	0.21	0.29	0.37	0.43	0.47
$S_{eff}(+,3/2,F=2)$			0.23	0.39	0.44	0.48	0.51	0.51
−	3/2	3/2	−0.18	−0.19	−0.20	−0.20	−0.20	−0.20
	3/2	1/2	−0.14	−0.17	−0.18	−0.19	−0.19	−0.19
$S_{eff}(-,3/2,F=2)$			−0.16	−0.18	−0.19	−0.19	−0.19	−0.20
+	5/2	5/2	0.13	0.35	0.45	0.54	0.59	0.62
	5/2	3/2	0.05	0.20	0.31	0.42	0.49	0.54
	5/2	1/2	0.00	0.02	0.05	0.12	0.18	0.25
$S_{eff}(+,5/2,F=3)$			0.09	0.26	0.35	0.45	0.51	0.55
−	5/2	5/2	−0.14	−0.18	−0.18	−0.19	−0.19	−0.20
	5/2	3/2	−0.12	−0.16	−0.17	−0.18	−0.19	−0.19
	5/2	1/2	−0.05	−0.10	−0.12	−0.14	−0.16	−0.17
$S_{eff}(-,5/2,F=3)$			−0.10	−0.14	−0.15	−0.17	−0.18	−0.18

Table 4.1 The state selector efficiencies $S(\pm,J,|M_J|)$ as a function of selector voltage for the rotational states $X^2\Pi_{3/2}$, J=3/2 and $X^2\Pi_{3/2}$, J=5/2 in the geometry given in Fig. 4.4. Also given are the effective efficiencies for the F=2 and F=3 hyperfine states. A negative efficiency for a given state means that less molecules in that state enter the cavity than in the case of no voltage applied to the selector.

In this expression the selector efficiency for a particular $|J,F,M_F\rangle$ substate is equal to the efficiency of the $|J,M_J\rangle$ substate connected to $|J,F,M_F\rangle$ by the correlation:

$$J = 3/2: \quad |M_J| = \min(3/2, |M_F| + 1/2) \text{ for } F = 2,+ \text{ and } F = 1,-$$
$$|M_J| = \max(1/2, |M_F| - 1/2) \text{ for } F = 2,- \text{ and } F = 1,+$$

$$J = 5/2: \quad |M_J| = \min(5/2, |M_F| + 1/2) \text{ for } F = 3,+ \text{ and } F = 2,-$$
$$|M_J| = \max(1/2, |M_F| - 1/2) \text{ for } F = 3,- \text{ and } F = 2,+$$

The flow Φ_c of molecules in a $|\pm,J,F,M_F\rangle$ substate entering the microwave cavity is then obtained by dividing the total flow into the selector of molecules in the $|\pm,J,F\rangle$ state, which is determined by the effective selector efficiency, by the number of magnetic substates:

$$\Phi_c(\pm,J,F,M_F) = \frac{\Phi_{\Omega_s}(\pm,J,F)}{2F+1} \left[S_{eff}(\pm,J,F) + \frac{\Omega_c'}{\Omega_s} \right] \qquad (4\text{-}6)$$

assuming both Λ-doublet states to be equally populated.

As shown by ter Meulen (MEU 76) the observed microwave lines consist only of $\Delta M_F = 0$ transitions. The maximum S/N ratio for a $\Delta F=0$ main line transition, in case of a field free region between the selector and microwave cavity, is calculated using the expression given by ter Meulen, yielding:

$$(S/N)_{max} \;(:)\; \left[\frac{F(F+1)}{2F+1} \right]^{1/2} |\mu_{F,F}| \times$$
$$\left[\Phi_{\Omega_s}(+,J,F)\left\{S_{eff}(+,J,F) + \frac{\Omega_c'}{\Omega_s}\right\} - \Phi_{\Omega_s}(-,J,F)\left\{S_{eff}(-,J,F) + \frac{\Omega_c'}{\Omega_s}\right\} \right] \qquad (4\text{-}7)$$

if summation over all M_F substates is performed. Here $\mu_{F,F}$ represents the dipole moment matrix element of the $^2\Pi_{3/2}$, J, F $\rightarrow$ F transition. Values for the effective selector efficiency are also given in Table 4.1.

If no field-free region is present between the selector and the microwave cavity, the population distribution over the various M_F substates will be conserved in the cavity (apart from possible transitions induced by Fourier components of the time varying fringing field seen by the molecules). The maximum ratio S/N is then given by:

$$(S/N)_{max} (:) \ [F(F+1)(2F+1)]^{-1/2} |\mu_{F,F}| \times$$

$$[\Phi_{\Omega_s}(+,J,F) \sum_{M_F} |M_F| \{S(+,J,F,M_F)+\frac{\Omega'_c}{\Omega_s}\} - \Phi_{\Omega_s}(-,J,F) \sum_{M_F} |M_F| \{S(-,J,F,M_F)+\frac{\Omega'_c}{\Omega_s}\}] \tag{4-8}$$

Relative values for $(S/N)_{max}$, normalized to unity at V = 25 kV state selector voltage assuming the electric field to be given by Eq. (4-3), are shown in Fig. 4.5 in case of a field-free region between the selector and the cavity. The discrepancy between the measured and calculated curves is probably due to the fact that in the measured values at 25 kV contributions exist from molecules coming near the rods. In this region the field approximation (4-3) is no longer valid and the exact expression given by Vonbun (VON 58) should be used, which yields a stronger field near the rods. As a consequence more molecules are selected at 25 kV compared to the calculations. At lower selector voltages the relative contribution to the total signal from molecules coming in the region, where the field approximation breaks down, is smaller, in which case the calculated selector efficiencies will deviate less from the values in the experiment. This will cause the calculated microwave intensity, taken relative to its value at 25 kV, to be higher than the observed value, which is in agreement with the result shown in Fig. 4.5. Insertion of the exact expression for the electric field into the calculations, however, would require the solution of a three-dimensional system of differential equations to determine the trajectory of the molecule inside the selector, because this trajectory will be a spiral. In the present model the trajectory is in a plane, which requires far less computational time to determine the selector efficiencies. In view of the fact that 3000 trajectories are calculated to determine the selector efficiency implementation

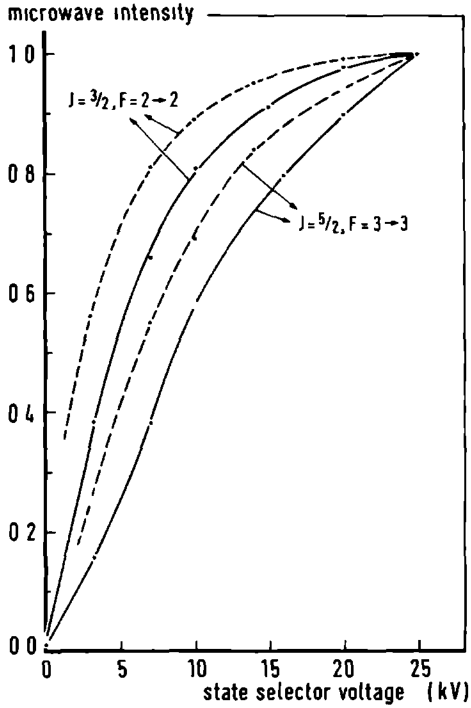

Fig. 4.5 The microwave intensity of the $X^2\Pi_{3/2}$, $J = 3/2$, $F = 2 \rightarrow 2$ and $X^2\Pi_{3/2}$, $J = 5/2$, $F = 3 \rightarrow 3$ transitions, normalized to unity at 25 kV, versus state selector voltage. The solid curve shows measured values and the dashed line represents calculated intensities.

of the exact expression is omitted. The influence of the fringing fields also tends to increase the number of selected molecules and therefore may also (partly) account for the observed discrepancy.

It should be noted, that anisotropic flow of the OH radicals into the selector is not accounted in the calculations. If excitation by a single parallel UV beam is used in the region between the source and state selector, anisotropies occur because only a small angular portion of the molecular beam is excited by the narrow band UV radiation. In our case, these effects will be significantly decreased by the tilted mirror set-up.

4.4 THE MICROWAVE DETECTION SYSTEM

The superheterodyne microwave detection system used to measure the population transfer effects produced by the UV pumping has been described before (VER 69). Basically, the microwave power, generated by a klystron oscillator and reflected by the cavity, is down-converted to an intermediate frequency of 30 MHz by mixing with a local oscillator signal (obtained from a separate klystron) and subsequently amplified and demodulated by a phase-sensitive detector (PAR, model 120) tuned to the reference frequency of 120 Hz provided by the beam chopper. The frequency of the primary oscillator is stabilized by mixing a small fraction of its output power with the signal from a combined frequency synthesizer (Rohde & Schwartz XSU+XUC, Schomandl ND100M), which is set 30 MHz from the desired klystron frequency. The resulting 30 MHz beat frequency is phase-locked to a 30 MHz reference signal by a Schomandl FDS 30 syncriminator. Scanning of the klystron frequency is accomplished by varying the frequency of either the reference signal or the synthesizer. The local oscillator frequency in turn is locked to the primary source by a similar method, replacing the synthesizer signal by the signal from the primary oscillator. The detection of a molecular transition is accomplished by monitoring the increase of the reflected microwave signal caused by the stimulated emission by the OH radicals inside the cavity. In this experiment microwave detection is performed on the $X^2\Pi_{3/2}$, $J = 3/2$, $F = 2 \rightarrow 2$ and $X^2\Pi_{3/2}$, $J = 5/2$, $F = 3 \rightarrow 3$ main line transitions at 1667.35903(10) MHz and 6035.09321(20) MHz, respectively (MEU 76). The effects of population transfer manifest themselves in a change of the measured microwave intensity. Because these effects are very small, long time integration techniques are used to improve the S/N ratio. The measurements are repeated a large number of times both with and without UV excitation and the results

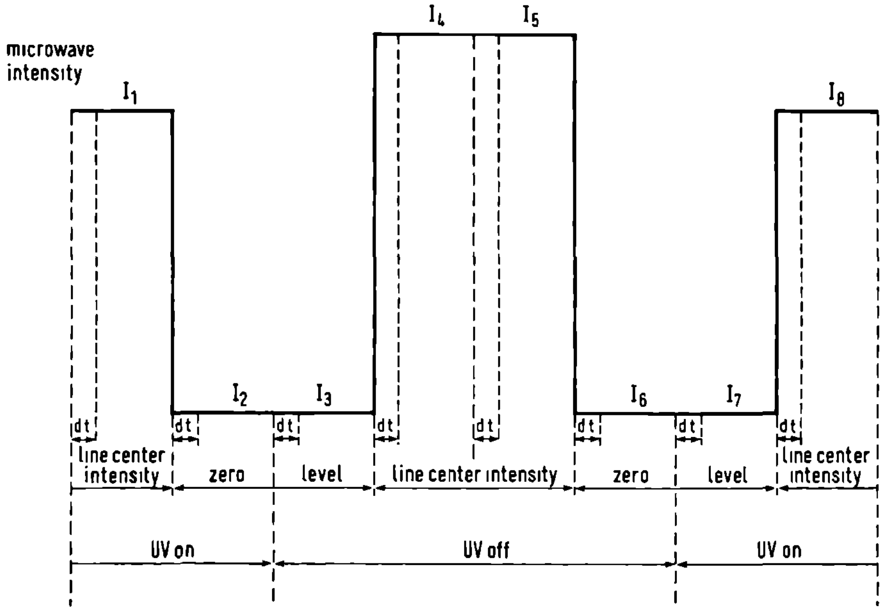

Fig. 4.6 The measuring procedure for detection of UV induced population transfer effects on the microwave intensity. Each step lasts 16 s, starting with 6 s dead time (d.t.). Each cycle of detection at the J = 3/2 transition is followed by a similar cycle for the J = 5/2 line.

are processed digitally. The measuring procedure used to accomplish this is shown schematically in Fig. 4.6. The dead time (d.t.) shown is required to avoid RC effects when switching from the top of the microwave line to the base line at 20 kHz from the line center or vice versa. Switching of the UV intensity is accomplished by a mechanical shutter in the UV beam. The cycle shown in Fig. 4.6 is completed for the J=3/2 and J = 5/2 microwave transitions alternately. The measuring sequence is reversed during each cycle to eliminate possible drift effects. During the sampling time of exactly 10 s, determined by the gating time of a frequency counter, the lock-in output signal is fed into a voltage to frequency converter (VIDAR, model 251) whose output is sampled by the counter (HP, model 5245L) phase-locked to a 1 MHz reference frequency. At the end of each sampling period of 10 s the measured frequency is recorded onto paper tape by a tape punch (FACIT, model 4070), after which computer processing is done. A complete cycle, measuring both the $J = 3/2$ and $J = 5/2$ microwave transitions takes 256 s. Usually, the total number of cycles recorded during a measuring run varied between 15 and 27.

Using the nomenclature shown in Fig. 4.6 the effect X of the UV induced population transfer on the microwave intensity can be calculated from the relation:

$$X = \tfrac{1}{2}\left[\frac{I_1 - I_2}{I_4 - I_3} + \frac{I_8 - I_7}{I_5 - I_6} \right] \qquad (4\text{-}9)$$

If the measuring error in each of the eight steps in a cycle is assumed to be equal to $N/\sqrt{10}$, where N represents the noise observed at the output of the lock-in amplifier at RC=1 s, the relative error in X after M complete cycles, in case of small effects, is given by :

$$\frac{S_X}{X} = \frac{1}{\sqrt{5M}} \left(\frac{S}{N} \right)^{-1} \qquad (4\text{-}10)$$

where S/N is the signal to noise ratio at RC = 1 s. Typical values of S/N at a state selector voltage of 25 kV are 100 for the $X^2\Pi_{3/2}$, $F = 2 \rightarrow 2$ microwave transition and 80 for the $X^2\Pi_{3/2}$, $J = 5/2$, $F = 3 \rightarrow 3$ transition. Under these circumstances the obtainable relative accuracy in X is approximately 10^{-3}. In practise, however, the accuracy is limited to at least 14%, which is probably due to fluctuation of the UV intensity and alignment of the UV beam.

4.5 THE OH ABSORPTION CELL

The Doppler broadened linewidth due to the divergence of the molecular beam is in the order of 100 MHz. The measuring accuracy of our wavelength meter (monochromator Hilger & Watts, type Monospek 1000) is only 0.1 Å in the visible region corresponding to an uncertainty of 15 GHz in the UV region. It is clear from these values that a search for a UV transition of OH in the beam maser is rather time consuming, also because the UV frequency cannot be scanned over more than 6 GHz. To overcome this problem an absorption cell for OH was constructed, where the Doppler linewidth is about 3.9 GHz. The set-up is shown in Fig. 4.7. The production of OH is done by the usual reaction $H + NO_2 \rightarrow OH + NO$ (MEU 76). The OH radicals are excited by the UV just in front of the NO_2 injecting glass capillary array, positioned at the end of the flow tube. The pressure in the interaction region is typically 0.05 Torr. In this situation searching is done by sweeping the transmission frequency of the narrow band etalon in the laser cavity, which causes mode hops and therefore changes in the laser frequency by approximately 300 MHz (in the UV 600 MHz). The molecular absorption line will then be scanned in about six mode

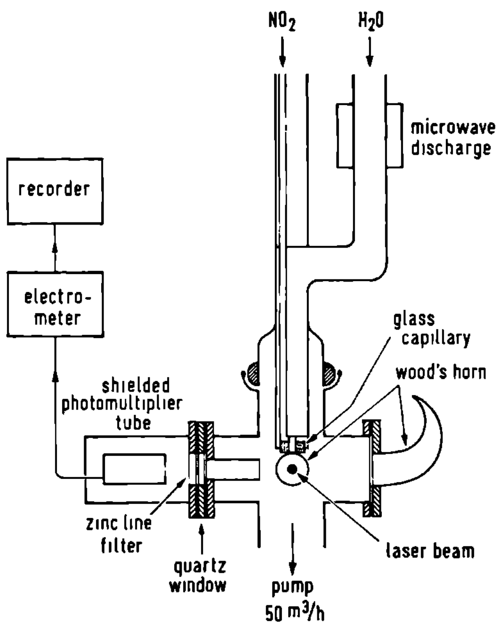

Fig. 4.7 Outline of the OH absorption cell set-up.

hops. This technique greatly facilitates searching because the laser frequency can now be scanned manually over a large distance (typically ∿30 GHz) without the danger of missing the OH absorption line.

The fluorescence radiation is measured by a photo-multiplier tube of the same type as used in the beam maser (EMI 9789 QA). The output current is measured by an electrometer (Keithley, model 610C) connected to a strip chart recorder. To reduce background radiation an atomic zinc line filter, having a transmission of 30% at 300 nm, is mounted in front of the photo-cathode. The background noise is further reduced by blackening of the entire gas cell and part of the flow tube and by the use of a Wood's horn to capture the UV beam; another horn is placed towards the photo-cathode as shown in Fig. 4.7. The solid angle subtended by the photo-cathode at the interaction region is 10^{-3} sr, which, together with a quantum efficiency of 17% and a total gain of 2×10^{7}, results in a detection efficiency of 1.6×10^{-16} C/photon. At the average UV power of 0.1 mW employed in the experiment the anode current is 0.2 mA, yielding a total of 1.3×10^{12} excitations per second in the absorption cell. The Doppler widths of the measured transition lines are 3.2 GHz, which is somewhat lower than expected. This may be caused by the fact that due to the strong reactivity of OH the preferential flow direction will be towards the vacuum pump, which causes a narrowing of the Doppler profile with respect to the pure isotropic situation.

CHAPTER 5

THE EXPERIMENTAL RESULTS

5.1 THE HYPERFINE STRUCTURE OF THE $A^2\Sigma^+_{1/2}$ STATE

The hyperfine splittings, belonging to the rho-doublet components of the rotational levels $K = 0$ through 5 in the $A^2\Sigma^+_{1/2}$ state, were measured by the UV excitation from the $X^2\Pi_{3/2}$ state in the wavelength region 306.8-308.3 nm: $K = 0,1$ and 2 by absorption from the $J = 3/2$ state, while the $K = 3,4$ and 5 levels were excited from the $X^2\Pi_{3/2}$, $J = 5/2$, 7/2 and 9/2 states, respectively. Phase-sensitive detection at RC = 1 s was performed on all transitions, whereas some splittings were also recorded directly by feeding the output of the amplifying electrometer to a strip chart recorder. Fig. 5.1 shows a typical recording for both situations. The high noise level in the direct recording is due to scattered UV detected by the photo-multiplier. The total anode current in this situation, after correction for the background signal, is 2.6×10^{-8} A, corresponding to approximately 1.3×10^{6} excitations per second by the UV beam. In all cases the adjustable diaphragm at the entrance of the radiation chamber was set to ⌀ 3 mm in order to minimize line broadening due to the divergence of the molecular beam. Observed linewidths are typically between 120 and 150 MHz, which prevents the hyperfine splittings of the ground state from being resolved, because these are smaller than 55 MHz and other methods of frequency calibration have to be used. Calibration has been performed by feeding a small fraction of the fundamental laser radiation into a thermally insulated and calibrated interferometer (Tropel, model 216 V), which is operated at zero voltage and whose output is used as a marker during a frequency scan. The free spectral range (FSR) of this interferometer is determined by measuring the known hyperfine splitting of the D_2 line of sodium at 589 nm in an atomic beam set-up, yielding: FSR = 302.2 ± 1.2 MHz. In the UV the distance between two frequency markers corresponds to exactly twice his value.

To determine the actual hyperfine splittings $\Delta\nu$ two

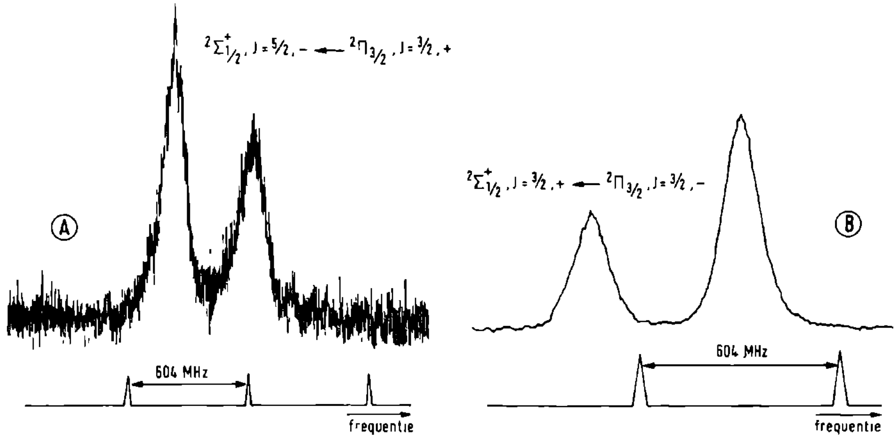

Fig. 5.1 Typical recordings of rotational transitions to the $A^2\Sigma^+_{1/2}$ state, split by the hyperfine interaction in the Σ state. Curve (A) represents a direct recording, curve (B) is a phase-sensitive measurement. The frequency markers are produced by the transmission of a fixed interferometer.

corrections have to be applied to the observed values:

1. Thermal drift of the calibration interferometer results in different distances between the frequency markers when scanning up or down. The hyperfine splitting $\Delta\nu_\pm$ measured on the recording during up (+) and down (−) scans, respectively, of the UV frequency is related to the actual splitting $\Delta\nu$ in MHz by:

$$\Delta\nu_\pm = \frac{r\,\Delta\nu}{S_\pm} \qquad (5\text{-}1)$$

where use is made of the fact that the molecular transitions are free of drift; r represents the speed of the strip chart recorder and $S_\pm$ is the scan speed of the UV frequency in the upward (+) or downward (−) direction. If the drift of the transmission maxima of the interferometer is constant over the measuring period, which turned out to be a reasonable assumption in our case, the distances FSR_+ and FSR_- between two markers, measured on the recording, during up and down scans, respectively, are given by:

$$FSR_{\pm} = \frac{r\,FSR}{\frac{1}{2}S_{\pm} \mp d} \tag{5-2}$$

Herein d is the drift velocity of the transmission maxima of the interferometer in the visible and FSR its free spectral range which is given above; the factor ½ in the denominator of the right hand side accounts for the fact that the markers are produced by the fundamental frequency, which is scanned at half the scan speed in the UV. The influence of this drift is then eliminated by computing the splittings according to the relation:

$$\frac{\Delta\nu}{FSR} = 2\,\frac{FSR_+^{-1} + FSR_-^{-1}}{\Delta\nu_+^{-1} + \Delta\nu_-^{-1}} \tag{5-3}$$

The recorder speed is assumed to be equal during up and down scans; the frequency scan rates, however, need not to be equal. Thermal drift that occurred during calibration of the interferometer was also corrected in this way. The contribution to the experimental error by the residual interferometer drift fluctuations is estimated from these calibration measurements to be less than 0.1%, which is far less than the experimental measuring accuracy of approximately 0.5% and can be neglected.

2. The transitions from two different hyperfine states in a $\Pi_{3/2}$ Λ-doublet to the same $A^2\Sigma^+_{1/2}$ hyperfine state coincide within the observed Doppler width $\Delta\nu_D$ of the transitions (the Σ-state hyperfine splittings turn out to be larger than $\Delta\nu_D$). In the $\Delta J = 0$ transitions the $\Delta F = 0$ components are at least a factor of five stronger than the $\Delta F = \pm 1$ lines, whereas the reverse occurs in the $\Delta J = \pm 1$ transitions.

If the weak components are neglected, the observed splittings are given by the sum or the difference of the hyperfine splittings of the $A^2\Sigma^+_{1/2}$ and $X^2\Pi_{3/2}$ states involved, depending on the ordering of the F levels. Due to the weak components, however, a shift of the top of the composite line occurs relative to the center frequency of the strong component. A correction to eliminate this effect is applied by calculating the shift numerically from the theoretical intensity ratio, the ground state hyperfine splitting and the line shape, which is taken to be Gaussian as observed for the single line component in a $\Delta J = \pm 1$ transition. The corrections obtained in this way varied from 12.7 MHz for the $A^2\Sigma^+_{1/2}$, $J' = 3/2,- \leftarrow X^2\Pi_{3/2}$, $J = 3/2,+$ complex to less than 1 MHz for the transitions involving the $^2\Pi_{3/2}$, $J \geq 5/2$ states.

The resulting values for the hyperfine splittings of the $A^2\Sigma^+_{1/2}$ state of OH are given in Table 5.1. The experimental errors quoted are the standard deviations from at least 10 recordings (five up and five down). The contribution to the experimental error by the overlap is estimated to be smaller: changing the relative strength R of the strong and weak components by 10% yields a shift smaller than 0.8 MHz for the $A^2\Sigma^+_{1/2}$, $J' = 3/2,- \leftarrow X^2\Pi_{3/2}$, $J = 3/2,+$ complex, which is regarded as typical for the transitions leaving from the $^2\Pi_{3/2}$, $J = 3/2$ state. Changes for $J \geq 5/2$ are negligible due to the high values of R involved.

The frequency separation between the $J = 1/2$, $F = 0$ and $J = 3/2$, $F = 2$ hyperfine levels of the $A^2\Sigma^+_{1/2}$, $K = 1$ state was measured by scanning the UV frequency via mode hops of the fundamental dye laser radiation. This method, which produces frequency jumps in the UV equal to the UV mode spacing quoted in Sect. 3.4, was necessary, because the required range was larger than 6.6 GHz, the largest continuous stabilized scan possible in the present laser system. Because the required distance was very nearly an integral multiple of the UV mode spacing, the scan, initiated at

K	J	observed splitting [MHz]	calculated splitting [MHz]	observed minus calculated splitting [MHz]
0	1/2	777.9(4.0)	777.8	0.1
1	1/2	198.1(1.6)	199.4	-1.3
	3/2	490.1(2.2)	490.0	0.1
2	3/2	276.5(1.8)	275.7	0.8
	5/2	436.0(2.2)	438.9	-2.9
3	5/2	303.4(1.6)	301.8	1.6
	7/2	415.9(1.9)	417.0	-1.1
4	7/2	319.1(2.2)	315.6	3.5
	9/2	404.4(2.3)	404.8	-0.4
5	9/2	323.2(2.0)	324.2	-1.0
	11/2	398.3(2.3)	397.0	1.3

Table 5.1 The observed and calculated hyperfine splittings in the $A^2\Sigma^+_{1/2}$ state of OH.

the top of the first line, could be stopped when the side of the second line was reached. Comparison of the fluorescence intensity at this point of arrival with the intensity at the top of the second line then determines, together with the number of mode hops, the total length of the frequency scan. Using this method the distance between the $A^2\Sigma^+_{1/2}$, $K = 1$, $J = 1/2$, $F = 0$ and $J = 3/2$, $F = 2$ hyperfine levels was measured to be 10745(45) MHz after application of the corrections discussed above. This value allows the determination of the rho-doubling in the $A^2\Sigma^+_{1/2}$, $K = 1$ state.

From the experimental values for the hyperfine splittings, as given in Table 5.1, and the measured value of the spacing between the $J = 1/2$, $F = 0$ and $J = 3/2$, $F = 2$ levels in the $A^2\Sigma^+_{1/2}$, $K = 1$ state the molecular hyperfine coupling constants b and c and the rho-doubling constant γ are calculated using the matrix elements given in Sect. 2.1 to determine the energy eigenvalues. The discussion in Sect. 2.1 shows, that the Hamiltonian matrix factorizes into blocks of 2×2 matrices, each describing a $\Delta K = \pm 2$ or $\Delta K = 0$ interaction. The $\Delta K = +2$ interactions give contributions to the hyperfine splittings in the order of 10 kHz, which is far below the experimental accuracy. Contributions to the hyperfine energies by interaction between the $A^2\Sigma^+_{1/2}$, $X^2\Pi_{1/2}$ and $X^2\Pi_{3/2}$ states are also expected to be below the experimental accuracy. In order to minimize correlation between the molecular parameters the quantities γ, c and $b + c/3$ are determined from a least squares fit of the spectrum using the inverse squared measuring errors of the splittings as weights. The resulting values are shown in Table 5.2. The values of 227 and 509 MHz for the $J = 1/2$ and $J = 3/2$ levels, respectively, of the $K = 1$ state deduced by German et al (GER 73) from their measurements on OD turn out to be somewhat

molecular constant	value [MHz] this work	value [MHz] other work
$b + c/3$	777.8(2.0)	$b = 719.0(1.2)$ (RAA 80)
c	165.8(2.8)	160.5(0.9) (RAA 80)
γ	7130 (30)	6875(75) (LIE 80)
		6810(20) (DES 77a)
		7050(2100) (GER 73)

Table 5.2 The hyperfine coupling and rho-doubling constants of OH in the $A^2\Sigma^+_{1/2}$ state.

higher than the present ones. The value of $\gamma = 7.05$ GHz, however, is consistent with our result within their large error (30%). The result of Diecke and Crosswhite (DIE 62) and Destombes (DES 77a) deviate strongly from the present value. Recently Liebermann et al (LIE 80) measured the rho-doubling of the $K = 1$ through 5 levels of the $A^2\Sigma^+_{1/2}$ state of OH optically by recording the fluorescent spectrum produced by excitation with a frequency doubled dye laser pumped by a pulsed nitrogen laser and obtained the value $\gamma = 6875(75)$ MHz. According to the information available, the hyperfine structure of the $A^2\Sigma^+_{1/2}$ state was not resolved in this measurement. The discrepancy with our result might be partly due to the neglect of the large hyperfine splitting of the $A^2\Sigma^+_{1/2}$ state, resulting in a shift of the top of the composite line relative to the position that would be obtained if no hyperfine splitting was present. Raab et al (RAA 80) reported accurate measurements of the hyperfine b and c constants of the $A^2\Sigma^+_{1/2}$ state by the use of quantum-beat spectroscopy and obtained the results shown in Table 5.2, which are in fair agreement with the present values.

The experiments to study UV induced population transfer effects in OH involve the excitation via the $A^2\Sigma^+_{1/2}$, $J' = 3/2$, $F' = 2,+ \leftarrow X^2\Pi_{3/2}$, $J = 3/2$, $F = 2,-$ transition (called $Q_1(1)$) or $A^2\Sigma^+_{1/2}$, $J' = 3/2$, $F' = 2,+ \leftarrow X^2\Pi_{3/2}$, $J = 5/2$, $F = 3,-$ transition (called $P_1(2)$) at 307.9337 nm and 308.7293 nm, respectively (ENG 72). In both cases microwave detection is performed on the $X^2\Pi_{3/2}$, $J = 3/2$, $F = 2 \leftarrow 2$ as well as on the $J = 5/2$, $F = 3 \leftarrow 3$ transition in a measurement cycle as described in Sect. 4.4. The typical UV power P_o, coupled into the beam maser, was 0.14 mW in case of $Q_1(1)$ excitation and 0.20 mW for the $P_1(2)$ transition. The excitation efficiency η, defined as the fraction of molecules from the OH beam excited by the UV, in the limit of weak interactions (Chap. 2) is given by the expression:

$$\eta = \sum_{i=0}^{N} W_i t_i f_i \tag{5-4}$$

Herein W_i represents the radiative transition rate in the i-th passage of the UV beam through the molecular beam, t_i the corresponding interaction time, f_i the maximum fraction of molecules that can be excited during the i-th passage and $N = 40$ is the number of reflections in the tilted UV mirror system. The fraction f_i of molecules with velocity v in a OH beam of diameter 2D and excited by a UV beam of diameter $2H_i$ ($H_i < D$) and linewidth $\Delta\nu$, is given by:

$$f_i = \frac{4H_i}{\pi D} \frac{\Delta\nu}{\Delta\nu_B} \tag{5-5}$$

with $$\Delta\nu_B = 2\nu_o \frac{v}{c} \sin\theta_m \tag{5-6}$$

where θ_m is the divergence of that part of the OH beam that is focused into the microwave cavity by the state selector and is therefore dependent on the quantum state and selector efficiency. The factor $\Delta\nu/\Delta\nu_B$ represents the excited fraction of the absorption profile of the entire OH beam, having a width $\Delta\nu_B$ due to

Doppler broadening. If a monochromatic UV beam of Gaussian spatial geometry is assumed equivalent to a parallel UV beam with a Gaussian frequency profile the excitation rate W_i is given, according to Eq. (2-15), by the expression:

$$W_i = \frac{B_{12}P(\nu_{12},\nu_{12})}{c\pi H_i^2} = \frac{2B_{12}P_i}{c\pi H_i^2\Delta\nu}\sqrt{(\frac{\ln 2}{\pi})} \qquad (5\text{-}7)$$

Herein $P(\nu_{12},\nu_{12})$ represents the power per unit of bandwidth in the center ν_{12} of the frequency profile of the UV radiation and P_i is the total power in the UV beam in the i-th passage. The width of the molecular absorption line, determined by the lifetime of the Σ state ($\tau \sim 7\times10^{-7}$ s) and the interaction time ($t_i \gtrsim 1.4\times10^{-7}$ s), is smaller than the effective width $\Delta\nu$ of the UV radiation given by the divergence of the UV beam ($\Delta\nu \sim 17$ MHz), which justifies the approximation of a flat UV spectrum in evaluating Eq. (2-15). The resulting expression for the total fraction η of excited molecules is then given by:

$$\eta = \frac{16B_{12}}{c\pi^2 v}\sqrt{(\frac{\ln 2}{\pi})}\frac{P_o}{D\Delta\nu_B}\sum_{n=0}^{40}\alpha^n \qquad (5\text{-}8)$$

with the parameter α the mirror reflection coefficient ($\alpha \geq 96\%$) and P_o the total power in the incident UV beam. Insertion of appropriate values for the parameters: $v = 717$ m/s, $D = 2.8$ mm, $\Delta\nu_B = 110$ MHz, $\alpha = 96\%$, $P_o = 0.2$ mW, $B_{12} = 6.4\times10^{17}$ m^3/Ws^3 for $Q_1(1)$ and $B_{12} = 6.7\times10^{17}$ m^3/Ws^3 for $P_1(2)$, yields $\eta = 3\%$ for both $Q_1(1)$ and $P_1(2)$ transitions assuming all the molecules within the opening angle of the state selector to be selected. Without state selection the values of D and $\Delta\nu_B$ are 1.2 mm and 49 MHz, respectively, (given by the exit opening of the state selector) yielding $\eta = 15\%$ and 16% for the $Q_1(1)$ and $P_1(2)$ transitions. Assuming a total OH flow of 3×10^{13} s^{-1} into the solid angle of the entrance of the state selector, an occupation factor of 6.1% for the $X^2\Pi_{3/2}$, $J = 3/2$, $F = 2,-$ state and 5.8% for the $X^2\Pi_{3/2}$, $J = 5/2$, $F = 3,-$ state at 300 K, the total number of excitations per second is 6×10^{10} in case of both $Q_1(1)$ and $P_1(2)$ transitions. At 0.2 mW pump power an average fluorescence intensity of 4.1×10^{-4} A is detected, corresponding to 4×10^{10} excitations per second in the $P_1(2)$ transition, which is in reasonable agreement with the estimated value.

The measured values of the relative effect on the microwave intensities at various values of the state selector voltage and scaled to 0.2 mW UV power are shown in Fig. 5.2. A diaphragm ø 10 mm is inserted at the entrance of the radiation chamber. The errors shown correspond to one standard deviation of the mean. During $P_1(2)$ excitation an increase of the microwave intensity is observed for both microwave transitions, whereas the reverse occurs when the $Q_1(1)$ transition is excited. The extremely large measuring

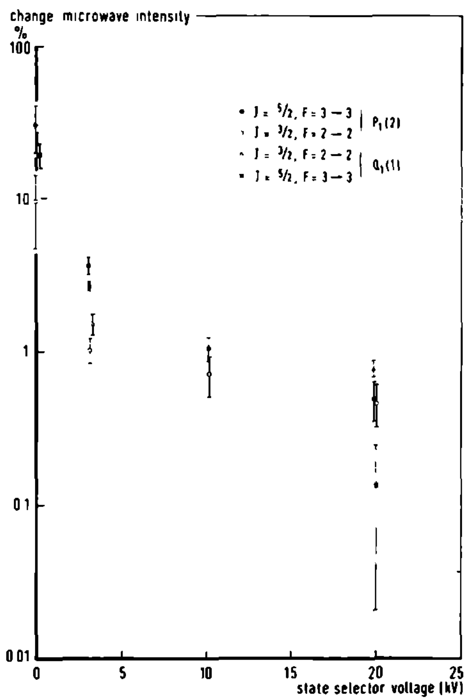

Fig. 5.2 The measured changes of the microwave intensity of the $^2\Pi_{3/2}$, J = 3/2, F = 2 → 2 and $^2\Pi_{3/2}$, J = 5/2, F = 3 → 3 transitions due to UV excitation at the $Q_1(1)$ or $P_1(2)$ transition versus state selector voltage.

error in the result for the $X^2\Pi_{3/2}$, $J = 5/2$, $F = 3 \rightarrow 3$ transition at 20 kV using $Q_1(1)$ excitation is due to the fact, that the observable effect on the microwave intensity of this transition vanishes at high selector voltages, because molecules in the lower Λ-doublet state, which is involved in the population transfer proces, are bent out of the beam by the selector.

Without state selection and UV pumping, emission signals are observed in both microwave cavities with typically $S/N \approx 6$ at $RC = 10$ s, which is approximately a factor two higher than the results of ter Meulen (MEU 76). These signals are due to the population inversion between the hyperfine levels involved, originating in the production region, and are much larger than the intensity changes produced by the UV excitation. The analysis of the results of UV excitation shown in Fig. 5.2 is greatly hampered by the occurrence of this chemical inversion proces. Without state selection the relative effects due to UV excitation do not grow beyond the values shown because of the nonzero lower bound on the microwave intensity produced by the chemical inversion proces. An estimate of the magnitude of the produced population inversion between the hyperfine levels of the Λ-doublets of both the $X^2\Pi_{3/2}$, $J = 3/2$ and $J = 5/2$ states is obtained from measurements of the microwave intensity at various state selector voltages without UV excitation and the selector efficiencies given in Sect. 4.3. These values will then be used in the analysis of the UV induced effects.

If the relative population inversion between the hyperfine levels of a microwave transition, in the absence of UV radiation, is given by the parameter:

$$\varepsilon(J,F) = 1 - \frac{\Phi_{\Omega_s}(-,J,F)}{\Phi_{\Omega_s}(+,J,F)} \tag{5-9}$$

the maximum S/N ratio, according to Eq. (4-7), becomes:

$$(S/N)_{max} (:) \sqrt{\frac{F(F+1)}{2F+1}}\ |\mu_{F,F}|\ \Phi_{\Omega_s}(+,J,F)\beta(J,F) \tag{5-10}$$

with:

$$\beta(J,F) = S_{eff}(+,J,F) - S_{eff}(-,J,F) + \varepsilon(J,F)\{S_{eff}(-,J,F) + \frac{\Omega'_c}{\Omega_s}\} \qquad (5\text{-}11)$$

From measurements of the microwave intensity with and without state selection the value of the relative population inversion $\varepsilon(J,F)$ is then determined via the relation:

$$\frac{S/N(0\ kV)}{S/N(20\ kV)} = \frac{\Omega'_c}{\Omega_s}\frac{\varepsilon(J,F)}{\beta(J,F)} \qquad (5\text{-}12)$$

Herein the relation $S_{eff}(\pm,J,F)=0$ without state selection is used and the selector efficiencies occurring in the expression of β are to be evaluated at 20 kV. The measurements of the effects caused by UV excitation at the $Q_1(1)$ and $P_1(2)$ transitions are performed on different days, resulting in different OH production circumstances and consequently in different values for $\varepsilon(J,F)$ in the $Q_1(1)$ and $P_1(2)$ excitation experiments. Measurement of the microwave signals with and without state selection yielded:

during $Q_1(1)$ series: $\varepsilon(3/2,2) = 0.088(16)$
$\varepsilon(5/2,3) = 0.066(13)$

during $P_1(2)$ series: $\varepsilon(3/2,2) = 0.060(12)$
$\varepsilon(5/2,3) = 0.035(9)$

when a 20% uncertainty in the values of the selector efficiencies is assumed (MEU 76).

For weak interactions the population change $\Delta\Phi_{\Omega_s}(j)$ in hyperfine state $|j\rangle$, due to UV induced excitation from a $X^2\Pi_{3/2}$ state $|i\rangle$ ($\neq|j\rangle$) and subsequent decay from the excited $A^2\Sigma^+_{1/2}$ state $|k\rangle$ is obtained from the relation (A3-13):

$$\Delta\Phi_{\Omega_s}(j) = \frac{A_{kj}}{A}\eta_i\Phi_{\Omega_s}(i) \qquad (5\text{-}13)$$

Herein A represents the total spontaneous emission rate from state $|k\rangle$, A_{kj}/A is the branching ratio from $|k\rangle$ to $|j\rangle$ and η_i the total excitation efficiency defined above. Because Eq. (5-13), in the case of $|j\rangle = |i\rangle$, gives the amount of population returned to state $|i\rangle$ by the decay of state $|k\rangle$, the total population change of state $|i\rangle$ is given by:

$$\Delta\Phi_{\Omega_s}(i) = -(1 - \frac{A_{ki}}{A})\eta_i \Phi_{\Omega_s}(i) \qquad (5\text{-}14)$$

Regarding the $Q_1(1)$ transition as an example ($A = 1.43\times10^6\ s^{-1}$), the condition for weak interaction is met for all crossings of the 0.2 mW UV beam with the OH beam except in the focus, where the excitation efficiency is equal to 34% according to the Einstein theory. This theory is therefore no longer applicable at the focus. The experimental errors, however, turn out to be much larger than the uncertainty in η_i produced by the assumption of a weak radiative interaction. Simultaneous pumping on satellite transitions due to overlap of the $X^2\Pi_{3/2}$ hyperfine states within the UV absorption line profile of 110 MHz is expected to give contributions below the experimental accuracy, because these transitions are at least a factor of 10 weaker due to the combined effect of a lower transition probability and off-resonance excitation.

The relative change D_J in microwave signal of the $X^2\Pi_{3/2}$, $J = 3/2$, $F = 2 \rightarrow 2$ and $J = 5/2$, $F = 3 \rightarrow 3$ transitions, values for which are shown in Fig. 5.2 and which is caused by UV excitation along the $Q_1(1)$ or $P_1(2)$ transitions, is obtained from Eq. (4-7) and Eq. (5-10,11):

$$D_J = \left.\frac{\Delta(S/N)}{S/N}\right|_{J,F} = \pm \frac{S_{eff}(\pm,J,F) + \Omega_c'/\Omega_s}{\beta(J,F)} \frac{\Delta\Phi_{\Omega_s}(\pm,J,F)}{\Phi_{\Omega_s}(+,J,F)} \qquad (5\text{-}15)$$

Herein the + and − sign refers to the $J = 3/2$ and $J = 5/2$ transitions, respectively. Using Eq. (5-13,14) to calculate the population changes induced by the UV excitation, the ratios U_Q and U_P of the relative effects on the $J = 3/2$ and $J = 5/2$ microwave transitions during $Q_1(1)$ and $P_1(2)$ excitation, respectively, become:

$$U_Q = \frac{D_{3/2}}{D_{5/2}} = \frac{14}{15}\left(\frac{1-x}{y}\right)\frac{\kappa}{Z} \qquad \text{for } Q_1(1) \qquad (5\text{-}16a)$$

$$U_P = \frac{D_{5/2}}{D_{3/2}} = \frac{15}{14}\left(\frac{1-y}{x}\right)\frac{Z}{\kappa} \qquad \text{for } P_1(2) \qquad (5\text{-}16b)$$

with:

$$\kappa = \frac{\beta(5/2,3)}{\beta(3/2,2)}\,\frac{S_{eff}(+,3/2,2)+\Omega_c'/\Omega_s}{S_{eff}(-,5/2,3)+\Omega_c'/\Omega_s} \qquad (5\text{-}17)$$

and $$Z = \Phi_{\Omega_s}(+,3/2)/\Phi_{\Omega_s}(+,5/2) \qquad (5\text{-}18)$$

The parameters x and y represent the branching ratios for the $A^2\Sigma^+_{1/2}$, $J'=3/2$, $F'=2,+ \rightarrow X^2\Pi_{3/2}$, $J=3/2$, $F=2,-$ ($Q_1(1)$) and $A^2\Sigma^+_{1/2}$, $J'=3/2$, $F'=2,+ \rightarrow X^2\Pi_{3/2}$, $J=5/2$, $F=3,-$ ($P_1(2)$) transitions, respectively. The factor 14/15 appears, because the flows of molecules in the considered hyperfine states are expressed as a fraction of the flows of molecules in the Λ-doublet states, assuming the magnetic hyperfine substates to be equally populated. Since in both pumping transitions the lower state of the $J=5/2$ Λ-doublet, having a negative selector efficiency, is involved, the observed effect on the $J=5/2$ microwave transition depends strongly on the geometry of source, selector and cavity. This is illustrated by the limiting case of complete state selection, where $S_{eff}(-,5/2,3) \rightarrow -\Omega_c'/\Omega_s$ and consequently $U_Q \rightarrow \infty$ and $U_P \rightarrow 0$. In view of the approximate model of the state selector (neglect of fringing fields and the simplified expression for the electric field) and the spatial extent of the actual OH source, the analysis of the measurements involving the $J=5/2$ state is expected to be less accurate at high selector voltages.

From the measurements with state selection, separate values for the branching ratios are only obtained from the experimental data at 3.2 kV, because no $Q_1(1)$ result is available at 10.1 kV and the $Q_1(1)$ value at 20 kV is subject to a large uncertainty. Insertion of the results shown in Fig. 5.2, the state selector efficiencies given in Sect. 4.3 and the values of ε presented above into Eq. (5-16,17) yields for the branching ratios:

$$x = -0.74(86)$$
$$y = 6.2\ (4.9)$$

Here $Z = 1$ is assumed, corresponding to no anomalous population distribution over the rotational levels at $T = 300$ K. The errors quoted are determined from the uncertainties in ϵ, the selector efficiencies and the experimental results by the well-known relations for error propagation, assuming all errors to be statistically independent. These values of x and y are not meaningful, which is mainly due to the observed larger effect on the $J = 5/2$ microwave transition compared to the $J = 3/2$ result during UV excitation via the $Q_1(1)$ line. The quantity dominating the dependence of U_Q on state selector voltage is the factor $S_{eff}(-,5/2,3) + \Omega_c'/\Omega_s$ in the denominator of Eq. (5-17), which vanishes for high selector voltages. At increasing voltage the value of U_Q is therefore expected to rise; a reduction, however, is observed at 3.2 kV. A possible explanation for this is a decrease of the selecting power of the state selector caused by OH radicals in the lower Λ-doublet level of the $X^2\Pi_{3/2}$, $J = 5/2$ state, that, after defocusing, pass between the rods near the end of the selector and are still captured by the $J = 5/2$ microwave cavity, subtending at the source a solid angle approximately four times the angle of the exit opening of the selector. From these values of x and y no definite conclusions can be drawn. Multiplication of U_P and U_Q from Eq. (5-16) yields an expression:

$$U_P U_Q = \left(\frac{1-x}{y}\right)\left(\frac{1-y}{x}\right) \qquad (5\text{-}19)$$

which depends only on the branching ratios. Insertion of the theoretical values x=0.25 and y=0.37 gives $U_P U_Q = 5.1$, which deviates strongly from the value 2.01(57) obtained from the data at 3.2 kV in Fig. 5.2 and indicates a possible anomaly in the actual values of x and y. However, before definite conclusions can be drawn, more accurate measurements have to be performed. Also more accurate calculations of the state selector efficiencies are required, especially for the lower Λ-doublet levels involved in the UV induced population transfer proces. This might require the application of the exact expression for the electric field inside the selector as given by Vonbun (VON 58), the inclusion of (de)focusing by the fringing fields of the selector, the knowledge of the velocity distribution of the OH radicals in the molecular beam as well as the determination of the relative occupation Z of the $X^2\Pi_{3/2}$, $J = 3/2$ and $J = 5/2$ states.

Without state selection all selector efficiencies vanish and the change in the microwave signal becomes equal to:

$$D_J = \pm \frac{1}{\varepsilon(J,F)} \Delta\Phi_{\Omega_s}(\pm,J,F)/\Phi_{\Omega_s}(+,J,F) \qquad (5\text{-}20)$$

Consequently very large relative effects are possible, which is in agreement with the observations (Fig. 5.2). The parameter κ, defined in Eq. (5-17),then becomes equal to the ratio of the relative population inversions ε at the $J = 5/2$ and $J = 3/2$ microwave transitions. Assuming as before no anomalous population distribution over the rotational levels ($Z = 1$) and the theoretical branching ratios to be applicable the following values of κ are obtained from Eq. (5-16) and the results shown in Fig. 5.2:

$\kappa = 0.63(17)$ for the $Q_1(1)$ series
$\kappa = 0.84(52)$ for the $P_1(2)$ series

From the values of ε presented earlier we obtain:

$$\begin{aligned} \kappa &= 0.75(20) \quad \text{for the } Q_1(1) \text{ series} \\ \kappa &= 0.58(19) \quad \text{for the } P_1(2) \text{ series} \end{aligned} \qquad (5\text{-}21)$$

which is in agreement with the result obtained above.

The branching ratios are determined from Eq. (5-16), Fig. 5.2 and the values of κ presented in (5-21). The result is:

$$x = 0.36(39)$$
$$y = 0.38(31)$$

Within the large error bounds, which are mainly due to the large measuring error in the experimental data for $P_1(2)$ excitation, these values are in agreement with the theoretical predictions. Conclusions regarding possible deviations from the predictions cannot be drawn because of the large uncertainties. Comparison of the theoretical value of $U_P U_Q$ with the result 3.8(2.6) obtained from Fig. 5.2 also produces agreement within the large error bound. Experimental determination of the value of $U_P U_Q$, however, can provide evidence for possible anomalous branching ratios without the need for knowledge of state selector efficiencies and energy level occupations and is therefore a powerful tool to investigate the UV induced population transfer proces.

ASTROPHYSICAL CONSEQUENCES AND CONCLUSIONS

6.1 THE POPULATION TRANSFER PROCES IN INTERSTELLAR OH

The influence of the hyperfine splittings in the $A^2\Sigma^+_{1/2}$ state (reported in the previous chapter) on the UV induced population transfer in interstellar OH is calculated according to the model described in Chap. 2. To evaluate the equations for population transfer the Einstein coefficients for spontaneous emission are calculated with the help of Eq. (A1-4,5) and the expressions for the dipole moment matrix elements of the UV transitions given by ter Meulen (MEU 74). The oscillator strength f_{oo} for the $v = 0 \rightarrow 0$ band is taken equal to 1.03×10^{-3} (DIM 79). For the cascade through the $X^2\Pi_{3/2}$ and $X^2\Pi_{1/2}$ states we use the values of the Einstein A coefficients given by Destombes _et al_ (DES 77).[1] As in Chap. 2 the UV flux density, assumed in the computations, is 10^{-17} $Wm^{-2}Hz^{-1}$, which corresponds to an O5 star ($R_* = 10R_\odot$, $T = 70{,}000$ K) at a distance of 2 ly from the OH formation (LIT 66, TUR 70). Figure 6.1a shows the relative gain factors G_{ij} for the four microwave transitions in the $X^2\Pi_{3/2}$, $J = 3/2$ state, calculated according to Eq. (2-27), as a function of UV optical depth assuming a kinetic temperature of 4.5 K. UV optical depth is defined here in terms of the depth (at line center, in thermal equilibrium and excluding overlap with nearby transitions) at the $A^2\Sigma^+_{1/2}$, $K = 1$, $J = 3/2$, $F = 2,+ \leftarrow X^2\Pi_{3/2}$, $J = 3/2$, $F = 2,-$ transition, The optical depth is temperature dependent via both the population of the ground state and the UV Doppler width (Eq. (2-23,25)). At 4.5 K unit optical depth corresponds to a projected density $N_{OH}L_0$ equal to 9.0×10^{17} m^{-2}, whereas the values at 14 K and 50 K are 1.6×10^{18} m^{-2} and 3.4×10^{18} m^{-2}, respectively. The quantity L_0 is the length of an OH cloud having $\tau_{UV} = 1$. If the parameter η is defined as the ratio of the hyperfine splitting of the considered

---

1) Correction is made for the value of the $X^2\Pi_{3/2}$, $J = 5/2$, $F = 4,- \rightarrow X^2\Pi_{3/2}$, $J = 7/2$, $F = 3,+$ transition, which should read $0.5207\,s^{-1}$.

rho-doublet state (given in Table 5.1) to the full Doppler width at half height of the UV transition, its value at $T = 4.5$ K is less than unity for all lower rho-doublet levels of each rotational Σ state, whereas $\eta > 1$ for all other levels. Figures 6.2a and 6.3a show curves similar to those of Fig. 6.1a at different temperatures (note the change of vertical scale in Fig. 6.3a); at 14 K only transitions to the $K = 0$ rotational state have $\eta > 1$, whereas at 50 K overlap occurs for all hyperfine split rho-doublet states.

The maxima, shown in the curves, correspond to depths at which the $A^2\Sigma^+_{1/2}$, $K = 2$, $J = 5/2$, $F+1,- \leftarrow X^2\Pi_{3/2}$, $J = 3/2$, $F,+$ transitions dominate the inverting population transfer between the Λ-doublet states, whereas the $A^2\Sigma^+_{1/2}$, $K = 3$, $J = 5/2$, $F+1,+ \leftarrow X^2\Pi_{3/2}$, $J = 3/2$, $F,-$ transitions are responsible for the anti-inverting transfer (Fig. 6.4). Radiation corresponding to the transitions to the $A^2\Sigma^+_{1/2}$, $J = 1/2$, $F \neq 0$ and $J = 3/2$ states is already absorbed at these depths due to the large line strengths of transitions to the $K = 1$ states or the strong overlap in the transitions to the $K = 2$ states (the transitions to the two $A^2\Sigma^+_{1/2}$, $J = 1/2$, $F = 0$ states are not efficient for population transfer). With increasing temperature growing overlap between the absorption profiles of the $A^2\Sigma^+_{1/2}$, $J = 5/2$, $F = 3,\pm \leftarrow X^2\Pi_{3/2}$, $J = 3/2$, $F = 2,\mp$ and the $A^2\Sigma^+_{1/2}$, $J = 5/2$, $F = 2,\pm \leftarrow X^2\Pi_{3/2}$, $J = 3/2, F = 1,\mp$ transitions reduces the intensity of the UV radiation in the corresponding bandwidth and consequently the depopulation of the $F = 1$ and $F = 2$ ground state levels of both Λ-doublet states. Due to the smaller hyperfine splitting (Fig. 6.4) the relative increase with temperature of the overlapped line shape areas is lower for the $A^2\Sigma^+_{1/2}$, $K = 3$, $J = 5/2,+$ state ($\Delta\nu_{HF} = 303$ MHz) than for the $A^2\Sigma^+_{1/2}$, $K = 2$, $J = 5/2,-$ state ($\Delta\nu_{HF} = 436$ MHz). This causes the balance to change in favor of the population transfer via the $K = 3$ state as the temperature is increased, resulting in a reduction of the population inversion in the main lines of the ground state and consequently in a reduction of the gain factors at both the 1665 MHz and 1667 MHz transitions. An additional reduction is due to the $T^{-1/2}$ dependence of the gain factor via the linewidth of the microwave transition.

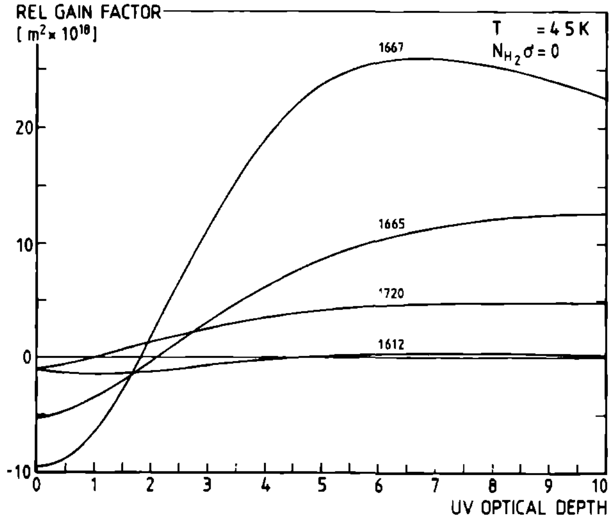

Fig. 6.1a The relative gain factors G_{ij} of the four ground state microwave transitions versus optical depth at $T = 4.5$ K.

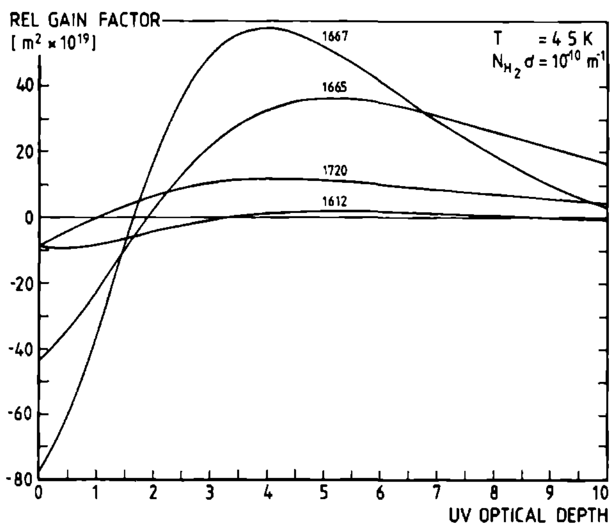

Fig. 6.1b Same as Fig. 6.1a, including collisions with hydrogen at $N_{H_2}\sigma = 10^{-10}$ m^{-1}.

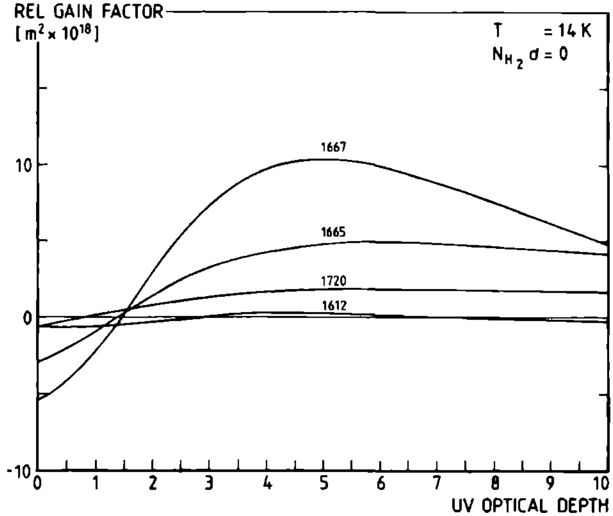

Fig. 6.2a The relative gain factors G_{ij} of the four ground state microwave transitions versus optical depth at T = 14 K.

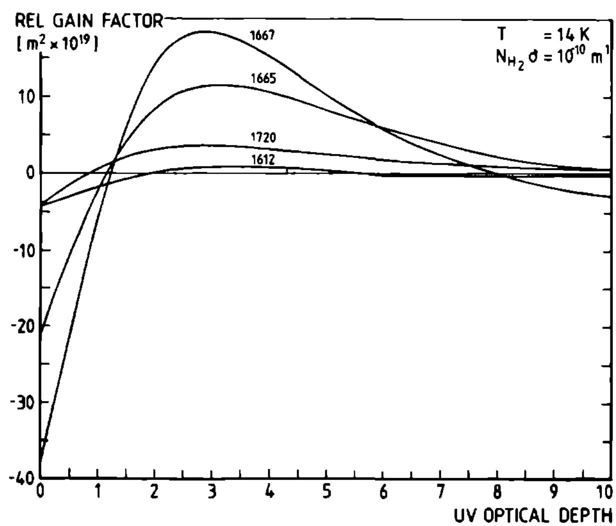

Fig. 6.2b Same as Fig. 6.2a, including collisions with hydrogen at $N_{H_2}\sigma = 10^{-10}\ m^{-1}$.

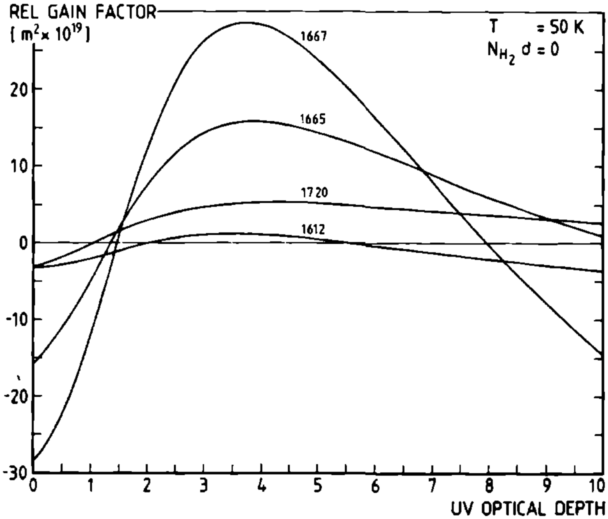

Fig. 6.3a The relative gain factors G_{ij} of the four ground state microwave transitions versus optical depth at $T = 50$ K.

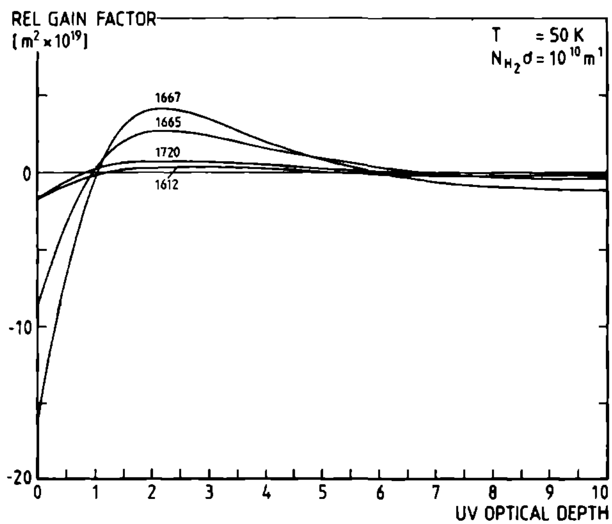

Fig. 6.3b Same as Fig. 6.3a, including collisions with hydrogen at $N_{H_2}\,\sigma = 10^{-10}\ m^{-1}$.

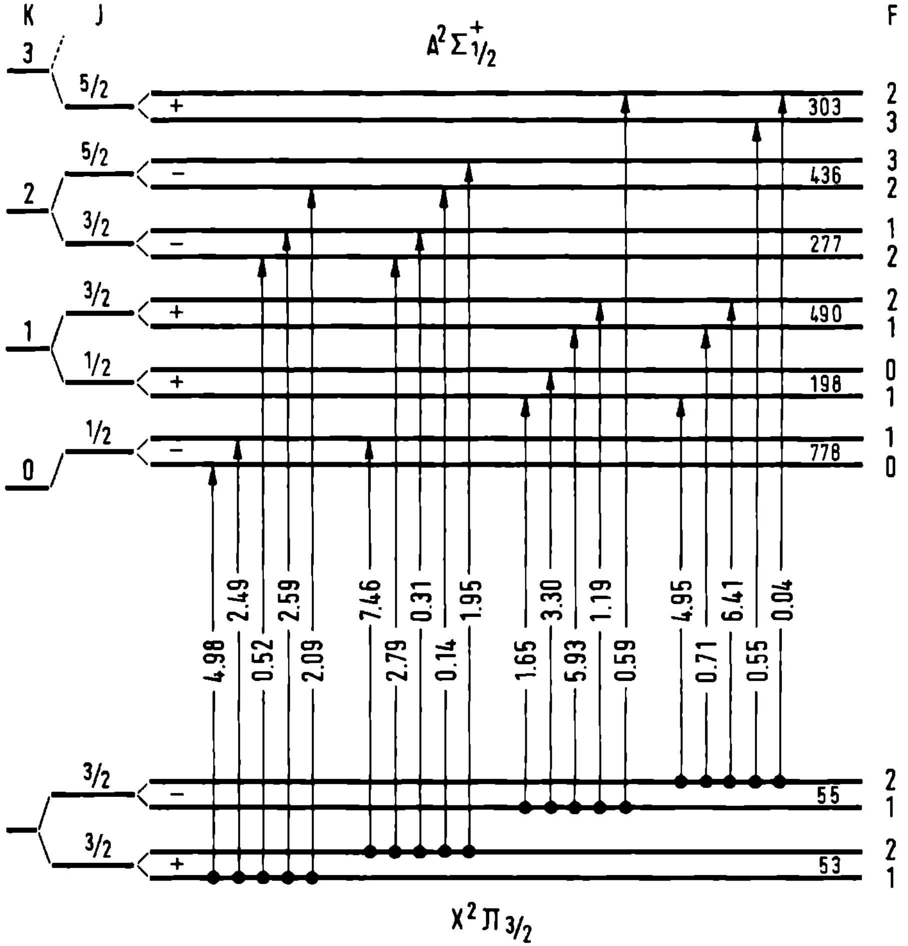

Fig. 6.4 The hyperfine transitions from the $X^2\Pi_{3/2}$, $J = 3/2$ state to the $A^2\Sigma^+_{1/2}$ state in the UV region near 307 nm. The numbers given at the transitions are the Einstein coefficients for absorption relative to 10^{17} $m^3s^{-3}W^{-1}$. The numbers shown between the energy levels are the hyperfine splittings in MHz.

The shift of the maximum of the gain factor to smaller optical depths at increasing temperature is explained by a similar argument: the increase of the anti-inverting population transfer via the $A^2\Sigma^+_{1/2}$, K = 3, J = 5/2,+ state relative to the inverting effects via the K = 2, J = 5/2 state, which occurs when the temperature increases, is compensated by the combination of higher UV fluxes, present at smaller optical depths, and larger line strengths of the transitions involving the K = 2 state. In addition the actual value of the optical depth, in the absence of thermalizing collisions, increases more rapidly than the value based on equilibrium considerations: because of the radiative decay of the excited rotational states the final ground state populations and consequently the UV optical depth are larger than the thermal equilibrium values. This effect, which becomes larger at increasing temperatures, enlarges the shift of the maxima of the curves.

We have also calculated the effect of thermalizing collisions with H_2 on the gain at the four microwave transitions using the model discussed in Chap. 2. The results are shown in Fig. 6.1b, 6.2b and 6.3b (note the change of vertical scale compared to the previous figures). A strong quenching of the relative gain factors is clearly present. In the computations the collision parameter $N_{H_2}\sigma$ is taken equal to 10^{-10} m^{-1}, which corresponds to a H_2 density of 10^3 cm^{-3} when a collision cross section of 10^{-19} m^2 is used (ELI 76). In this situation the ratio between the collisional deexcitation rate C per magnetic sublevel and the UV excitation rate W at the $A^2\Sigma^+_{1/2}$, K = 1, J = 3/2, F = 2,+ $\leftarrow$ $X^2\Pi_{3/2}$, J = 3/2, F = 2,− transition at the front of the OH formation is 0.03 at 4.5 K, 0.05 at 14 K and 0.08 at 50 K. The shift of the maxima in these gain curves towards lower UV optical depths, compared to the collision free situation, is due to the reduction of the radiative contribution to the transfer proces relative to the thermalizing collision part, as the UV flux penetrates into the OH cloud. It is clearly demonstrated by these results that collisional quenching at large optical depths more strongly affects the radiatively induced population inversion between both $F = 2$ levels than between both $F = 1$ levels. At H_2 densities two orders of magnitude higher the collisional deexcitation rate C exceeds the UV excitation rate at the front of the OH cloud by a factor of 3 at 4.5 K and 8 at 50 K and quenches the population inversion ΔN, defined in Eq. (2-28), to values of at most -2.0% at 4.5 K and -0.25% at 50 K at all four microwave transitions. Calculations show, that this quenching reestablishes the absorptive gain ratio 1 : 5 : 9 : 1 for the 1612 MHz, 1665 MHz, 1667 MHz and 1720 MHz transitions at all temperatures and optical depths. Turner's results, including collisions, indicate a substantial enhancement of the maximum gain factor at 1720 MHz relative to the other microwave lines, which does not show in our calculations. In addition, Fig. 6.1b, 6.2b and 6.3b show a strong reduction of the main line gain factors with increasing temperature, which is in contradiction with Turner's results. However, as explained in Chap. 2, his results are probably obtained at a fixed temperature but with diminishing hyperfine splittings in the Σ state. The increase of the maximum gain factors at the main lines is, however, not clear as is the behaviour of the 1720 MHz transition. In addition, the various uncertainties in Turner's model severely hinder a comparison with our results.

As is evident from the strong influence of the collisional effects, deviations from the approximations used in the calculation of the collisional transition rates, presented in Chap. 2, may strongly influence the results obtained above. If in contrast to the present statistical model a rotational- and parity-selective collision proces is assumed, the main line inversion can be increased (GWI 73, BER 76). Therefore a good understanding of the proces of inelastic collisions of hydroxyl with molecular hydrogen is of vital importance to the population transfer mechanism.

The results, shown above, apply to UV excitation of OH radicals having a Gaussian absorption line profile. Comparison of Fig. 6.1a with Fig. 2.4, where a rectangular lineshape at the same temperature was assumed, show large differences. In the results with a rectangular profile the reduction of the gain factor at 1665 MHz relative to the other three ground state microwave transitions is quite remarkable. Whereas always overlap between neighbouring Gaussian line profiles takes place, no overlap is present at all between the rectangular absorption profiles of transitions to different levels in the Σ state at 4.5 K. Compared to the case of a Doppler profile, the maximum gain factor at 1667 MHz is increased slightly, the optimum is shifted to a smaller optical depth and the population inversion between the $F = 2$ levels at large optical depths is significantly reduced, when a rectangular absorption profile is used. It is therefore concluded that the results for the relative gain factors depend strongly on the lineshape assumed in the model.

Under conditions of unsaturated maser action and negligible spontaneous emission, the observed intensity I_{ij} at microwave transition $|i\rangle \leftarrow |j\rangle$ is given by the relation:

$$I_{ij} = I_{ij}(0) \exp(M_{ij}) = I_{ij}(0) \exp\left[\int_0^L G_{ij}(s)\, N_{OH}\, ds \right] \qquad (6\text{-}1)$$

M_{ij} represents the total gain at the considered microwave transition, $I_{ij}(0)$ the microwave intensity incident on the hydroxyl cloud. The integration extends along the line of sight over the total length L of the OH formation. In the one-dimensional model of the OH cloud assumed in the calculations the line of sight is parallel to the UV pumping direction and the total gain M_{ij} at optical depth τ_o is given according to Eq. (6-1) by:

$$M_{ij}(\tau_o) = N_{OH} L_O \int_0^{\tau_o} G_{ij}(\tau)\, d\tau \qquad (6\text{-}2)$$

where τ represents the UV optical depth in thermal equilibrium and $N_{OH} L_O$ is the projected density corresponding to unit optical depth at the considered temperature. Table 6.1 shows values of the total gain M of all four ground state microwave transitions as a function of UV optical depth τ_o for the various kinetic temperatures, including population transfer due to collisions

	T = 4.5 K				T = 14 K				T = 50 K			
τ_{UV}	M_{1612}	M_{1665}	M_{1667}	M_{1720}	M_{1612}	M_{1665}	M_{1667}	M_{1720}	M_{1612}	M_{1665}	M_{1667}	M_{1720}
0	0.0	0.0	0.0	0.0	0.0	0.0	0.0	0.0	0.0	0.0	0.0	0.0
1	-0.8	-3.0	-5.3	-0.4	-0.5	-1.8	-3.5	-0.3	-0.3	-1.3	-2.5	-0.2
2	-1.4	-3.9	-6.0	-0.1	-0.6	-1.2	-2.6	0.1	-0.3	-0.7	-1.7	-0.1
3	-1.6	-2.7	-2.8	0.7	-0.5	0.5	0.2	0.6	-0.2	0.1	-0.4	0.2
4	-1.6	-0.2	2.1	1.8	-0.4	2.3	2.9	1.2	-0.2	0.8	0.5	0.3
5	-1.4	2.9	7.1	2.8	-0.3	3.7	4.9	1.6	-0.1	1.1	0.9	0.5
6	-1.3	6.2	11.2	3.7	-0.3	4.9	6.1	1.9	-0.1	1.3	1.0	0.5
7	-1.1	9.1	14.4	4.6	-0.3	5.6	6.7	2.2	-0.2	1.3	0.9	0.5
8	-1.1	11.7	16.5	5.2	-0.3	6.1	6.8	2.3	-0.2	1.3	0.6	0.5
9	-1.1	13.8	17.8	5.8	-0.4	6.3	6.6	2.4	-0.3	1.1	0.2	0.5
10	-1.1	15.4	18.3	6.2	-0.5	6.4	6.1	2.5	-0.4	1.0	-0.3	0.5

Table 6.1 The total gain of the ground state microwave transitions as a function of UV optical depth, according to the model including collisions ($N_{H_2}\sigma = 10^{-10}\ m^{-1}$). The UV pumping direction is along the line of sight.

with hydrogen at $N_{H_2}\sigma = 10^{-10}\ m^{-1}$ (values for $N_{OH}L_0$ at the considered temperatures are given earlier in this chapter). It is clear from these values, that $T > 14$ K if the gain at the 1665 MHz line should exceed the value at 1667 MHz. Gains in the order of 20 or higher, however, are not obtained at these temperatures, except possibly in very cool and optically thick formations as may be expected from an extrapolation of the data at 4.5 K, in which case the 1665 MHz emission can also exceed the output at 1667 MHz. When the gains are calculated in the absence of collisions, very large values (up to 140 at 4.5 K in the 1667 MHz line) are obtained. Quenching of the population inversion due to microwave transitions across the Λ-doublet, however, will reduce these values. The microwave transition rate W_{ij} is estimated from the relation:

$$W_{ij} = \frac{B_{ij} I_o}{c}\ \Omega_m \exp(M_{ij}) \qquad (6\text{-}3)$$

Here I_o represents the microwave intensity ($T = 3$ K) incident on the OH cloud, B_{ij} is the Einstein coefficient of the considered transition $|i\rangle \rightarrow |j\rangle$ and the solid angle of the amplified microwave emission is taken equal to Ω_m. If the angle is determined purely geometrically Ω_m will be in the order of $(d/L)^2$ with d and L the thickness and length of the OH cloud, respectively (LIT 66). In case of a strictly one-dimensional model Ω_m would then be very small and microwave quenching should be negligible. In this situation the high gains shown in Table 6.1 can be reached. If, however, we allow at this point for beam spreading the microwave quenching is no longer negligible in the region of high total gain and a reduction of the produced gain factors will occur. To obtain an estimate of the influence of microwave quenching we take $\Omega_m = M_{ij}^{-1}$ (LIT 66) in this case and using for the collisional transition rate C_{ij} at 1665 MHz the values of $1.7\times10^{-19}\ s^{-1}$, $3.0\times10^{-19}\ s^{-1}$ and $4.8\times10^{-19}\ s^{-1}$ at 4.5 K, 14 K and 50 K, respectively, (estimated from Eq. (2-20,21)) we found that at 4.5 K the present model is valid ($W_{ij} < C_{ij}$) up to $G \simeq 3.5$ in the 1665 MHz line, whereas the limits at 14 K and 50 K are

$G = 4.0$ and 4.5, respectively. At 4.5 K microwave quenching is more severe at 1667 MHz than at 1665 MHz for $\tau > 4$, because of the considerably higher gains encountered at 1667 MHz. This results in an enhancement of the gain at the $F = 1 \rightarrow 1$ transition with respect to $F = 2 \rightarrow 2$. At 14 K the same effect occurs for $5 \leq \tau \leq 8$; if $\tau \geq 9$ the situation is reversed. At 50 K all gains are low and quenching is supposed to be weak. In all cases, however, the magnitude of the gains, observed to be in the range 20-30 in interstellar OH formations (TUR 70, DYM 73), will be inexplicable within the present model if collisions with H_2 are included. A correct treatment of microwave quenching, however, is hard to incorporate into the present one-dimensional model, because it depends strongly on the geometry of the OH cloud and, being triggered either by spontaneous emission or by the isotropic 3 K background radiation, is essentially not a one-dimensional proces. Comparing the results with and without collisions it is expected that, in case microwave quenching is not too strong, the gains at a low collisional transition rate will be higher than the values shown in Table 6.1 and the gain at 1665 MHz will grow with respect to 1667 MHz.

The present calculations show that the UV induced population transfer mechanism, as proposed by Litvak (LIT 66) and applied by Turner (TUR 70), is able to explain, under certain conditions of temperature and projected density, some characteristics of Class I OH emitters such as the existence of anomalous intensity ratios of the four ground state microwave transitions and the dominance of the 1665 MHz emission. The model seems to fail, however, in explaining the observed high gains at the main line transitions of the ground state. The present results indicate that these high gains are only possible at low H_2 densities and low temperatures (< 14 K), in which case quenching effects due to microwave transitions across the Λ-doublet should be taken into account.
UV excitation from higher rotational states is believed to be negligible due to the extremely low population rates (via collision and the cascade following UV excitation from the ground state) involved compared to the spontaneous emission rates of these

states (1-100 s^{-1}). Other refinements of the model include trapping of UV radiated in the decay of the Σ state (ELI 76) in a two- or three-dimensional model, which increases the efficiency of the pumping proces and therefore possibly allows for higher gains, interaction with population transfer processes due to IR and more sophisticated collision models (GWI 73, BER 76).

6.2 CONCLUSIONS

Intra-cavity frequency doubling of a single mode dye laser has proven to be a powerful technique to obtain high molecular excitation efficiencies in the UV, which are at least two orders of magnitude larger than obtainable with any other tunable radiation source. Together with the present frequency stabilization long time measurements of radiative population transfer have been made possible. The present measurement of the hyperfine structure in an electronically excited state by the technique of laser induced fluorescence from a molecular beam is the first one in the UV region.

To determine the astrophysical consequences of overlapping UV transitions in interstellar OH formations, the present measuring accuracy of approximately 2 MHz is sufficient, If desired, however, greater resolution may be obtained by the application of a better collimated molecular beam or by reduction of the region from which fluorescence is detected. If the total beam divergence in this region is kept below 1°, the known ground state hyperfine splittings of OH are resolved in the $J = 3/2$ state, which eliminates the need for additional frequency calibration and consequently render drift corrections, to be applied in our situation, redundant. This procedure, however, will not be effective if the ground state splittings are much smaller than 50 MHz (higher rotational states in OH), because the divergency cannot be reduced at will without reduction of the sensitivity. Double resonance experiments, using the frequency stabilized UV radiation to populate the electronically excited state followed by microwave or RF excitation to the other hyperfine state, permits much higher resolution, because the attainable accuracy is determined by the frequency calibration of the microwave or RF radiation (GER 73). Because the transitions in the Σ state are $\pm \leftrightarrow +$ parity transitions in this method, high microwave or RF fields are required to induce these transitions, which limits the applicability of this technique because of the occurrence of gaseous discharges in the excitation region (GFR 73). The technique described in this thesis can also be used to measure the hyperfine structure in the $A^2\Sigma^+_{1/2}$, $v = 1$ vibrational state of OH by excitation with UV radiation near 281.9 nm (DIE 62), which, however, requires different coatings in the laser system in conjunction with an angle-tuned ADP or KDP crystal. With an ADA crystal UV generation is possible in the wavelength range of 290-310 nm (Fig. 3.2) by temperature tuning or above this region by angle tuning, which permits the study of the energy level structure of other free radicals having electronic absorption bands in the 300 nm region, such as OD, SH, CN, and NH.

Beam maser investigation of the influence of electronic excitation on the intensities of two different microwave transitions measured simultaneously is a powerful technique to obtain branching ratios. When the three-level population transfer is induced in reversed order several uncertainties are eliminated like state-selector efficiencies and anomalous rotational occupation distributions, which can often be quantified only very approximately. The present measurements are the first ones of this type using CW UV excitation in a molecular beam. From the intensity changes observed on the $X^2\Pi_{3/2}$, $J = 3/2$ and $J = 5/2$ Λ-doublet transitions some evidence for the existence of anomalous branching ratios from the $A^2\Sigma^+_{1/2}$, $K = 1$, $J = 3/2$, $F = 2,+$ state of OH has been obtained. Definite conclusions about this possibility can be drawn after investigation of another scheme of transitions involving either the $Q_1(1)$ or the $P_1(2)$ lines and which also permits the determination of the absolute values for these ratios. The experimental accuracy then has to be improved which is possible by an enhancement of the UV excitation by either a higher UV intensity or a larger number of reflections. The latter is possible by the application of mirrors having a higher UV reflectivity or by a multiple reflection system in which the UV radiation crosses the molecular beam a large number of times in a very confined region (KIE 72). Enlargement of the UV intensity is possible by a more collimated laser beam, a reduction of the losses in the radiation transfer system and by use of higher pumping powers from the argon ion laser. The latter can only be achieved if thermal lensing effects in the dye medium are reduced by the use of other solvents and a higher dye flow velocity (LEU 76, FRO 76). Power improvement is also possible by a reduction of the losses in the dye laser cavity through the application of other tuning elements, like a birefringent filter to replace the tuning wedge or a retroflecting grating in a double Michelson set-up for mode selection (PIN 78). From the discussion in Chap. 3 it is concluded that a reduction of the length of the frequency doubling crystal may also result in an enhancement of the generated UV power due to a decrease of absorption and of thermal phase-mismatching problems inside the crystal. Frequency stability can be improved by the application of separate feedback loops for LF and HF noise components present in the dye laser output frequency, whereas intensity dependent gain control in the feedback loop will minimize the probability of oscillation of the electronic circuitry at higher output power levels from the dye laser. With the advent of the ring dye laser important new facilities for the generation of high power single mode UV radiation have become available, that can be applied in the study of the UV induced population transfer mechanism for interstellar hydroxyl.

The intensity $I_\nu(s)$ at frequency ν and position s is derived from the power dP_ν within frequency bandwidth $d\nu$ flowing within a solid angle $d\Omega$ through a surface element $d\sigma$ normal to the direction of propagation:

$$dP_\nu = I_\nu d\nu d\sigma d\Omega \tag{A1-1}$$

If the spontaneous emission is assumed to be isotropic and the stimulated processes to be due to a radiation field having an energy density $\rho_\nu(s) = \frac{1}{c} I_\nu(s)\, d\Omega$, the energy balance between spontaneous and stimulated processes within a volume element $dV = d\sigma . ds$ then yields the differential equation for the variation of intensity along the direction of propagation s:

$$\frac{dI_\nu(s)}{ds} = \sum_{\substack{i \\ j<i}} \left[\frac{h\nu}{4\pi} A_{ij} N_i(s) g(\nu,\nu_{ij}) + \frac{h\nu}{c} B_{ij} I_\nu(s) g(\nu,\nu_{ij}) \times \left\{N_i(s) - \frac{g_i}{g_j} N_j(s)\right\}\right] \tag{A1-2}$$

Here g_i is the degeneracy of level i and $g(\nu,\nu_{ij})$ the line shape of the transition $i \rightarrow j$ centered at ν_{ij}, which, in the interstellar situation, is assumed to be Gaussian due to Doppler broadening:

$$g(\nu,\nu_{ij}) = \frac{2}{\Delta\nu_{ij}} \sqrt{\left(\frac{\ln 2}{\pi}\right)} \exp\left[-\ln 2\left(\frac{\nu-\nu_{ij}}{\Delta\nu_{ij}/2}\right)^2\right] \tag{A1-3}$$

The Einstein A_{ij} and B_{ij} coefficients are related by:

$$A_{ij} = \frac{8\pi\nu_{ij}^3 h}{c^3} B_{ij} \tag{A1-4}$$

$$B_{ij} = \frac{|\mu_{ij}|^2}{6\varepsilon_o h^2} \tag{A1-5}$$

and: $$g_i B_{ij} = g_j B_{ji} \tag{A1-6}$$

where μ_{ij} is the dipole moment matrix element of the transition $i \rightarrow j$. The Einstein B coefficient given by Eq. (A1-5) has been averaged over the orientations of the molecular dipole moment (assumed to have an isotropic distribution of directions) relative to the two polarization directions of the radiative field. The ratio R of the spontaneous and stimulated terms in Eq. (A1-2) is estimated by considering a two-level system:

$$R = \frac{cA_{21}}{4\pi B_{21} I_\nu} \times \frac{N_2}{N_2 - \frac{g_2}{g_1} N_1} \tag{A1-7}$$

In the presence of stimulated and spontaneous processes and a negligible collisional transition rate the steady state populations N_1 and N_2 are related by:

$$\frac{N_1}{N_2} = \frac{A_{21} + B_{21}\rho(\nu_{21})}{B_{12}\rho(\nu_{21})} \tag{A1-8}$$

Here $\rho(\nu) = I_\nu \Delta\Omega/c$ is the energy density in the radiation field at ν assumed to be due to a radiation field propagating within a solid angle $\Delta\Omega$ (the width $\Delta\nu_{12}$ of the molecular absorption profile is assumed to be much smaller than the spectral width of ρ, which is true for the UV radiation at the front of the OH cloud). Insertion of (A1-8) into (A1-7) then yields at line center ($\nu=\nu_{21}$):

$$|R_{\nu_{21}}| = \frac{\Delta\Omega}{4\pi} \tag{A1-9}$$

This expression shows, that the spontaneous transitions can be neglected in the calculation of I_ν within the cloud, if this intensity is confined within a very small solid angle.

The expression for the electric field strength in a focused Gaussian beam has been derived by Bjorkholm (BJO 66). The result, taking into account crystal absorption and assuming a time dependence $e^{-i\omega t}$, is:

$$\vec{E}(x,y,z) = \frac{\vec{E}_o}{1+i\tau}\, e^{-\frac{1}{2}\alpha z} e^{ikz} \exp\{-(x^2+y^2)/w_o^2(1+i\tau)\} \qquad \text{(A2-1)}$$

Herein α represents the power absorption coefficient of the crystal medium at frequency ω, k the wavevector of the central pencil of the focused laser beam inside the crystal (coinciding with the z-axis), $2w_o$ the diameter of the beam waist and $\tau=2(z-z_f)/b$, where z_f is the focal position (Fig. A2.1); b is the confocal parameter given by the relation:

$$b = w_o^2 k \qquad \text{(A2-2)}$$

The origin is taken on the center of the beam at the crystal surface. In birefringent media the expression (A2-1) is valid only for the ordinary wave. Boyd et al (BOY 68) have derived an

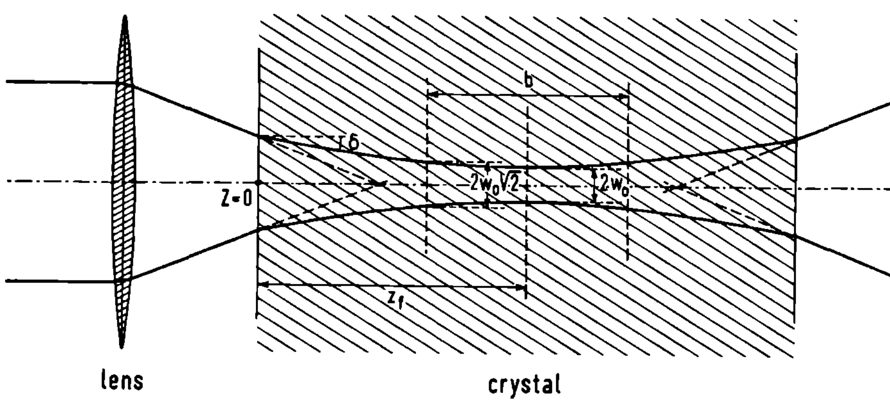

Fig. A2.1 The focused Gaussian beam geometry (the vertical dimensions are greatly exaggerated).

expression for the extra-ordinary wave, which will not be reproduced here, because its knowledge is not required for type I SHG processes in negative uniaxial crystals. The intensity distribution (power per unit area) at frequency ω is given by:

$$I(x,y,z) = \tfrac{1}{2}\varepsilon_o c n_o |\vec{E}_o|^2 e^{-\alpha z} \frac{\exp\{-2(x^2+y^2)/w_o^2(1+\tau^2)\}}{1+\tau^2} \qquad \text{(A2-3)}$$

where n_o represents the refractive index of the ordinary ray at frequency ω. From this result the following equivalent definitions for the confocal parameter b are deduced:

- the distance between the half power points on axis on either side of the focus and applies only in the absence of absorption;
- the distance between the locations on either side of the focus, where the spotsize w of the beam has increased to $w_o\sqrt{2}$;

The confocal parameter is related to the far-field diffraction angle δ, shown in Fig. A2.1, by the expression:

$$b = \frac{2w_o}{\delta} \qquad \text{(A2-4)}$$

It should be emphasized that the quantities used in the theory on SHG are to be taken inside the nonlinear crystal and are related to their vacuum equivalents by the relations:

in vacuo	in crystal	
k/n_o	k	
δn_o	δ	(A2-5)
w_o	w_o	
b/n_o	b	

The problem of focusing of a Gaussian beam by a lens, having focal length f, has been discussed by Yariv (YAR 75). Extension of his result to the confocal parameter b inside the crystal delivers, using (A2-2) and (A2-5):

$$b = \frac{4f^2 n_o^2}{kw^2} \Big/ \left[1 + \left(\frac{2fn_o}{kw^2} \right)^2 \right] \tag{A2-6}$$

where the beam incident on the lens is assumed to have its waist w at the lens. In practical situations the last term in the denominator is very small and (A2-6) is very well approximated by:

$$b = \frac{4f^2 n_o^2}{kw^2} \tag{A2-7}$$

The curvature P of the wave front of the Gaussian beam at a distance s behind the crystal is determined via the propagation law for Gaussian beams in the paraxial approximation (YAR 75) assuming the focus to be centered in the crystal:

$$R = s + \frac{L}{2n_o} + \left(\frac{b}{2n_o} \right)^2 \Big/ \left[s + \frac{L}{2n_o}\right] \tag{A2-8}$$

We consider a n-level system, where population is transferred from level 1 in the ground state to level 2 in the excited electronic state $A^2\Sigma^+_{1/2}$ by means of UV excitation at a rate W_{12}. In the subsequent decay of level 2 population is returned to level 1 by spontaneous and stimulated processes at a rate A_{21} and W_{21}, respectively, and transferred to various other levels, designated $i = 3,4,\ldots,n$ by spontaneous emission at a rate A_{2i}. The stimulated emission rate W_{21} is related to the excitation rate W_{12} by $g_2W_{21} = g_1W_{12}$ with g_k the degeneracy of level k. With these processes the rate of change of the population of the various energy levels is given by:

$$\dot{N}_1 = -W_{12}N_1 + (W_{21}+A_{21})N_2 \tag{A3-1}$$
$$\dot{N}_2 = W_{12}N_1 - (W_{21}+A)N_2 \tag{A3-2}$$
$$\dot{N}_i = A_{2i}N_2 \qquad (i = 3,4,\ldots \tag{A3-3}$$

Herein $A = \sum_{i=1}^{n} A_{2i}$ represents the total spontaneous decay rate of level 2. The population $N_i(t)$ of level i at time t is obtained by solving this system of equations assuming $N_i(0) = 0$ for $i > 1$. The result is:

$$N_1(t) = \frac{N_1(0)}{\lambda_+-\lambda_-}\left[(\lambda_++W_{21}+A)\exp(\lambda_+t)-(\lambda_-+W_{21}+A)\exp(\lambda_-t)\right] \tag{A3-4}$$

$$N_2(t) = N_1(0)\,\frac{W_{12}}{\lambda_+-\lambda_-}\left[\exp(\lambda_+t)-\exp(\lambda_-t)\right] \tag{A3-5}$$

$$N_i(t) = N_1(0)\,\frac{W_{12}A_{2i}}{\lambda_+-\lambda_-}\left[\frac{\exp(\lambda_+t)}{\lambda_+} - \frac{\exp(\lambda_-t)}{\lambda_-}\right] + \frac{A_{2i}}{A-A_{21}}\,N_1(0) \tag{A3-6}$$

with $\lambda_\pm = -\tfrac{1}{2}(W_{12}+W_{21}+A) \pm \tfrac{1}{2}\left[(W_{12}+W_{21}+A)^2-4W_{12}(A-A_{21})\right]^{1/2}$ (A3-7)

If the interaction time of the molecules with the radiation field is given by T, only spontaneous decay of level 2 occurs for $t > T$ (all levels $i \neq 2$ are assumed to have an infinite lifetime, at least compared to the times of interest in the beam maser). The final population $N_i(\infty)$ of level i, including this spontaneous decay, is then given by:

$$N_i(\infty) = N_i(T) + \frac{A_{2i}}{A} N_2(T) \qquad \text{for } i \neq 2 \tag{A3-8}$$

The relative reduction $R_1 = 1 - N_1(\infty)/N_1(0)$ of the population of level 1 is obtained from Eq. (A3-4,5,8):

$$R_1 = 1 - \frac{1}{\lambda_+ - \lambda_-} \left[(\lambda_+ + A + W_{21} + W_{12}A_{21}/A)\exp(\lambda_+ T) - (\lambda_- + A + W_{21} + W_{12}A_{21}/A)\exp(\lambda_- T) \right] \tag{A3-9}$$

With the help of Eq. (A3-7) the final population of level i is then expressed in terms of R_1 by:

$$N_i(\infty) = \frac{A_{2i}}{A-A_{21}} R_1 N_1(0) \tag{A3-10}$$

If, contrary to the assumption made above, level i ($i > 2$) is not empty at $t = 0$, the resulting change in population of this level is given by Eq. (A3-10) and a relative change R_i, analogous to R_1, can be defined and expressed in terms of R_1:

$$R_i = - \frac{A_{2i}}{A-A_{21}} R_1 \frac{N_1(0)}{N_i(0)} \tag{A3-11}$$

Confining the attention to weak interactions ($W_{12} \ll A$, $W_{12}T \ll 1$) the relative changes R_1 and R_3 reduce to:

$$R_1 = W_{12}T(1-A_{21}/A) \tag{A3-12}$$

$$R_i = - \frac{A_{2i}}{A} W_{12}T \frac{N_1(0)}{N_i(0)} \tag{A3-13}$$

The quantity $W_{12}T$ in these expressions is called the excitation efficiency.

REFERENCES *

ADH 68 R.S. Adhav, J. Appl. Phys. 39, 4095 (1968)

ADH 69 R.S. Adhav, Br. J. Appl. Phys. (J. Phys. D) 2, 177 (1969)

ADH 69a R.S. Adhav, J. Opt. Soc. Am. 59, 414 (1969)

ADH 74 R.S. Adhav and M. Orzag, Electro-Optical Systems Design, Milton S. Kiver Publ., Inc. (Dec. 1974)

AIP 63 Am. Institute of Physics Handbook, 2nd ed., Chap. 6, McGraw-Hill, New York (1963)

ARM 62 J.A. Armstrong, N. Bloembergen, J. Ducuing and P. Pershan, Phys. Rev. 127, 1918 (1962)

ASH 63 A. Ashkin, G.D. Boyd and J.M. Dziedzic, Phys. Rev. Lett. 11, 14 (1963)

BAA 72 E.L. Baardsen and R.W. Terhune, Appl. Phys. Lett. 21, 209 (1972)

BEC 72 K.H. Becker, D. Haaks and T. Tatarczyk, Z. Naturforsch. 27a, 1520 (1972)

BER 76 M. Bertojo, A.C. Cheung and C.H. Townes, Astrophys. J. 208, 914 (1976)

BJO 66 J.E. Bjorkholm, Phys. Rev. 142, 126 (1966)

BOR 59 M. Born and E. Wolf, Principles of Optics, Pergamon Press, New York, 1959

BOY 65 G.D. Boyd, A. Ashkin, J.M. Dziedzic and D.A. Kleinman, Phys. Rev. 137, A1305 (1965)

BOY 68 G.D. Boyd and D.A. Kleinman, J. Appl. Phys. 39, 3597 (1968)

BRO 74 J.H. Brophy, J.A. Silver and J.L. Kinsey, Chem. Phys. Lett. 28, 418 (1974)

DES 77 J.L. Destombes, C. Marliere, A. Baudry and J. Brillet, Astron. & Astrophys. 60, 55 (1977)

---

* In the following Quart. Rep. stands for Quarterly Report of the Atomic and Molecular Research Group, Fysisch Laboratorium, Katholieke Universiteit, Nijmegen, The Netherlands. These are in English and available on request.

DES 77a J.L Destombes, C. Marliere and F. Rohart, J. Mol. Spectrosc. 67, 93 (1977)

DIE 62 G.H. Diecke and H.M. Crosswhite, J. Quant. Spectrosc. & Radiat. Transfer 2, 97 (1962)

DIM 79 W.L. Dimpfl and J.L. Kinsey, J. Quant. Spectrosc. & Radiat. Transfer 21, 233 (1979)

DOU 55 G.C. Dousmanis, T.M. Sanders and C.H. Townes, Phys. Rev. 100, 1735 (1955)

DUC 72 T.W. Ducas, L.D. Geoffrion, R.M. Osgood Jr. and A. Javan, Appl. Phys. Lett. 21, 42 (1972)

DYM 73 A. Dymanus, Interstellaire Masers, Ned. Tijdschr. Natuurk. 39, 193 (1973) (in Dutch)

ELI 76 M. Elitzur, Astrophys. J. 203, 124 (1976)

ELM 72 B.G. Elmergreen and W.H. Smith, Astrophys. J. 178, 557 (1972)

ENG 72 R. Engleman, J. Quant. Spectrosc. & Radiat. Transfer 12, 1347 (1972)

FER 77 A.I. Ferguson and M.H. Dunn, IEEE J. Quant. Electron. QE-13, 751 (1977)

FRE 66 K.F. Freed, J. Chem. Phys. 45, 4214 (1966)

FRO 52 R.A. Frosch and H.M. Foley, Phys. Rev. 88, 1337 (1952)

FRO 76 D. Fröhlich, L. Stein, H.W. Schröder and H. Welling, Appl. Phys. 11, 97 (1976)

GER 73 K.R. German, T.H. Bergeman, E.M. Weinstock and R.N. Zare, J. Chem. Phys. 58, 4304 (1973)

GER 75 K.R. German, J. Chem. Phys. 62, 2584 (1975)

GER 80 K.H. Gericke, G. Ortgies and F. Comes, Chem. Phys. Lett. 69, 156 (1980)

GOR 54 J.P. Gordon, H.J. Zeiger and C.H. Townes, Phys. Rev. 95, 282 (1954)

GWI 73 W.D. Gwinn, B.E. Turner, W.M. Goss and G.L. Blackman, Astrophys. J. 179, 789 (1973)

HAB 74 H.J. Habing, W.M. Goss, H.E. Matthews and A. Winnberg, Astron. & Astrophys. 35, 1 (1974)

HEM 77 J.C. Hemminger, R. Cavanagh, J.M. Lisy and W. Klemperer, J. Chem. Phys. 67, 4952 (1977)

HOG 74 P. Hogan and D.D. Davis, Chem. Phys. Lett. 29, 555 (1974)

JOH 67 I.D. Johnston, Astrophys. J. 150, 33 (1967)

JUD 63 B.R. Judd, Operator Techniques in Atomic Spectroscopy, McGraw-Hill Inc., New York (1963)

KAT 74 K. Kato, IEEE J. Quant. Electron. QE-10, 616 (1974)

KAT 75 K. Kato, J. Appl. Phys. 46, 2721 (1975)

KIE 72 W. Kiefer, H.J. Bernstein, H. Wieser and M. Danyluk, J. Mol. Spectrosc. 43, 393 (1972)

KLE 62 D.A. Kleinman, Phys. Rev. 128, 1761 (1962)

KLE 66 D.A. Kleinman, A. Ashkin and G.D. Boyd, Phys. Rev. 145, 338 (1966)

KOG 71 H. Kogelnik, CRC Handbook of Lasers, ed. R.J. Pressley, 1971

KOG 72 H. Kogelnik, E.P. Ippen, A. Dienes and C.V. Shank, IEEE J. Quant. Electron. QE-8, 373 (1972)

KRA 66 J.D. Kraus, Radio Astronomy, McGraw-Hill Inc., New York, 1966

LAN 62 Landolt-Börnstein, Zahlenwerte und Funktionen, 6. Auflage, II Band, 8. Teil: Optische Konstanten, Springer Verlag, Berlin (1962)

LEE 75 W.R. Leeb, Appl. Phys. 6, 267 (1975)

LEM 79 B. Lemoine, R. Bustreel, C. Demuynck and J.L. Destombes, J. Chem. Phys. 71, 3131 (1979)

LEN 77 R.K. Lengel and D.R. Crosley, J. Chem. Phys. 67, 2085 (1977)

LEU 76 S. Leutwyler, E. Schumacher and L. Wöste, Opt. Comm. 19, 197 (1976)

LIE 80 D.A. Lieberman, F. Raab and H. Metcalf, Bull. Am. Phys. Soc. 25, 493 (1980)

LIT 66 M.M. Litvak, A.L. McWorther, M.L. Meeks and H.J. Zeiger, Phys. Rev. Lett. 17, 821 (1966)

LIT 69 M.M. Litvak, Astrophys. J. 156, 471 (1969)

MAR 77 R.P. Mariella and A.C. Luntz, J. Chem. Phys. 67, 5388 (1977)

MEE 71 W.L. Meerts, Quart. Rep. 31, 23 (1971)

MEE 73 W.L. Meerts and A. Dymanus, Chem. Phys. Lett. 23, 45 (1973)

MEE 75 W.L. Meerts and A. Dymanus, Can. J. Phys. 53, 2123 (1975)

MEE 75a W.L. Meerts, Thesis, Katholieke Universiteit, Nijmegen (1975)

MEU 72 J.J. ter Meulen and A. Dymanus, Astrophys. J. 172, L21 (1972)

MEU 74 J.J. ter Meulen, Quart. Rep. 42, 169 (1974)

MEU 76 J.J. ter Meulen, Thesis, Katholieke Universiteit, Nijmegen (1976)

MEU 76a J.J. ter Meulen, W.L. Meerts, G.W.M. van Mierlo and A. Dymanus, Phys. Rev. Lett. 36, 1031 (1976)

MEU 77 J.J. ter Meulen, Quart. Rep. 55, 95 (1977)

MID 65 J.E. Midwinter and J. Warner, Br. J. Appl. Phys. 16, 1135 (1965)

MIE 73 G.W.M. van Mierlo, Quart. Rep. 40, 102 (1973)

MIE 76 G.W.M. van Mierlo, Quart. Rep. 52, 51 (1976)

NIK 77 D.N. Nikogosyan, Sov. J. Quant. Electron. 7, 1 (1977)

OKA 71a M. Okada and S. Ieiri, IEEE J. Quant. Electron. QE-7, 469 (1971)

OKA 71b M. Okada and S. Ieiri, IEEE J. Quant. Electron. QE-7, 560 (1971)

PHI 66 R.A. Phillips, J. Opt. Soc. Am. 56, 629 (1966)

PIN 78 M. Pinard, C.G. Aminoff and F. Laloë, Appl. Phys. 15, 371 (1978)

POY 68 R.L. Poynter and R.A. Beaudet, Phys. Rev. Lett. 21, 305 (1968)

QTL 71 Quantum Technology, Data Sheet 701, Oct. 1971

QTL 71a Quantum Technology, Data Sheet 702, Oct. 1971

QTL 74 Quantum Technology, Data Sheet 707, Jan. 1974

RAA 80 F. Raab, T. Bergeman, D. Lieberman and H. Metcalf, Opt. Lett. 5, 427 (1980)

RAD 64 H.E. Radford, Phys. Rev. A 136, 1571 (1964)

SIN 71 S. Singh, CRC Handbook of Lasers, ed. R.J. Pressley, 1971

SUE 67 Y. Suemune, J. Phys. Soc. Japan 22, 735 (1967)

SUV 67 V.S. Suvorov and A.S. Sonin, Sov. Phys. Crystall. 11, 711 (1967)

TES 76 O. Teschke, J.R. Whinnery and A. Dienes, IEEE J. Quant. Electron. QE-12, 513 (1976)

TUR 67 B.E. Turner, Ph. D. Thesis (unpublished), Univ. of Calif., Berkeley (1967)

TUR 70 B.E. Turner, J. R. Astron. Soc. Canada 64, 221 (1970)

VER 69 J.A.Th. Verhoeven, Thesis, Katholieke Universiteit, Nijmegen (1969)

VON 58 F.O. Vonbun, J. Appl. Phys. 29, 632 (1958)

WAN 74 C.C. Wang and L.I. Davies, Phys. Rev. Lett. 32, 349 (1974)

WEA 65 H.F. Weaver, D.R. Williams, N.H. Dieter and W.T. Lum, Nature 208, 29 (1965)

WEI 63 S. Weinreb, A.H. Barrett, M.L. Meeks and J.C. Henry, Nature 200, 829 (1963)

WEL 75 B. Wellegehausen, L. Laepple and H. Welling, Appl. Phys. 6, 335 (1975)

YAR 75 A. Yariv, Quantum Electronics, 2nd ed., J. Wiley & Sons, New York (1975)

ZER 64 F. Zernicke Jr., J. Opt. Soc. Am. 54, 1215 (1964)

ZER 73 F. Zernicke and J.E. Midwinter, Applied Nonlinear Optics, J. Wiley & Sons, New York (1973)

In deze dissertatie is een onderzoek beschreven naar populatie transport in interstellaire hydroxyl formaties geinduceerd door ultraviolette straling rond 308 nm. Als gevolg van de UV excitatie naar de eerste aangeslagen electronische toestand $A^2\Sigma^+_{1/2}$ en het daarop volgend verval terug komt onder bepaalde omstandigheden (temperatuur en dichtheid) populatie inversie tussen de hyperfijne toestanden in de laagste energie toestand $X^2\Pi_{3/2}$, $J = 3/2$ tot stand. Bij voldoende grote inversie kan dit proces resulteren in de waargenomen maser emissies bij 1.6 GHz op de vier overgangen welke tussen deze hyperfijn toestanden mogelijk zijn. Volgens het UV pomp model hangen de relatieve intensiteiten van de vier emissie lijnen sterk af van de mate van overlap tussen de $A^2\Sigma^+_{1/2}$ hyperfijn toestanden. De bepaling van de hyperfijn opsplitsingen in de $A^2\Sigma^+_{1/2}$ toestand is een van de resultaten van dit onderzoek. Hiernaast is in een bundel maser opstelling populatie inversie waargenomen als gevolg van UV excitatie.

Een beschrijving van dit transport mechanisme, alsmede van de molekulaire energie niveau structuur van OH, welke van belang is bij de bepaling van de invloed van overlap van de exciterende UV overgangen, is gepresenteerd in Hoofdstuk 2.

Uit een berekening van de UV intensiteit (par. 2.4), vereist voor de experimentele studie van dit populatie transport proces, wordt geconcludeerd dat slechts een vloeistof laser, waarvan de straling frequentie verdubbeld is door een niet-lineair crystal (ADA: Ammonium Diwaterstof Arsenaat) geplaatst in de laser trilholte, de voor dit doel vereiste vermogens kan leveren. De op dit principe gebaseerde, nieuw ontwikkelde, UV bron levert een maximum vermogen van 0.3 mW bij 308 nm, is frequentie gestabiliseerd en heeft een maximum gestabiliseerd scan bereik van 6.6 GHz bij 308 nm. Teneinde de vereiste temperatuur stabiliteit van het crystal voor optimale werking te verkrijgen is een compact dubbel oven systeem geconstrueerd, waarmee een temperatuur stabiliteit bereikbaar is van 0.01°C bij 100°C. De frequentie stabilisatie bleek nodig teneinde de drift van de laser frequentie tijdens de langdurige metingen ($\sim$1 uur) te beperken. Via de toepassing van een actief tegengekoppeld systeem is het gelukt de laser frequentie te stabiliseren t.o.v. de transmissie karakteristiek van een stabiele externe referentie trilholte, hetwelk resulteerde in een drift <100 MHz/uur van de UV frequentie. Het principe van frequentie verdubbeling in niet-lineaire media, de constructie van laser en verdubbelingseenheid, alsmede van bovengenoemde frequentie stabilisatie, is uitvoerig beschreven in Hoofdstuk 3.

De molekulaire bundel maser, die voor dit onderzoek gebruikt wordt, is beschreven in Hoofdstuk 4 met speciale aandacht voor de UV interactie zone (een spiegelconstructie welke een 40-tal passages van het UV door de molekulaire bundel toestaat) en de methode van electrostatische toestand selektie. Een molekulaire absorptie cel, bedoeld om het zoeken naar de UV overgangen van OH te vergemakkelijken, is eveneens toegepast bij de metingen en beschreven in dit hoofdstuk.

Het eerste deel van Hoofdstuk 5 beschrijft de eerste gerapporteerde metingen van de hyperfijne energie niveau structuur van OH in de $A^2\Sigma^+_{1/2}$ electronische toestand. De energie opsplitsingen zijn bepaald door variatie van de UV frequentie, waarbij de fluorescentie van de Σ toestand werd geobserveerd. De waargenomen opsplitsingen varieren tussen 198 MHz en 778 MHz, hetgeen duidelijk groter is dan de overeenkomstige grootheden in de $X^2\Pi_{1/2}$ en $X^2\Pi_{3/2}$ electronische toestanden. Vooral de hyperfijne energie opsplitsing van de laagste rotatie toestand in $A^2\Sigma^+_{1/2}$ is belangrijk groter dan van de andere toestanden.

Het tweede gedeelte van Hoofdstuk 5 is gewijd aan de metingen van het door UV geinduceerde populatie transport. Met behulp van super-heterodyne microgolf detectie technieken op de hyperfijne Λ-doublet overgangen van zowel de $X^2\Pi_{3/2}$, $J = 3/2$ als de $J = 5/2$ toestand zijn veranderingen van de microgolf intensiteit op deze overgangen waargenomen bij instraling van resonante UV straling op de $A^2\Sigma^+_{1/2}$, $K' = 1$, $J' = 3/2$, $F' = 2,+ \leftarrow X^2\Pi_{3/2}$, $J = 3/2$, $F = 2,-$ of $A^2\Sigma^+_{1/2}$, $K' = 1$, $J' = 3/2$, $F' = 2,+ \leftarrow X^2\Pi_{3/2}$, $J = 5/2$, $F = 3,-$ overgangen. De waargenomen relatieve effecten varieren van 0.1% tot 30% afhankelijk van de toestandselector spanning en de beschouwde overgang. Zowel inverterende als anti-inverterende werking is opgetreden, hetgeen in overeenstemming is met de verwachtingen. Binnen de waargenomen meetfouten kon geen duidelijke afwijking van de theoretische waarden voor de relatieve overgangs waarschijnlijkheden vanaf de Σ toestand vastgesteld worden. Bovendien is bij al deze metingen een populatie inversie van 6-8% aangetroffen in de $X^2\Pi_{3/2}$, $J = 3/2$ en $J = 5/2$ toestanden, welke in de OH produktie zone ontstaat.

Met behulp van de verkregen gegevens over de hyperfijne structuur is de invloed van overlappende UV overgangen op het populatie transport berekend (Hoofdstuk 6). De resultaten tonen aan, dat onder bepaalde condities van temperatuur, optische diepte en frequentie van botsingen met H_2, versterking van microgolf straling op de overgangen van de $X^2\Pi_{3/2}$, $J = 3/2$ toestand mogelijk is vanwege een bezettingsinversie van de betrokken energie niveaus. Indien de nivellerende invloed van microgolf overgangen op het populatie transport proces in rekening gebracht wordt, lijken evenwel de waargenomen hoge versterkingsfactoren in de interstellaire OH formaties onverklaarbaar binnen het huidige model van UV geinduceerd populatie transport.

Tevens wordt in Hoofdstuk 6 een discussie gewijd aan de toegepaste onderzoeksmethodes, waarbij suggesties ter verbetering van de meetnauwkeurigheid ter sprake komen. Vooral de komst van een moderne krachtiger UV stralingsbron (frequentie verdubbelde ring laser) lijkt veel belovend voor een verdere studie van dit populatie transport mechanisme.

Op 23 november 1949 ben ik geboren te Arnhem. Vanaf 1962 volgde ik middelbaar onderwijs aan het Thomas à Kempis College te Arnhem, alwaar in juni 1968 het getuigschrift Gymnasium β behaald werd.

Nadien volgde aan de Katholieke Universiteit te Nijmegen de studie natuurkunde en werd in april 1971 het kandidaats examen behaald. De doctoraal studie is, na een afstudeer stage bij de afdeling voor Atoom- en Molekuulfysica, in januari 1974 afgesloten met het doctoraal examen experimentele natuurkunde.

Vervolgens bleef ik, als wetenschappelijk medewerker in FOM verband, aan deze groep verbonden. In het kader van het Nijmeegse onderzoeksprojekt naar de astrofysische achtergronden van anomale microgolf emissies van interstellaire OH formaties is, onder leiding van Prof. Dr. A. Dymanus, een experimentele studie verricht van het door UV geinduceerde populatie transport mechanisme in OH. Deze studie is, via de bouw van een daartoe geschikte UV bron, beeindigd met de resultaten die in dit proefschrift vermeld staan.

Momenteel ben ik, als wetenschappelijk medewerker, verbonden aan de afdeling Signaalverwerking van het Physisch Laboratorium TNO te 's-Gravenhage.

STELLINGEN

1. In hun analyse van de branching fracties bij de resonante multifoton ionisatie van molekulaire benzeen bundels laten Silberstein en Levine de mogelijke formatie van het $C_6H_n^+$ (n=1,4) ion via niet-resonante drie-foton absorptie buiten beschouwing. Dit kan het verschil verklaren tussen de door hen berekende en de experimenteel gemeten branching fracties van dit ion complex.

J. Silberstein en R.D. Levine,
Chem. Phys. Lett. 74, 6 (1980)
L. Zandee en R.B. Bernstein,
J. Chem. Phys. 71, 1359 (1979)

2. De kwantitatieve overeenstemming voor de invloed van rotationele energie van NO op de reactiviteit met O_3 tussen enerzijds de resultaten van Redpath *et al* en anderzijds de resultaten van Anderson *et al*, zoals deze laatsten opmerken, verdwijnt volledig als men de invloed van de snelheidsverdeling van de botsende moleculen in rekening brengt.

S.L. Anderson, P.R. Brooks, J.D. Fite en On Van Nguyen,
J. Chem. Phys. 72, 6521 (1980)
A.E. Redpath, M. Menzinger en T. Carrington,
Chem. Phys. 27, 409 (1978)

3. De juistheid van de door Larson en Kostin geponeerde triplet kombinaties van lokale eigenfunkties voor diffusie in een bistabiele potentiaal is onbewezen.

R.S. Larson en M.D. Kostin,
J. Chem. Phys. 69, 4821 (1978)

4. Het verdient aanbeveling, dat de voorlichting betreffende de aktie "Moeders voor Moeders" zich niet voornamelijk richt op een uiteindelijk door het zwangerschapshormoon (HCG) te induceren nieuwe

zwangerschap, maar ook op het gebruik bij medisch begeleide afslankkuren.

5. Uit de experimenten van Flygare en Benson aan Fluoroform H en D is niet eenduidig het teken van het elektrisch dipoolmoment te bepalen.

W.H. Flygare en R.C. Benson, Mol. Phys. 20, 225 (1971)

6. De toepassing door Ferguson en Dunn van de analyse betreffende thermisch geinduceerde degradatie van de SHG konversie efficientie in niet-lineaire media, gegeven door Okada en Ieiri, is in principe niet toegestaan in geval van optimale focusering van de fundamentele straling.

A.I. Ferguson en M.H. Dunn, IEEE J. Quant. Electron. QE-13, 751 (1977)

M. Okada en S. Ieiri, IEEE J. Quant. Electron. QE-7, 469 (1971)

7. De levensduur van diamantnaalden voor het afspelen van grammofoonplaten wordt over het algemeen grotelijks overschat.

C.W. Lamberts, Disk 134, 61 (1978)

8. De resultaten van een kwantitatieve analyse van de effecten van overlappende hyperfijne UV overgangen in interstellaire hydroxyl formaties op de geproduceerde populatie inversies in de grond toestand van OH zijn sterk afhankelijk van de lijnvorm van deze overgangen.

dit proefschrift

9. Het verdient aanbeveling, gezien de grote effecten van botsingen tussen H_2 en OH in interstellaire hydroxyl formaties op de door UV excitatie geproduceerde populatie inversies in de grond toestand van OH, een experimentele studie te wijden aan dit botsingsproces.

dit proefschrift

10. De terugstrooi coefficient van aerosolen voor opvallende straling met een golflengte rond 1 μm kan berekend worden met behulp van een simpele uitdrukking, welke slechts de Junge parameters van de gemeten aerosolen verdeling bevat, hetgeen een aanzienlijke vereenvoudiging betekent vergeleken met de analyse via de Mie theorie.

C.W. Lamberts, Report PHL 1980-41,
Physisch Laboratorium TNO, Den Haag (1980)

11. Aangezien zowel hoofddeksels als luchtverontreiniging geacht worden kaalheid te bevorderen, verdient het aanbeveling een innovatief onderzoek te starten naar hoeden, mutsen en petten met een lucht filtrerend ventilatie systeem.